Departamento de Química C-IX.
Facultad de Ciencias.
Universidad Autónoma de Madrid.

One and Two-Photon Double Ionization of He and H_2 using Exterior Complex Scaling

Tesis dirigida por
Fernando Martín García,
Memoria de tesis para optar al Título de Doctor en
Química Teórica y Computacional

Felipe Morales Moreno
Madrid, Septiembre de 2009.

Agradecimientos

A Fernando Martín, mi tutor, por haber confiado en mi, incluso en mis momentos más bajos. Gracias a su apoyo, a su conocimiento, y al empeño que ha puesto en mi, estoy donde estoy.

A todos los profesores del departamento de Química, que, de una manera o de otra siempre me han prestado su ayuda, sus conocimientos y sus ganas siempre que la he necesitado.

A los profesores C. W. McCurdy y T. N. Rescigno por por darme la oportunidad de trabajar y dejarme aprender de ellos. A Dan Horner por acogerme tan hospitalariamente, y ayudarme en todo, tanto a nivel personal como a nivel científico.

A Goar, Fran, Lara, Paula, Alicia, Pablo, y a toda la gente que empezó esta aventura conmigo, gracias por todas las cosas compartidas, tanto dentro como fuera de la universidad.

A los "*laser boys*": A Thomas, a quien no tengo palabras para agradecerle el esfuerzo que ha hecho para ayudarme con mi tesis, y a Jhon Fredy y Etienne, en quienes he descubierto dos amigos. Sin los partidos de fútbol piña, el trabajo nunca sería igual.

Al resto de compañeros de departamento, (Yang, Sergio, Cristina, Ane, Danielle, Thiago y demás) con quienes he compartido tantos buenos ratos.

A Cristina, por soportar mi difícil forma de ser y por animarme en mis horas más bajas.

A mi padre y a mis hermanos, quienes siempre me han apoyado en todos

los sentidos y siempre han creído en mi. Sin su implicación todo esto hubiera sido imposible. Con ellos que he vivido todo, y jamás podré expresar todo lo que significan para mi.

A mi madre, por haberme dejado tantas cosas, por haberme hecho crecer tanto como persona. Sólo espero que se hubiera sentido orgullosa.

CONTENTS

LIST OF FIGURES

Introducción

La doble fotoionización es un proceso en el que dos electrones de un átomo o una molécula, que se encuentra en un estado dado, son arrancados por la absorción de uno o varios fotones. Estos fotones suman la energía suficiente para llevar estos dos electrones al continuo:

$$n\hbar\omega + A \rightarrow A^{++} + 2e^{-} \tag{1}$$

Generalmente, cuando el átomo o la molécula, A, está en su estado fundamental, la energía del fotón (o si es más de uno, la energía resultante de sumar todas las energías de los fotones) tiene que ser más alta que la energía del límite de la doble ionización del sistema. Desde el punto de vista teórico, en el caso de la absorción de un fotón, si la interacción entre los dos electrones que se escapan del sistema no se tiene en cuenta, el proceso de doble ionización no puede ocurrir. Por tanto, los procesos de doble ionización son muy dependientes de la manera en que se traten los efectos de correlación electrónica. Por este motivo el problema se convierte en un proceso de ruptura culombiana de tres cuerpos, en el caso de un átomo como el helio, o en un proceso de ruptura culombiana de cuatro cuerpos, para el caso de moléculas diatómicas como la molécula de hidrógeno. Esto supone un gran reto a nivel teórico, puesto que, tratar correctamente las condiciones asintóticas asociadas a la ruptura de un sistema con dos o tres partículas cargadas es una tarea particularmente complicada.

El tratamiento de las condiciones de contorno para el problema de la ruptura de tres partículas cargadas ha sido reconocido como un problema tanto formal como práctico desde los años 60 ([1, 2, 3, 4]). Pero hasta la última década no se han encontrado métodos que hayan tenido éxito a nivel formal y con un alto grado de precisión. El uso de funciones de onda usando *ansatz* con una forma explícita para las condiciones asintóticas de tres cuerpos fue usado en la aproximación de tres cuerpos de Coulomb [5, 6, 7], mientras,

otros grupos, siguiendo un proceso similar, como por ejemplo, el grupo de Shakeshaft, hicieron uso de una asunción sobre el estado final de las ondas culombianas emitidas [8, 9]. El primer intento de resolver la ecuación de Schrödinger de manera numérica, usando condiciones de contorno de dos cuerpos, mediante cálculos *close-coupling*, y construyendo las amplitudes de tres cuerpos a partir de los canales discretos de dos cuerpos se llevó a cabo a principio de los años 90 por el grupo de Bray, [10, 11, 12]. El grupo teórico de Selles, en una publicación más reciente, desarrolló un método usando funciones *outgoing* semi clásicas, combinadas en un método de R-matrix con coordenadas hiper esféricas para imponer las condiciones de contorno de tres cuerpos [13]. Otra aproximación exitosa es el método dependiente del tiempo *close-coupling*, que aplica las condiciones de contorno correctas implícitamente mediante la propagación del estado inicial [14, 15] en un método que produce resultados precisos para este tipo de problemas y otros problemas de ruptura culombiana. La necesidad de imponer condiciones de contorno de tres cuerpos fue evitada usando funciones complejas *Sturmian* en un elegante método matemático desarrollado por Pont y Shakeshaft [9].

En el campo experimental, ha habido muchos esfuerzos para entender el papel de la correlación electrónica en procesos de doble fotoionización. Por ejemplo, en 1991, se realizaron medidas de la sección eficaz diferencial simple para la doble fotoionización del átomo de helio usando espectrometría *Time Of Flight* [16]. Pero el avance experimental más importante en este campo se produjo con el desarrollo de la técnica *Cold Target Recoil Ion Momentum Spectroscopy* (COLTRIMS) a final de los años 90, en el departamento *Experimental Atomic Physics* de la *Goethe-Universität of Frankfurt* (para una historia completa del desarrollo del COLTRIMS ver [17]). Esta técnica permite la medición de energías y momentos de todas las partículas emitidas en coincidencia. Es interesante revisar [18] para obtener más detalles sobre la técnica. Esta nueva tecnología permitió a muchos grupos experimentales de todo el mundo realizar experimentos para numerosos sistemas, y recoger información respecto a diferentes problemas de ionización. Respecto a la doble ionización del átomo de helio, hubo unos cuantos experimentos, por ejemplo [19, 20, 21, 22, 23, 24].

Intentar resolver este problema en una molécula añade nuevas dificultades, puesto que, por ejemplo, a la doble fotoionización en el H_2 le sigue una explosión culombiana de los dos protones resultantes. Este proceso es rápido comparado con la rotación molecular, y, en consecuencia, el vector de momento relativo de los núcleos en disociación definen la alineación de la molécula en el momento de la absorción del fotón. De esta manera, es posible medir secciones eficaces diferenciales de moléculas como si estuvieran fijas en el espacio, mientras se hayan medido en coincidencia las cuatro partículas resultantes. Por tanto, la técnica COLTRIMS también puede ser empleada

para la doble fotoionización del H_2, con la condición de que se detecten tres de las cuatro partículas, puesto que el momento y la energía de la cuarta puede ser deducido por las leyes de conservación de la energía y el momento. Los primeros experimentos llevados a cabo para la doble fotoionización del H_2 usando esta técnica experimental fueron hechos por T. Webber *et al.* entre 2003 y 2004 [25, 26]. Estos experimentos abrieron el camino a muchos otros grupos, como por ejemplo [27]. Todo esto supuso un reto para cualquier método teórico *ab initio*. Aunque ha habido otros, la metodología expuesta en este trabajo fue una de las primeras en ofrecer resultados precisos, directamente comparables con estos nuevos experimentos. Los resultados de [28] supusieron uno de los primeros resultados teóricos que resolvieron el problema de la doble fotoionización para una molécula.

El uso de todas estas técnicas teóricas y experimentales, ha dado lugar al descubrimiento de nuevos procesos físicos, y, por supuesto, podrán llevar a nuevos descubrimiento en un futuro. Por ejemplo, en 1966 Cohen y Fano sugirieron que, cuando un electrón escapa de una molécula diatómica, este electrón puede mostrar patrones de interferencia provocados por los dos núcleos [29]. Gracias a los avances tanto teóricos como experimentales, la difracción de doble rendija en la ionización sencilla en el H_2 está actualmente bien modelada [30], y comprobada experimental [31, 32], y teóricamente [33, 34]. Estudios experimentales recientes [35, 36] sugirieron que estas interferencias también podían aparecer en la doble fotoionización de la molécula de hidrógeno. Este problema se estudiará a nivel formal en el Capítulo 5 aplicando el método teórico expuesto en esta tesis.

Como añadido a todas las dificultades de la doble fotoionización mediante un fotón de átomos y moléculas, la doble fotoionización mediante dos fotones introduce aún más retos a cualquier tratamiento teórico. El proceso se puede resumir así:

$$\hbar\omega + \hbar\omega + A \rightarrow A^{++} + 2e^{-} \tag{2}$$

Este proceso de dos fotones puede ocurrir en varias etapas, dependiendo de las energías del fotón, y también del sistema tratado. La absorción del primer fotón lleva al sistema a un estado "intermedio", y, es desde este estado desde dónde se produce la absorción del segundo fotón. La naturaleza de este estado "intermedio", que está directamente relacionada con la energía del fotón, es una de las complicaciones más delicadas en el tratamiento teórico de este tipo de problemas. Este estado "intermedio" puede ser directamente un estado en el que uno o los dos electrones se pueden encontrar en el continuo. Este proceso se llama *Above Threshold Ionization* (ATI, ionización por encima del límite), y será tratado en detalle dentro de esta tesis. El Capítulo 6 muestra la aplicación de los formalismos aquí expuestos al problema de la ionización del átomo de hidrógeno, que sirve como punto de partida para

entender la problemática que implican los procesos ATI.

Por ejemplo, para la doble ionización mediante dos fotones del átomo de helio, con energías de fotón en el rango de [39.4-54.4] eV, hay dos procesos de ionización compitiendo. El papel de estos procesos, como interfieren, y como esta interacción afecta a la sección eficaz total es, a día de hoy, un asunto de discusión teórica [37, 38, 39, 40, 41, 42, 43, 44, 45, 46, 47, 48, 49, 50, 51, 52, 53, 54], discusión empezada por un trabajo experimental [55]. Este trabajo llevado a cabo en Japón, usó fuentes de luz mediante la generación de armónicos esféricos altos para ionizar el sistema. Otro experimento fue llevado a cabo en Hamburgo, usando el láser de electrones libres (FLASH) [56, 57]. Ambos métodos experimentales hacen uso de la última tecnología láser disponible, y fueron llevados a cabo en el régimen de intensidades donde la teoría de perturbaciones de segundo orden debe funcionar. A pesar de todo ello, dichos experimentos no tienen aún la suficiente resolución para medir unas secciones eficaces tan pequeñas, mientras que las predicciones teóricas no están de acuerdo en el valor absoluto de la sección eficaz total. Los resultados experimentales aún tienen barras de error demasiado grandes como para extraer conclusiones acerca de este desacuerdo, y, por tanto, existe todavía una discusión acerca de los efectos de la correlación electrónica en este problema. Los resultados para este sistema en esta región de energías de fotón serán presentados en el Capítulo 7.

Siguiendo el mismo camino llevado para la ionización sencilla, los primeros experimentos para la doble fotoionización mediante dos fotones del H_2 están siendo llevados a cabo [58]. Al mismo tiempo, los primeros trabajos teóricos han sido publicados [59, 60], demostrando que, incluso si los resultados teóricos están en desacuerdo, este campo de investigación está todavía lleno de física por explorar. Los efectos puramente moleculares, el papel de los estados autoionizantes, y el comportamiento de las secciones eficaces en las regiones donde los procesos ATI son posibles, son un ejemplo de las cuestiones abiertas que necesitarán ser respondidas en un futuro. Los resultados actuales fruto de esta tesis se mostrarán en el Capítulo 8.

Esta tesis está dividida en dos grandes partes. La primera parte describe toda la teoría necesaria para comprender el formalismo usado para este trabajo. Esta parte comienza con una pequeña introducción a todos los capítulos que le siguen. La otra parte contiene los resultados teóricos más significativos que fueron obtenidos durante esta tesis. Posteriormente, habrá un capítulo con el resumen de las conclusiones alcanzadas más importantes, y unos apuntes sobre dónde podría estar el trabajo por hacer en este campo. Para finalizar, a modo de apéndice, se incluye una breve descripción de los métodos computacionales usados.

Introduction

Double photoionization is a process in which two electrons from an atom or a molecule, which lies in a given state, are taken away by one or several photons, photons that carry enough energy to take two electrons into the continuum:

$$n\hbar\omega + A \rightarrow A^{++} + 2e^{-} \tag{3}$$

Typically, when the atom or molecule, A, is in its ground state, the photon energy (or if more than one, the energy that results from adding all the photon energies) should be higher than the double ionization threshold in order to eject two electrons. From a theoretical point of view in the case of one-photon absorption, if the interaction between the two ejected electrons is completely neglected, the double ionization process cannot occur. Therefore, the double ionization process is very dependent on the way the electronic correlation effects are treated. This turns this problem into a full three body Coulomb breakup, in the case of an atom like helium, or into a four body Coulomb breakup problem for diatomic molecules like the hydrogen molecule. This already poses a truly theoretical challenge, because to treat correctly the boundary conditions associated with the breakup of a system with three or four charged particles is a particularly difficult task.

The treatment of the boundary conditions for the breakup of three charged particles has been known as a formal and practical problem since the 1960s ([1, 2, 3, 4]). But one has to go to the last decade in order to find methods that succeeded both formally and accurately. Ansatz wave function with an explicit three-body asymptotic form was used in the three Coulomb body wave approach [5, 6, 7], while, others, in a similar approach, like for example, Shakeshaft and coworkers, made use of an assumed final state of the screened Coulomb waves [8, 9]. The first attempt to solve the Schrödinger equation numerically, using two-body boundary conditions within close-coupling calculations, and constructing three-body breakup amplitudes from the two-body

discrete channel amplitudes was performed in the early 1990s by Bray et al. [10, 11, 12]. Selles et al., in a more recent publication, developed a method using semi-classical outgoing waves, combined with the hyperspherical R-matrix method to impose outgoing three-body boundary conditions [13]. Another successful approach is the time-dependent close-coupling method which applies the correct boundary conditions implicitly by time propagation of the initial state [14, 15] in a method that produces accurate results for the present case and other Coulomb breakup problems. The need to explicitly impose three-body asymptotic boundary conditions was avoided using complex Sturmian basis functions in a mathematically elegant method developed by Pont and Shakeshaft [9].

Experimentally, there has been a lot of efforts to understand the role of electronic correlation in the double photoionization processes. For example, in 1991, measurements of the single differential cross sections for double photoionization of He were performed using time of flight spectrometer [16]. But the biggest experimental breakthrough in measuring techniques in this field was achieved with the development of the Cold Target Recoil Ion Momentum Spectroscopy (COLTRIMS) in the late 1990s, in the Experimental Atomic Physics department at the Goethe-Universität of Frankfurt (for a complete history on the development of COLTRIMS see [17]). This technique allows for the measurement of the energies and momenta of all the ejected particles in coincidence. For more details about these experimental measurements it is worth to recall [18]. This new experimental setup allowed groups from all over to world to perform experiments for numerous targets, and recover information concerning different ionization problems. Regarding the double ionization of the helium atom, there were quite a few experiments, for example those in [19, 20, 21, 22, 23, 24].

Trying to solve this problem with a molecule introduces more difficulties, as, for example, the double photo ionization in H_2 is followed by a Coulomb explosion of the resulting two bare protons. This process is rapid compared to the molecular rotation, so, the relative momentum vector of the dissociating nuclei defines the alignment of the molecule at the instant of photon absorption. This way, it is possible to measure differential ionization cross sections of the molecules as if they were fixed in space, provided that all four particles emerging from the system are detected in coincidence. Therefore, the COLTRIMS technique can also be applied to double photoionization of H_2, whereas three of the four particles are detected, since momentum and energy of the fourth can be deduced by laws of energy and momentum conservation. First experiments carried out on double photon ionization of H_2 using this experimental methodology were performed by T. Webber et al. in 2003-2004 [25, 26]. They opened the way for more experiments, for example [27], which already pose a significant challenge to any ab initio theory.

Although there are others, the methodology shown in this work was one of the first to offer accurate results, directly comparable with these experiments. The results from [28] were one of the first theoretical calculations that solved the double photoionization for a molecule giving accurate results.

With all these experimental and theoretical techniques, a lot of new physics has been discovered, and, of course, can lead to exciting results in a future. For example, in 1966 Cohen and Fano suggested that, when a diatomic molecule ejects one of the electrons, this electron can show interference patterns as the result of the diffraction by the two nuclei [29]. This two-slit diffraction in single photoionization of H_2 is now well modeled [30], and, after both experimental [31, 32], and theoretical [33, 34] studies, it is well understood. Recent experimental results [35, 36] suggested that this interferences also appear in double ionization of the hydrogen molecule. With all the formalism exposed in this thesis, this problem will also be studied from a theoretical point of view in Chapter 5.

In addition to all the difficulties of single photon double ionization of atoms and molecules, two-photon ionization adds even more challenges to any theoretical treatment, as, the ionization is produced by the absorption of two photons instead of just one:

$$\hbar\omega + \hbar\omega + A \rightarrow A^{++} + 2e^{-} \tag{4}$$

This two-photon process can occur in several steps, depending on the photon energies, and also depending on the system being treated. The first photon absorption takes the system into a “intermediate’ state, and, it is from that state that the second photon is absorbed. The nature of that ”intermediate“ state, which is directly related to the photon energy, is one of the biggest complications when treating theoretically this kind of problems, as this “intermediate” state can already be a state in which one or both of the electrons are already in the continuum. This is called Above Threshold Ionization (ATI), and will be addressed in detail within this thesis. Chapter 6 shows the application of the ECS formalism to the problem of ionization of the hydrogen atom with two photons, which served as an starting point in order to understand all the problems that ATI implies.

For example, for the two photon double ionization of He, with photon energies in the range of [39.4-54.4] eV, there are two ionization processes competing. The role of these processes, how they interfere, and how this affects the total cross sections, it is still subject of theoretical discussions [37, 38, 39, 40, 41, 42, 43, 44, 45, 46, 47, 48, 49, 50, 51, 52, 53, 54], and was first started by an experimental work [55]. This work, performed in Japan, made use of high harmonic generation sources in order to ionize the target.

Another experimental work was carried out in the free electron laser source located in Hamburg (FLASH) [56, 57]. Both of these experiments are making use of the latest technology of laser sources available, and performed within the laser intensity regime where second order perturbation theory is expected to work. However, the current experiments do not have sufficient resolution yet to measure such small cross-sections, while the present theoretical predictions do not even agree in the total ionization cross-sections. Experimental results have still large error bars, too large to settle down the theoretical disagreement, and, therefore, there is a still ongoing discussion about the effects of electron correlation. Results for two photon double ionization of He in this photon energy region will be presented in Chapter 7.

Following in the same path that was taken for single ionization, first experiments for the two photon double ionization of H_2 are being carried out [58]. At the same time the first theoretical works have already been published [59, 60], proving that, even if the theoretical methods disagree, that this research field is still rich of physics to explore. The purely molecular effects, the role of autoionizating states, and the behavior of the cross sections when ATI is possible are an example of the open questions that need to be addressed in the future. Present results will be shown in Chapter 8.

This thesis is divided into two big parts. The first part describes all the theory necessary to understand the theoretical formalism used for this work. This part begins with a little introduction to all the chapters within. After that, the other part follows, containing the most significant results that were obtained during the duration of this thesis. It finishes with a chapter containing the most relevant conclusions, and what the future work in this field could be. Also, a brief description of the computational methods used is included in the appendix part.

Part I

Theory

This part of the thesis contains a brief description of the theory used for this thesis, as well as it points to the specific chapters where such theory is explained.

There are many ways of studying the ionization process of atoms and molecules. In particular, the theoretical method used for this study is a time independent perturbative treatment, which has its origins in a previous analysis used for electron-hydrogen atom ionization performed by Peterkop, Rudge and Seaton [1, 2]. This analysis will be introduced in Chapter 1. Also, in this Chapter 1, the definition of the photoionization Fully Differential Cross Section is introduced (FDCS). The FDCS describes the probability of ejection of the electrons in a given angle for a particular energy sharing of the excess energy between the ejected electrons. This FDCS can provide theoretical results, which can be directly compared with the results of the COLTRIMS experiments. All these FDCS expressions depend on the quantum amplitude of the ionization arrangement. The explanation of how to extract this amplitudes from the results of the calculations will shown in Chapter 3.

Firstly, it is necessary to describe the continuum wave functions. For this, an exact definition of the boundary conditions of the system is required, or a way to prevent such conditions. The Exterior Complex Scaling (ECS) ([61, 62, 63, 64, 28, 65]) method, which is an extension of the Complex Scaling (CS) method ([66, 67, 68, 69, 70, 71, 72, 73, 74]) is used to achieve the latter, and is explained in detail in Chapter 2. With the ECS technique is possible to obtain these scattering wave functions, which, within the complex scaling radius, have the correct asymptotic behavior.

Once such wave functions are obtained it is necessary to extract and combine the corresponding amplitudes that describe either the single or the double ionization processes. The process of extracting these amplitudes is explained in detail in Chapter 3. These amplitudes, in the case of a molecule, need to be calculated for a specific orientation of the molecule with respect to the polarization axis. As the calculations are done for a fixed value of ΔM (i.e. for the transition of a specific atom or molecular configuration to another of different total magnetic quantum number), the way the different amplitudes are combined is also explained in this chapter. From these amplitudes, it is then very easy to extract the fully differential cross sections mentioned above.

The scattering wave functions need a numerical representation that allow them to have a long range behavior, far from the center of mass, as they represent a wavefunction of a system in which one or two electrons are moving away from the nuclei. In order to represent them, two different

basis functions are used. Both of are them piecewise polynomials, defined in intervals, which can be extended to any given distance from the nuclei. Chapter 4 introduces the two types of these functions, B-Splines and FEM-DVR, used in this work.

With all these pieces together, the theoretical basis of this work is settled, and, so, it is possible to begin the interpretation of the results obtained.

CHAPTER 1

Time Independent Perturbative Treatment of Photoionization Processes

Perturbative treatments of the three body quantum breakup and ionization problems have been used for a long time. It was in the 1960s, when Peterkop and Rudge and Seaton ([1, 2]), deduced the boundary conditions for electron-hydrogen atom ionization, which set the grounds for the formal development of the perturbative treatment of such problems. The asymptotic form they derived was:

$$\Psi^{+}(\mathbf{r}_1, \mathbf{r}_2) = \Psi_0(\mathbf{r}_1, \mathbf{r}_2) + \Psi^{(sc)+}(\mathbf{r}_1, \mathbf{r}_2) \tag{1.1}$$

with

$$\Psi^{(sc)+}(\mathbf{r}_1, \mathbf{r}_2) \underset{\rho\to\infty}{\longrightarrow} f(\hat{r}_1, \hat{r}_2, \alpha)\sqrt{\frac{i\kappa^3}{\rho^5}}\exp\left(i\kappa\rho + i\frac{\zeta(\hat{r}_1 \cdot \hat{r}_2, \alpha)}{\kappa}\log 2\kappa\rho\right) \tag{1.2}$$

where $\mathbf{r}_1$ and $\mathbf{r}_2$ are the electronic coordinates, $\Psi_0(\mathbf{r}_1, \mathbf{r}_2)$ is the initial unperturbed state wavefunction, f is the ionization amplitude, and the hyperspherical coordinates are defined by $\rho = (r_1^2 + r_2^2)^{\frac{1}{2}}$ with $\alpha = \tan^{-1}(\frac{r_2}{r_1})$, and κ is related to the total energy by $E = \frac{\kappa^2}{2}$.

This asymptotic form does not provide a way to numerically compute the amplitude. In addition it is only valid in the far asymptotic region (where the three particles are separated). The coefficient $\zeta(\hat{r}_1 \cdot \hat{r}_2, \alpha)$ of the logarithmic phase is a function, both of the electron distances and of the angle between the two ejected electrons. The most complicated problem is the fact that this equation is not separable in spherical coordinates, making it inadequate for use in a numerical calculation, since the wave function for an atomic system is almost always expanded in partial waves.

There is another challenge in the formal theory mentioned by Peterkop, Rudge and Seaton. It is not possible to apply the ordinary expression to evaluate the amplitude starting from the scattering wavefunction that solves the Schrödinger equation, as, defined in the usual way, since this would have an infinite phase associated with integrating an expression with logarithmic phases over an infinite volume. Instead, the ionization amplitude for producing electrons (with momenta $\mathbf{k_1}$ and $\mathbf{k_2}$) is:

$$\begin{aligned} f(\mathbf{k_1}, \mathbf{k_2}) &= -(2\pi)^{5/2} e^{i\Delta(\mathbf{k_1}, \mathbf{k_2})} \\ &\int\int \Psi^+ (H - E)\phi(-\mathbf{k_1}, z_1)\phi(-\mathbf{k_2}, z_2) d\mathbf{r}_1 d\mathbf{r}_2 \end{aligned} \quad (1.3)$$

with effective charges z_1 and z_2 in the one-particle Coulomb function, $\phi(-\mathbf{k}, z)$ depending on both the energy and the direction of each electron. This expression satisfies the Peterkop condition,

$$\frac{z_1}{k_1} + \frac{z_2}{k_2} = \frac{1}{k_1} + \frac{1}{k_2} - \frac{1}{|\mathbf{k_1} - \mathbf{k_2}|} \quad (1.4)$$

with

$$\Delta(\mathbf{k_1}, \mathbf{k_2}) = 2[(\frac{z_1}{k_1}) \log(\frac{k_1}{\kappa}) + (\frac{z_2}{k_2}) \log(\frac{k_2}{\kappa})] \quad (1.5)$$

Practical approaches to an ab initio treatment of ionization have employed either approximate ionization boundary conditions, or have been designed to prevent them entirely. Exterior Complex Scaling is one of the latter, and will be discussed in the following chapters. There are other remarkable methods in the same context.

There have been several successful computational approaches to the three-body Coulomb problem based on solving the time-dependent Schrödinger equation, notably the "time-dependent close-coupling" approach of Pindzola, Schultz, Robicheux and coworkers [75, 76], who, based on the initial work of Bottcher [77], applied the method to electron impact double ionization $(e, 2e)$ and to photo double ionization $(\gamma, 2e)$ problems. Still, this method has the same problems when projecting into asymptotic states. It also has a big disadvantage when it comes to computational time, as it is a computationally quite demanding method.

Within the hyperspherical R-matrix method, with semiclassical outgoing waves (HRM-SOW) [78], the time-independent Schrödinger equation is solved without detailed specification of the three-body Coulomb boundary conditions by merging two different approaches: an *R-matrix* treatment of the two-electron system in the vicinity of the nucleus along with a semiclassical description of the evolution of the system in the asymptotic region [79, 80].

A lot of applications have been carried out by employing approximate two-body boundary conditions in solving the time-independent Schrödinger equation above the ionization threshold. The goal of these methods is to extend the close-coupling (CC) formalism, that has been available for over four decades as the basis for most *ab initio* works on calculating atomic excitation cross sections, to treat ionization.

In the CC method, the internal target states are used as a basis for expanding the full wavefunctions. Obviously, the target-states must be truncated in computations. For the close-coupling expansion to 'converge', the target states must approach completeness in the interaction region.

The success of these methods in computing total ionization cross sections is always tied to the completeness of the underlying basis and the unitary character of the close-coupling formalism. Convergence of the total ionization cross section is guaranteed by convergence of the discrete excitation cross sections, since the former can be obtained by subtracting the latter from the total cross section, which in turn can be obtained using the optical theorem. But, the computation of differential ionization cross sections is not guaranteed by the formalism, and additional assumptions are usually made.

The method that will be explained here is based on perturbation theory, with a complex rotation of the electronic coordinates in order to handle properly the boundary conditions, and using piecewise defined polynomial basis sets, which will be explained in detail later.

1.1 Photoionization cross section definitions

Unless specified otherwise, the MKS unit system will be used for the description of cross sections within this chapter.

In a process resulting int one or two electrons in the continuum the most detailed information is given by the fully differential cross section (FDCS), which depends on the direction of both electrons and on how they share the excess energy. Formally, the FDCS is proportional to the quantum amplitude of the ionization arrangement. This fully differential cross section, in the case of a double ionization problem, is called Triply Differential Cross Section (TDCS), as it is differential in how two electrons share the excess energy of the system, and also differential in the ejection angles of both electrons. Integrating over both ejection angles, i.e. $d\Omega_1$ and $d\Omega_2$, results in an expression that is called Single Differential Cross Section (SDCS) as it only depends on the energy sharing between the electrons. Integrating only over one of the ejection angles, is called Double Differential Cross Section

(DDCS), and it represents the probability of ejection of one electron into a given angle, irrespectively of the other.

Next is to provide a working expression for the fully differential cross section for an m-electron ejection by n-photons. It is defined by dividing the rate of ejection (transition rate) by the flux of photons which has units of photons/area/time:

$$\frac{d\sigma}{dEd\Omega_1...d\Omega_m} = \frac{W^{(n)}}{F^n}, \tag{1.6}$$

where F^n is the photon flux and $W^{(n)}$ is the ionization rate given by Fermi's golden rule formula:

$$W^{(n)} = \frac{2\pi}{\hbar}\left|\langle\Psi_0|V\frac{1}{E_0+\hbar\omega-H}\times...\times\frac{1}{E_0+(n-1)\hbar\omega-H}V|\Psi_{\mathbf{k_1},...,\mathbf{k_m}}\rangle\right|^2 \tag{1.7}$$

where Ψ_0 is the initial state, and $\Psi_{\mathbf{k_1},...,\mathbf{k_m}}$ the energy normalized final state with m electrons in the continuum. This definition is valid when the rate can be defined, that is, when the number of electrons ejected is linear in time, which is the perturbation theory result at all orders.

V is the photon-atom interaction potential in the dipole approximation, which, in the length gauge reads:

$$V = eE_0\boldsymbol{\epsilon}\cdot\mathbf{r}, \tag{1.8}$$

and in the velocity gauge:

$$V = \frac{eA_0\boldsymbol{\epsilon}\cdot\mathbf{p}}{m}, \tag{1.9}$$

where

$$E_0 = -\frac{\partial}{\partial t}A_0, \tag{1.10}$$

and

$$|E_0|^2 = \omega^2|A_0|^2. \tag{1.11}$$

The photon flux in terms of A_0 and E_0 is given by ([81, 82]):

$$F = \frac{c}{2\pi\hbar\omega}|E_0|^2 = \frac{c\omega}{2\pi\hbar}|A_0|^2 \tag{1.12}$$

Combining equations 1.6, 1.7, 1.8 and 1.9, yields for the length gauge:

$$\frac{d\sigma^{(n)}}{dEd\Omega_1...d\Omega_m} = \frac{2\pi}{\hbar}\frac{(e^2E_0^2)^n|\langle\Psi_0|\boldsymbol{\epsilon}\cdot\mathbf{r}\,(E_0+\hbar\omega-H)^{-1}...}{\left(\frac{c}{2\pi\hbar\omega}|E_0|^2\right)^n}$$
$$\frac{...\boldsymbol{\epsilon}\cdot\mathbf{r}\,(E_0+(n-1)\hbar\omega-H)^{-1}\,\boldsymbol{\epsilon}\cdot\mathbf{r}|\Psi_{\mathbf{k_1},...,\mathbf{k_m}}\rangle|^2}{\left(\frac{c}{2\pi\hbar\omega}|E_0|^2\right)^n} = 2\pi(2\pi\alpha)^n\omega^n\hbar^{2n-1}\times$$
$$\left|\langle\Psi_0|\boldsymbol{\epsilon}\cdot r\frac{1}{E_0+\hbar\omega-H}...\boldsymbol{\epsilon}\cdot\mathbf{r}\frac{1}{E_0+(n-1)\hbar\omega-H}\boldsymbol{\epsilon}\cdot\mathbf{r}|\Psi_{\mathbf{k_1},...,\mathbf{k_m}}\rangle\right|^2, \tag{1.13}$$

and in the velocity gauge

$$\frac{d\sigma^{(n)}}{dEd\Omega_1...d\Omega_m} = \frac{2\pi}{\hbar}\left(\frac{e^2A_0^2}{m^2}\right)^n\frac{|\langle\Psi_0|\boldsymbol{\epsilon}\cdot\mathbf{p}\,(E_0+\hbar\omega-H)^{-1}...}{\left(\frac{c\omega}{2\pi\hbar}|A_0|^2\right)^n}$$
$$\frac{...\boldsymbol{\epsilon}\cdot\mathbf{p}\,(E_0+(n-1)\hbar\omega-H)^{-1}\,\boldsymbol{\epsilon}\cdot\mathbf{p}|\Psi_{\mathbf{k_1},...,\mathbf{k_m}}\rangle|^2}{\left(\frac{c\omega}{2\pi\hbar}|A_0|^2\right)^n} = \frac{2\pi(2\pi\alpha)^n\hbar^{2n-1}}{\omega^n m^{2n}}\times$$
$$\left|\langle\Psi_0|\boldsymbol{\epsilon}\cdot\mathbf{p}\frac{1}{E_0+\hbar\omega-H}...\boldsymbol{\epsilon}\cdot\mathbf{p}\frac{1}{E_0+(n-1)\hbar\omega-H}\boldsymbol{\epsilon}\cdot\mathbf{p}|\Psi_{\mathbf{k_1},...,\mathbf{k_m}}\rangle\right|^2. \tag{1.14}$$

When the final state $\Psi_{\mathbf{k_1},...,\mathbf{k_m}}$ is momentum normalized it is necessary to multiply the above equations by the density of states:

$$\rho(\mathbf{k_1},...,\mathbf{k}_m) = \frac{m\mathbf{k}_1}{\hbar^2}...\frac{m\mathbf{k}_m}{\hbar^2} \tag{1.15}$$

Then the resulting expressions are:

$$\frac{d\sigma^{(n)}}{dEd\Omega_1...d\Omega_m} =$$
$$= 2\pi(2\pi\alpha)^n\omega^n\hbar^{2(m-n)-1}m^m\mathbf{k_1}...\mathbf{k_m}$$
$$\times\left|\langle\Psi_0|\boldsymbol{\epsilon}\cdot r\frac{1}{E_0+\hbar\omega-H}...\boldsymbol{\epsilon}\cdot\mathbf{r}\frac{1}{E_0+(n-1)\hbar\omega-H}\boldsymbol{\epsilon}\cdot\mathbf{r}|\Psi_{\mathbf{k_1},...,\mathbf{k_m}}\rangle\right|^2 \tag{1.16}$$

for the length gauge, and in the velocity gauge:

$$\frac{d\sigma^{(n)}}{dEd\Omega_1...d\Omega_m} =$$
$$= \frac{2\pi(2\pi\alpha)^n\hbar^{2(m-n)+1}}{\omega^n m^{2n-m}}$$
$$\times\left|\langle\Psi_0|\boldsymbol{\epsilon}\cdot p\frac{1}{E_0+\hbar\omega-H}...\boldsymbol{\epsilon}\cdot\mathbf{p}\frac{1}{E_0+(n-1)\hbar\omega-H}\boldsymbol{\epsilon}\cdot\mathbf{p}|\Psi_{\mathbf{k_1},...,\mathbf{k_m}}\rangle\right|^2 \tag{1.17}$$

From the general expressions (1.16) and (1.17) for the ejection of m electrons, one can substitute $m = 2$ for the case of the helium atom, or the hydrogen molecule (and it's isotopes) considered within this thesis work. Equivalently, n will be substituted by the total number of photons being studied.

1.1.1 Cross sections for the one-photon double-ionization

For the length gauge, substituting $m = 2$ and $n = 1$ in equation (1.16) results in:

$$\begin{aligned}\frac{d\sigma^{(1)}}{dEd\Omega_1 d\Omega_2} &= 2\pi(2\pi\alpha)\omega\hbar^{-2-1}m^2k_1k_2|f(\mathbf{k_1},\mathbf{k_2})|^2 \\ &= \frac{4\pi^2\alpha\omega m^2}{\hbar^3}k_1k_2|f(\mathbf{k_1},\mathbf{k_2})|^2, \end{aligned} \tag{1.18}$$

and for the velocity gauge (equation 1.17):

$$\begin{aligned}\frac{d\sigma^{(1)}}{dEd\Omega_1 d\Omega_2} &= \frac{2\pi(2\pi\alpha)m^{-2+2}}{\hbar^3\omega}k_1k_2|f(\mathbf{k_1},\mathbf{k_2})|^2 \\ &= \frac{4\pi^2\alpha}{\hbar^3\omega}k_1k_2|f(\mathbf{k_1},\mathbf{k_2})|^2. \end{aligned} \tag{1.19}$$

Taking into account that $\alpha = \frac{e^2}{\hbar c}$, and using atomic units, it follows for length gauge:

$$\frac{d\sigma^{(1)}}{dEd\Omega_1 d\Omega_2} = \frac{4\pi^2\omega}{c}k_1k_2|f(\mathbf{k_1},\mathbf{k_2})|^2, \tag{1.20}$$

and for the velocity gauge:

$$\frac{d\sigma^{(1)}}{dEd\Omega_1 d\Omega_2} = \frac{4\pi^2}{c\omega}k_1k_2|f(\mathbf{k_1},\mathbf{k_2})|^2. \tag{1.21}$$

1.1.2 Cross sections for the two-photon double-ionization

For the length gauge, substituting $m = 2$ and $n = 2$ in equation 1.16 leads to:

$$\begin{aligned}\frac{d\sigma^{(2)}}{dEd\Omega_1 d\Omega_2} &= 2\pi(2\pi\alpha)^2\omega^2\hbar^{2(2-2)-1}m^2k_1k_2|f(\mathbf{k_1},\mathbf{k_2})|^2 \\ &= \frac{8\pi^3\alpha^2\omega^2m^2}{\hbar}k_1k_2|f(\mathbf{k_1},\mathbf{k_2})|^2, \end{aligned} \tag{1.22}$$

and for the velocity gauge (equation 1.17):

$$\begin{aligned}\frac{d\sigma^{(1)}}{dEd\Omega_1 d\Omega_2} &= 2\pi(2\pi\alpha)^2\omega^{-2}\hbar^{2(2-2)-1}m^{-4+2}m^2k_1k_2|f(\mathbf{k_1},\mathbf{k_2})|^2 \\ &= \frac{8\pi^3\alpha^2}{\hbar\omega^2m^2}k_1k_2|f(\mathbf{k_1},\mathbf{k_2})|^2. \end{aligned} \tag{1.23}$$

Again, taking into account that $\alpha = \frac{e^2}{\hbar c}$, and using atomic units, the length gauge expression becomes:

$$\frac{d\sigma^{(2)}}{dE d\Omega_1 d\Omega_2} = \frac{8\pi^3 \omega^2}{c^2} k_1 k_2 |f(\mathbf{k_1}, \mathbf{k_2})|^2, \tag{1.24}$$

and in the velocity gauge:

$$\frac{d\sigma^{(2)}}{dE d\Omega_1 d\Omega_2} = \frac{8\pi^3}{c^2 \omega^2} k_1 k_2 |f(\mathbf{k_1}, \mathbf{k_2})|^2. \tag{1.25}$$

CHAPTER 2

Exterior Complex Scaling

Exterior Complex Scaling (ECS) is a method that allows the calculation of exact scattering wave functions, while removing the need to assume a specific functional form for the asymptotic behavior of the scattered wave. The only requirement that ECS imposes is that the solutions have to be purely outgoing.

The idea of complex coordinate scaling in the Schrödinger equation has its most notably origin in the early efforts made by Regge [66, 67, 68] in the late 1950s and early 1960s, who established the analytic properties of the *S-matrix* in the complex momentum and energy planes. The idea was to scale the radial coordinates by a complex phase factor:

$$r \rightarrow re^{i\theta} \tag{2.1}$$

Years later, the idea was taken in a formal context and extended to systems of particles interacting with Coulomb potentials by Balsev and Combes [70], Aguilar and Combes [71] and Simon [72].

One key point of all these works is to understand how this complex scaling affects the Hamiltonian. A consequence is that the continuous spectrum associated with each threshold is rotated in the energy plane, by a angle of 2θ, and, therefore, discrete resonances are revealed while bound state energies remain unchanged. Although resonances wavefunctions are not square integrable, under this scaling, their pure outgoing form $\psi_{res} \underset{r\rightarrow\infty}{\rightarrow} e^{(ik_{res}r)}$ becomes exponentially decaying, $\exp(i|k_{res}|e^{-i\alpha}re^{i\theta})$, and thus they become square integrable. The work of Doolen [73] led to a spread of the use of complex scaling in the calculation of resonance energies, (see e.g. the review by Reinhardt [74]). Also it allows for the study of the energies and lifetimes

of doubly excited states of H_2, [64].

Back into the scattering amplitudes context, it was in 1969 when Nuttall and Cohen [69] extended this ideas to the three-body problems above the breakup threshold. But, the problem of *regular* complex scaling is that it only could be applied to problems involving short-range potentials.

When calculating resonance energies, a problem arose in the first applications to molecular systems. In the Born-Oppenheimer approximation, the nuclear attraction potentials were not analytical after the complex transformation of equation (2.1). It was Simon [61] who suggested an exterior complex scaling (ECS) transformation to the coordinates of the Hamiltonian. Instead of rotating the whole coordinate plane, the idea was to rotate the coordinates at an angle of θ but only after a given point R_0:

$$r \rightarrow \begin{cases} r & \text{for} \quad r \leq R_0 \\ R_0 + (r - R_0)e^{i\theta} & \text{for} \quad r > R_0 \end{cases} \tag{2.2}$$

Inside the radius R_0, the wavefunctions will still real valued (see figure 2.1). But outside that radius, they can have a complex part. The basic idea appeared in a paper by Nicolaides and Beck in 1978 [83], but Simon showed one year later that the spectrum of the Hamiltonian under an ECS transformation such as (2.2) changes the same way as under the original complex scaling of equation (2.1).

The ECS transformation in equation (2.2) provides a method for imposing outgoing wave boundary conditions (setting $\theta \neq 0$ while enforcing the condition that on the ECS contour the wavefunction vanishes as $r \rightarrow \infty$). At the same time it yields the wave function in the interaction region where the amplitudes can be calculated. Under this scaling, the purely outgoing functions also decay exponentially, but only along the complex portion of the coordinate space. Thus, any outgoing wave will become a function with a finite extent. Therefore ECS provides a convenient way to compute collisional amplitudes. In problems involving more than one coordinate, the transformation should be applied to each of the coordinates.

It is important to note that in an exact or converged calculation, the solution of the Schrödinger equation does not depend on the value of θ, and it gives the physical solution for $r < R_0$. Thus, in an ECS calculation, it is an important convergence test to check if the results vary with the variation of θ.

This section will first show the main properties of the ECS transformed Hamiltonian, then a in depth study of the discontinuity at $r = R_0$, a key

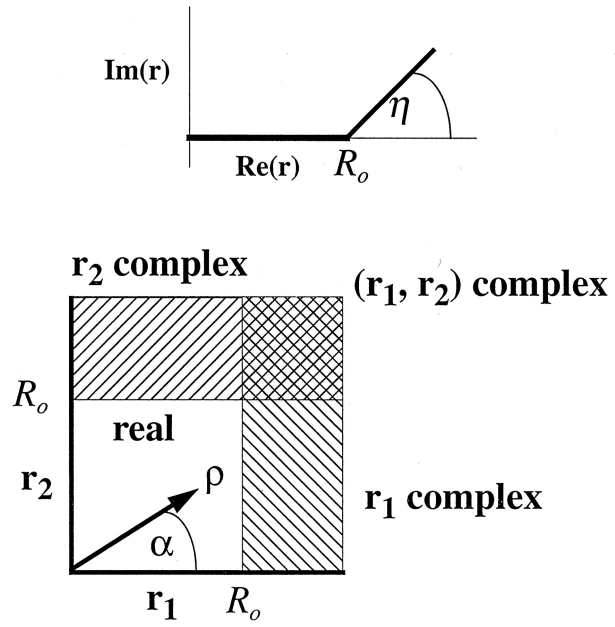

Figure 2.1: ECS applied to r in one and two dimensions

point in the process of building a numerically robust ECS implementation. In section 2.1 a case of arbitrary *smooth* ECS will be examined, where that discontinuity does not appear. Afterward, in section 2.3, a *sharp* ECS case will be shown.

2.1 ECS Hamiltonian properties

As described in [74], the main properties of the rotated Hamiltonian (H_θ) can be summarized as:

- Bound states associated with the rotated Hamiltonian (H_θ), are the same as those from the original Hamiltonian (H). Boundary conditions determine if an operator has eigenvalues and if its corresponding eigenvectors are square integrable (bound states) or not (scattering states). Taking as an example the *1s* hydrogen atom function, $R(r) = 2e^{-r}$, which is square integrable. When applying the ECS, $R(re^{i\theta}) = 2e^{-re^{i\theta}}$, it still is square integrable, under the restriction that $|\theta| \leq \frac{\pi}{2}$. Then, H and H_θ have the same eigenvalues and eigenvectors.

- The continuum spectrum branches of H_θ that begins in each scattering limit are rotated by an angle of 2θ.
  Continuum state wavefunctions are not square integrable. While the

potentials are not long-ranged, the radial *scattering* solutions are asymptotically ($r \to \infty$) written as linear combination of $\frac{e^{+i\vec{k}\vec{r}}}{r}$ and $\frac{e^{-i\vec{k}\vec{r}}}{r}$. To keep the same boundary conditions, when making the ECS transformation $k \to k^{-i\theta}$ should also be imposed. Then, $E \simeq= \frac{k^2}{2} \to e^{-2i\theta}\frac{k^2}{2}$ for the allowed *scattering* energies. Therefore, continuum states have an energy of $Ee^{2i\theta}$, and so, the continuum is rotated in the complex plane, as can be seen in the Figure 2.2.

- Isolated complex eigenvalues over the threshold correspond to resonances. Their characteristics can be directly extracted from the spectrum.

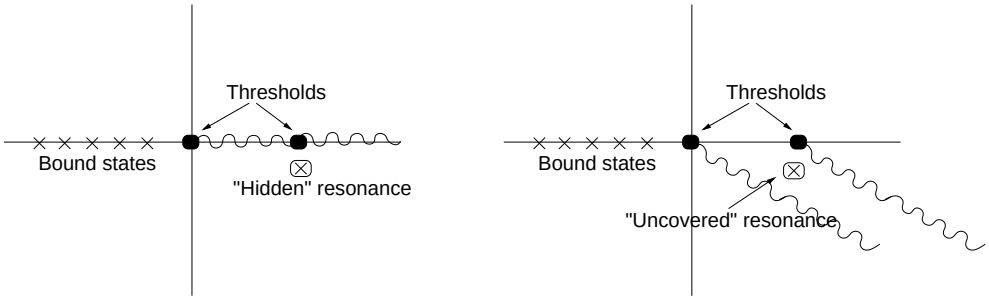

Figure 2.2: Hamiltonian spectra under ECS transformation

2.2 ECS for arbitrary complex coordinate contours

Consider a one dimension radial problem, in which a unique and continuous, but arbitrary, complex transformation of coordinate r is made. The operator (U) of the transformation reads:

$$U\Psi(r) = J(r)\Psi(R(r)), \tag{2.3}$$

where the Jacobian of the transformation is:

$$J(r) = \left(\frac{dR(r)}{dr}\right)^{\frac{1}{2}} \tag{2.4}$$

Considering the original Schrödinger equation

$$H\Psi(r) = E\Psi(r), \tag{2.5}$$

with the Hamiltonian

$$H = -\frac{1}{2\mu}\frac{d^2}{dr^2} + \frac{j(j+1)}{2\mu r^2} + V(r), \tag{2.6}$$

the transformed Schrödinger equation can be extracted from an unitary transformation:

$$UHU^{-1}U\Psi = EU\Psi. \tag{2.7}$$

The inverse of the transformation is given by

$$U^{-1}\Psi = \frac{1}{J(R^{-1}(r))}\Psi(R^{-1}(r)), \tag{2.8}$$

where $R^{-1}(r)$ is the inverse of the function that defines the complex contour. Representing the contour in the way suggested by Kurasov et al. [84]:

$$R(r) = \int_0^r q(r')dr' \tag{2.9}$$

such that $dR(r) = q(r)dr$ and the exterior complex scaling is specified by:

$$q(r) \to \begin{cases} 1 & \text{for} \quad r \to 0 \\ e^{i\eta} & \text{for} \quad r \to \infty \end{cases} \tag{2.10}$$

$R(r)$ becomes differentiable for all r.
The transformed Schrödinger equation then reads:

$$\widehat{H}\phi(r) = E\phi(r) \tag{2.11}$$

where $\phi(r) = \Psi(R(r))$. The transformed Hamiltonian becomes:

$$\widehat{H}(r) = -\frac{1}{2\mu}\left[\frac{1}{q(r)^2}\frac{d^2}{dr^2} - \frac{q'(r)}{q(r)^3}\frac{d}{dr}\right] + \frac{j(j+1)}{2\mu R(r)^2} + V(R(r)) \tag{2.12}$$

When doing a basis set expansion, the idea is to expand the transformed $\phi(r)$ and not $U\Phi(r)$ in a square integrable basis set L^2 $\chi_n(r)$. This way, the kinetic energy matrix elements are:

$$K_{mn} = -\frac{1}{2\mu}\int_0^\infty \chi_m(r)\left[\frac{1}{q(r)^2}\frac{d^2}{dr^2} - \frac{q'(r)}{q(r)^3}\frac{d}{dr}\right]\chi_n(r)q(r)dr \tag{2.13}$$

Given the definition that the χ_n vanish at the end of the grid, and integrating by parts, leads to:

$$H_{mn} = \frac{1}{2\mu}\int_0^\infty \chi'_m(r)\frac{1}{q(r)}\chi'_n(r)dr. \tag{2.14}$$

The kinetic energy matrix is then complex symmetric. Other matrix elements, where the operator is a function of $V(R(r))$, like for example the potential matrix elements read:

$$V_{mn} = \frac{1}{2\mu}\int_0^\infty \chi_m(r)V(R(r))\chi_n(r)q(r)dr \tag{2.15}$$

Thus the matrix representation of the Hamiltonian is complex symmetric for any contour defined by $q(r)$.

2.3 *Sharp* exterior scaling

Choosing the transformation given by 2.2, $q(r)$ will be:

$$q(r) \rightarrow \begin{cases} 1 & for \quad r \leq R_0 \\ e^{i\theta} & for \quad r > R_0 \end{cases} \tag{2.16}$$

Using this definition of $q(r)$ is obvious that the Jacobian

$$J(r) = q(r)^{\frac{1}{2}} \tag{2.17}$$

has a discontinuity at $r = R_0$ since $q(r)$ is discontinuous. The transformed wavefunction $\psi(r) = \Psi(R(r))$ is always continuous, but its first derivative with respect to r is not:

$$\frac{d}{dr}\psi(r) = \frac{dR(r)}{dr}\Psi'(R(r)) = q(r)\Psi'(R(r)) \tag{2.18}$$

The treatment of this discontinuity is always a critical point in the implementation of ECS, because the numerical convergence properties will depend on the representation of the wavefunction within R_0. As an advance the to next chapters, with the use of either B-Splines or DVR-FEM, the solution to this discontinuity problem is easy, because by just forcing the basis set to have an element boundary at $r = R_0$ is enough to guarantee the continuity of the wave function at R_0, while leaving a discontinuity in the derivative.

CHAPTER 3

Calculating amplitudes

Once the details of the Exterior Complex Scaling formalism are explained, the next step in the methodology is to extract the dynamic information that the calculated wavefunctions contains. This would be a major issue in other scattering methods, because the asymptotic boundary conditions that define the quantities of interest are used in the production of the wavefunction. In the ECS method, as the specification of the boundary conditions is avoided in the method itself, the wavefunction represents all the processes available at a specific total energy. The most practical approach to calculate the breakup cross sections is to formulate the problem in terms of integral expressions for the underlying scattering amplitudes. Another way to justify this is that it is necessary to obtain working expressions for the cross section definitions of Chapter 1, i.e. connecting equations (1.17) with those in (1.19) and (1.25). There are difficulties in evaluating these amplitudes on finite volumes, as they are using a finite grid representation used within ECS in this work. All difficulties are easily overcome, as shown in [62], where compact expressions are derived for several problems, such as breakup by electron impact, inelastic scattering and double photoionization. The working formalism for the double photoionization amplitude expressions is directly derived from the one that treats electron impact ionization. Therefore, the first part of this chapter will introduce the derivation of such expressions for the electron impact double ionization. After this, a partial-wave analysis, exploiting the spherical symmetry properties of the atomic case will be performed, followed by an amplitude and partial-wave analysis.

The following chapters will then adapt all this formulation to the problem of photo double ionization, firstly for the one photon double ionization of an atom, and secondly the expressions needed for two-photon double ionization of atoms will be derived. Then, the method will be extended for molecules,

and also for the two-photon double ionization of diatomic molecules.

With these calculated amplitudes it is possible to obtain the fully differential cross sections for each case, using the expressions of Chapter 1. These amplitudes, within the frame of double ionization, contains the information regarding the angular and kinetic energies of all the ejected electrons.

3.1 Amplitudes for breakup by electron impact

Since this ECS approach confines the interaction to a finite volume, the standard theory of rearrangement scattering [85] can be used, which is valid only for short-range interactions. This means that the Coulomb potentials are truncated at a large but finite distance.

The formal expression for the breakup amplitude for the case of short-range interactions reads:

$$\begin{aligned} f(\mathbf{k}_1,\mathbf{k}_2) &= \langle \mathbf{k}_1,\mathbf{k}_2|V + V(E-H+i\epsilon)^{-1}V_1|\Psi_0\rangle_{\rho_0} \\ &\equiv \langle \mathbf{k}_1,\mathbf{k}_2|V + VG^+(E)V_1|\Psi_0\rangle_{\rho_0} \end{aligned} \tag{3.1}$$

where the final state is simply a product of plane waves ($\langle \mathbf{r}|\mathbf{k}\rangle = \exp(i\mathbf{k}\cdot\mathbf{r})$) and Ψ_0 is the initial state, i.e. the product of a plane wave for the incident electron and the initial target state. It is to be understood that the matrix element is carried out over a large, but finite volume defined by some hyperradius ρ_0. All of the integrals in this sections are performed within that finite volume, so we henceforth omit the ρ_0 subscript. The potential V is the full interaction potential, i.e. $H = T + V$, while V_1 is the interaction operator defined by:

$$V_1|\Psi_0\rangle \equiv (H-E)|\Psi_0\rangle. \tag{3.2}$$

Using (3.2) the breakup amplitude becomes

$$\begin{aligned} f(\mathbf{k}_1,\mathbf{k}_2) &= \langle \mathbf{k}_1,\mathbf{k}_2|V[1+G^+(E)(H-E)]|\Psi_0\rangle \\ &= \langle \mathbf{k}_1,\mathbf{k}_2|V|\Psi^+\rangle \qquad (3.3) \\ &= \langle \mathbf{k}_1,\mathbf{k}_2|E-T|\Psi^+\rangle, \qquad (3.4) \end{aligned}$$

where $(H-E)\Psi^+ = 0$ has been taken into account. Splitting Ψ^+ into an incident and a scattered wave term $\Psi^+ = \Psi_0 + \Psi^{SC}$, the contribution from the incident term does not contribute to Eq.3.4, as it is proportional to δ functions between the incident and final momenta, which cannot be the same. Then:

$$\begin{aligned} f(\mathbf{k}_1,\mathbf{k}_2) &= \langle \mathbf{k}_1,\mathbf{k}_2|E-T|\Psi^{SC}\rangle \\ &= \langle \mathbf{k}_1,\mathbf{k}_2|E-T|G^+(H-E)\Psi_0\rangle \end{aligned} \tag{3.5}$$

The contributions of the parts of Ψ^{SC} that describe discrete, two-body channels, for an infinite volume, become proportional to δ functions between initial and final momenta and therefore vanish. On a finite volume they produce spurious contributions that make Eq.(3.5) unstable.

In order to eliminate this problem, one possible way is to use distorted waves to replace the plane-wave final states. If this distorted waves are chosen to be eigenfunctions of the target Hamiltonian, then there will be no spurious two-body contributions to the ionization amplitude, as the distorted waves and the discrete target states are orthogonal. To derive the working equations it is necessary to use the standard theory of rearrangement scattering. Starting by writing the full interaction as the sum of the one-body distorted wave potential, V_d:

$$\begin{aligned} V_d &= \upsilon_d(\mathbf{r}_1) + \upsilon_d(\mathbf{r}_2) \\ V &= V_d + \Delta V, \end{aligned} \tag{3.6}$$

the two-potential formula to express the full Green's function in terms of g_d^+, becomes:

$$G^+(E) = g_d^+(E) + g_d^+(E)\Delta V G^+(E). \tag{3.7}$$

Using the identity relationship:

$$(E - T)G^+(E) = 1 + VG^+(E), \tag{3.8}$$

(Eq.3.5) can be written as:

$$f(\mathbf{k}_1, \mathbf{k}_2) = \langle \mathbf{k}_1, \mathbf{k}_2 | [1 + V_d g_d^+(E)][1 + \Delta V G^+(E)](H - E)|\Psi_0\rangle. \tag{3.9}$$

where $[1 + V_d g_d^+(E)]$ is the wave operator for the potential V_d, which transforms the product $|k_1, k_2\rangle$ into a product of distorted waves $|\Phi_{k_1}^{d-}, \Phi_{k_2}^{d-}\rangle$. Thus the amplitude can be written in the 'two-potential' form:

$$f(\mathbf{k}_1, \mathbf{k}_2) = \langle \Phi_{\mathbf{k}_1}^{d-}, \Phi_{\mathbf{k}_2}^{d-} | (H - E)|\Psi_0\rangle + \langle \Phi_{\mathbf{k}_1}^{d-}, \Phi_{\mathbf{k}_2}^{d-} | \Delta V | \Psi^{SC}\rangle \tag{3.10}$$

The driven Schrödinger equation that defines Ψ^{SC}

$$(E - H)\Psi^{SC} = (H - E)\Psi_0, \tag{3.11}$$

is solved to obtain:

$$f(\mathbf{k}_1, \mathbf{k}_2) = \langle \Phi_{\mathbf{k}_1}^{d-}, \Phi_{\mathbf{k}_2}^{d-} | (E - T - V_d) | \Psi^{SC}\rangle \tag{3.12}$$

Using Green's theorem to express the last equation in terms of matrix elements with the kinetic energy operating on the left hand side, and the final

state being an eigenfunction with energy E of the $(T + V_d)$ operator, the only terms that do not disappear are the surface terms:

$$f(\mathbf{k}_1, \mathbf{k}_2) = \frac{1}{2} \int_S \left(\Phi_{\mathbf{k}_1}^{d-*} \Phi_{\mathbf{k}_2}^{d-*} \nabla \Psi^{SC} - \Psi^{SC} \nabla \Phi_{\mathbf{k}_1}^{d-*} \Phi_{\mathbf{k}_2}^{d-*} \right) \cdot d\hat{\mathbf{S}}. \tag{3.13}$$

Then the amplitude is only determined by the asymptotic behavior of Ψ^{SC} at $\rho = \rho_0$.

For problems with Coulomb interaction it has been suggested [86] to employ (3.12) or (3.13) by replacing $\Phi_{\mathbf{k}}^{d-*}$ by momentum normalized Coulomb functions. In this way, the distorting potential is

$$V_1 = -\frac{1}{r_1} - \frac{1}{r_2} \tag{3.14}$$

Formal theory in [1, 2, 4] state that expressions like (3.13) should have a divergent phase as the volume of integration becomes infinite. One can define the integral [4]:

$$I \equiv -\frac{1}{2} \lim_{S \to \infty} \int [\Psi \nabla \phi(z_1, -\mathbf{k}_1 | \mathbf{r}_1) \phi(z_2, - \\ \mathbf{k}_2 | \mathbf{r}_2) - \phi(z_1 - \mathbf{k}_1 | \mathbf{r}_1) \phi(z_2 - \mathbf{k}_2 | \mathbf{r}_2) \nabla \Psi] \cdot \hat{\mathbf{n}} dS \tag{3.15}$$

to calculate the amplitude for the six-dimensional volume integration in (3.12) for two electrons, such that it becomes a five-dimensional surface integral. Here, the functions $\phi(z - \mathbf{k}|\mathbf{r})$ are Coulomb functions with an effective charge z.

Integrating (3.15) using the stationary-phase approximation reveals a divergent phase depending on the radius of the bounding surface. To eliminate this phase, the formal theory requires that the effective charges z_1 and z_2 satisfy the Peterkop relation [87] (1.4), which is momentum and direction dependent:

$$\frac{Z_1}{k_1} + \frac{Z_2}{k_2} = \frac{1}{k_1} + \frac{1}{k_2} - \frac{1}{|\mathbf{k}_1 - \mathbf{k}_2|} \tag{3.16}$$

With this condition the electron impact amplitude is given by the same expression as in (1.3):

$$f(\mathbf{k_1}, \mathbf{k_2}) = -(2\pi)^{5/2} e^{i\Delta(\mathbf{k_1}, \mathbf{k_2})} \int \int \Psi^+ (H - E) \phi(-\mathbf{k_1}, z_1) \phi(-\mathbf{k_2}, z_2) dr_1 dr_2 \tag{3.17}$$

with the finite phase:

$$\Delta(k_1, k_2) = 2[(\frac{z_1}{k_1}) \log(\frac{k_1}{\kappa}) + (\frac{z_2}{k_2}) \log(\frac{k_2}{\kappa})] \tag{3.18}$$

where $\kappa = \sqrt{k_1^2 + k_2^2}$.

3.1.1 Partial-wave analysis of breakup amplitudes

By using the spherical symmetry of an atom, it is possible to reduce the combinations of amplitudes and to calculate on an arc in the $[r_1, r_2]$ plane of coordinates.
In the case of electron-impact ionization the driven Schrödinger equation to solve is (3.11):

$$(E - H)\Psi^{SC}(\mathbf{r}_1, \mathbf{r}_2) = (H - E)\Psi_0(\mathbf{r}_1, \mathbf{r}_2) \tag{3.19}$$

Both Ψ_0 and Ψ^{SC} can be expanded in generalized spherical harmonics using Clebsh-Gordon coefficients (using Edmonds notation [88]):

$$\mathcal{Y}^{L,M}_{\ell_1,\ell_2}(\hat{\mathbf{r}}_1, \hat{\mathbf{r}}_2) = \sum_{m_1,m_2} (\ell_1 m_1 \ell_2 m_2 | \ell_1 \ell_2 L M) Y_{\ell_1,m_1}(\hat{\mathbf{r}}_1) Y_{\ell_2,m_2}(\hat{\mathbf{r}}_2) \tag{3.20}$$

or Wigner $3j$ symbols:

$$\mathcal{Y}^{L,M}_{\ell_1,\ell_2}(\hat{\mathbf{r}}_1, \hat{\mathbf{r}}_2) = \sum_{m_1,m_2} (-1)^{\ell_2-\ell_1-M}(2L+1)^{1/2} \begin{pmatrix} \ell_1 & \ell_2 & L \\ m_1 & m_2 & -M \end{pmatrix} Y_{\ell_1,m_1}(\hat{\mathbf{r}}_1) Y_{\ell_2,m_2}(\hat{\mathbf{r}}_2) \tag{3.21}$$

For example, for the ionization of the hydrogen atom in its 1s ground state:

$$\Psi_0 = \sqrt{\frac{k_i}{4\pi}} \frac{1}{\sqrt{2}} [\Phi_{1s}(\mathbf{r}_1) e^{i\mathbf{k}_i \cdot \mathbf{r}_2} + (-1)^S \Psi_{1s}(\mathbf{r}_2) e^{i\mathbf{k}_i \cdot \mathbf{r}_1}] = \sum_{L=0}^{\infty} \frac{i^L}{r_1 r_2} \sqrt{\frac{2L+1}{2k_i}} \times [\Phi_{1s}(r_1) j_L(k_i r_2) \mathcal{Y}^{L0}_{0L}(\hat{\mathbf{r}}_1, \hat{\mathbf{r}}_2) + (-1)^S \Psi_{1s}(r_2) j_L(k_i r_1) \mathcal{Y}^{L0}_{L0}(\hat{\mathbf{r}}_1, \hat{\mathbf{r}}_2)] \tag{3.22}$$

the expansion for the scattered wave function without M-mixing becomes:

$$\Psi^{SC} = \sum_{L,\ell_1,\ell_2} \frac{i^L}{r_1 r_2} \psi^L_{\ell_1 \ell_2}(r_1, r_2) \mathcal{Y}^{L0}_{\ell_1 \ell_2}(\hat{\mathbf{r}}_1, \hat{\mathbf{r}}_2) \tag{3.23}$$

The Schrödinger equation (3.19) therefore reduces to a coupled two-dimensional equation for the radial functions $\psi^L_{\ell_1 \ell_2}(r_1, r_2)$. To evaluate the ionization amplitude using the surface integral of Eq.(3.13) the partial wave expansion of the Coulomb function is also needed:

$$\Phi^-_{\mathbf{k}}(\mathbf{r}) = \sum_{m=-\ell}^{\ell} \frac{i^\ell e^{-i\eta_\ell(k)}}{kr} \varphi^{(c)}_\ell(k, r) Y^*_{\ell,m}(\hat{\mathbf{k}}) Y_{\ell,m}(\mathbf{r}) \tag{3.24}$$

where the radial Coulomb function, $\varphi_\ell^{(c)}(k,r)$ has the asymptotic behavior

$$\varphi_\ell^{(c)}(k,r) \to \sin\left(kr + \frac{Z}{k}\log 2kr - \frac{\pi\ell}{2} + \eta_\ell(k)\right) \tag{3.25}$$

with

$$\eta_\ell(k) = \arg\Gamma(\ell + 1 - i/k) \tag{3.26}$$

Substituting equations (3.23) and (3.24) into equation (3.13) the following expression for the ionization amplitude arises:

$$f(\mathbf{k}_1,\mathbf{k}_2) = \sum_{L,\ell_1,\ell_2} i^{L-\ell_1-\ell_2} e^{i(\eta_{\ell_1}(k_1)+\eta_{\ell_2}(k_2))} f^L_{\ell_1,\ell_2}(k_1,k_2)\mathcal{Y}^{L0}_{\ell_1\ell_2}(\hat{\mathbf{k}}_1,\hat{\mathbf{k}}_2) \tag{3.27}$$

where

$$f^L_{\ell_1,\ell_2}(k_1,k_2;\rho_0) = \frac{\rho_0}{2k_1k_2}\int_0^{\pi/2} d\alpha(\varphi^{(c)}_{\ell_1}(k_1,r_1)\varphi^{(c)}_{\ell_2}(k_2,r_2)\frac{d}{d\rho}\psi^L_{\ell_1,\ell_2} - \psi^L_{\ell_1,\ell_2}\frac{d}{d\rho}[\varphi^{(c)}_{\ell_1}(k_1,r_1)\varphi^{(c)}_{\ell_2}(k_2,r_2)])|_{\rho=\rho_0}. \tag{3.28}$$

3.2 Amplitudes for single photon double photoionization of an atom: He

Following through the electron-impact formulation, the method of the previous section can be adapted to photonic ionization. The first step will be to modify the electron impact formalism to the case of one photon double ionization of a helium atom. In this process, an atom absorbs one photon and ejects two electrons in the continuum, leading to a final state with three unbound charged particles. In the weak-field limit, this process is described by an amplitude that is a matrix element of the dipole operator between the initial target wavefunction and a final state involving a doubly charged ion and two free electrons. Using the velocity form of the dipole operator:

$$\mathcal{F}(\mathbf{k}_1,\mathbf{k}_2) = \langle\Psi^-_{\mathbf{k}_1,\mathbf{k}_2}|\epsilon\cdot(\nabla_1+\nabla_2)|\Psi_0\rangle \tag{3.29}$$

where ϵ is the polarization vector, and $|\Psi_0\rangle$ is the initial bound state of the atom. The final state wavefunction, $\Psi^-_{k_1,k_2}$, has both electrons in the continuum. In this case, it would be necessary to solve a driven Schrödinger equation for each energy sharing between the final state photo-electrons. A better way is to begin with the first order equation describing single-photon absorption by a two electron atom in the velocity gauge, and choosing the z-axis along the polarization vector:

$$(E_0+\omega-H|\Psi^+_1\rangle = \boldsymbol{\epsilon}\cdot(\nabla_1+\nabla_2)|\Psi_0\rangle = \left(\frac{\partial}{\partial z_1}+\frac{\partial}{\partial z_2}\right)|\Psi_0\rangle \tag{3.30}$$

The asymptotic form of the solution of this equation can be written in analogy with Rudge's formal analysis of the electron-impact ionization problem [4]:

$$\Psi^{+}_{SC} \to -i^{1/2}\left(\frac{K^3}{\rho^5}\right)^{1/2}\mathcal{F}(r_1,r_2,\alpha)e^{iK\rho+i(\zeta/K)\log(2K\rho)} \tag{3.31}$$

where $\mathcal{F}$ is proportional to the ionization amplitude. The hyperradius ρ, the hyperangle α, and magnitude of the total momentum K, are given by:

$$\begin{aligned}\rho &= \sqrt{r_1^2+r_2^2}\\ \alpha &= \tan^{-1}(r_2/r_1)\\ K &= \sqrt{k_1^2+k_2^2}\end{aligned} \tag{3.32}$$

The angle dependence of the logarithmic phase is:

$$\frac{\zeta(r_1,r_2,\alpha)}{\rho} = \frac{2}{r_1}+\frac{2}{r_2}-\frac{1}{r_{12}}. \tag{3.33}$$

The most efficient approach for two particle problems within ECS method is to write the amplitude as a surface integral on a surface within the volume enclosed by the exterior scaling radius R_0 [89, 86]. This way the amplitude can be written as:

$$f(\mathbf{k}_1,\mathbf{k}_2) = \langle\Phi^{(-)}_{z_1}(\mathbf{k}_1,\mathbf{r}_1)\Phi^{(-)}_{z_2}(\mathbf{k}_1,\mathbf{r}_1)|E-T-V_1|\Psi^{+}_{SC}\rangle \tag{3.34}$$

where E is the total energy, T is the two electron kinetic-energy operator and V_1 is the sum of all one-electron potentials,

$$V_1 = -\frac{Z_1}{r_1}-\frac{Z_2}{r_2} \tag{3.35}$$

The $\Phi^{(-)}_{z_i}(\mathbf{k},\mathbf{r})$ are Coulomb functions normalized to a δ function in momentum space, with effective charges Z_i.
In order to relate amplitude in (3.34) with the amplitude $\mathcal{F}$ in (3.29), it is possible to follow Rudge's analysis, and do integrate over stationary phases. With Rudge's equation (equation (2.52) in [2]) (regarding a factor of $(2\pi)^3$ that comes from the fact that the Coulomb functions here are momentum normalized, and with an volume-dependent overall phase that arises because "Peterkop conditions" are not enforced):

$$\mathcal{F}(\mathbf{k}_1,\mathbf{k}_2,\beta) = -(2\pi)^{1/2}\chi(\mathbf{k}_1,\mathbf{k}_2,\rho)f(\mathbf{k}_1,\mathbf{k}_2) \tag{3.36}$$

with $\chi(\mathbf{k}_1,\mathbf{k}_2,\rho)$ being the volume-dependent overall phase:

$$\begin{aligned}\chi(\mathbf{k}_1,\mathbf{k}_2,\rho) = e^{-2iZ_2\log(k_2/K)/k_2}e^{-2iZ_1\log(k_1/K)/k_1}\\ \times e^{i[\zeta(k_1,k_2,\beta)/K-Z_1/k_1-Z_2/k_2]\log(2K\rho)\log(k_2/J)/k_2}\end{aligned} \tag{3.37}$$

The ζ function:

$$\zeta(k_1, k_2, \beta)/K = \frac{1}{k_1} + \frac{1}{k_2} - \frac{1}{|\mathbf{k}_1 - \mathbf{k}_2|} \tag{3.38}$$

parametrizes the asymptotic momentum distribution of the photo-ejected electrons with $\beta = \tan^{-1}(k_2/k_1)$. The main idea of the Peterkop condition is to eliminate this volume-dependent phase by choosing Z_1 and Z_2 according to:

$$\frac{Z_1}{k_1} + \frac{Z_2}{k_2} = \frac{1}{k_1} + \frac{1}{k_2} - \frac{1}{|\mathbf{k}_1 - \mathbf{k}_2|} \tag{3.39}$$

This way the last exponent in Eq.(3.37) disappears.

With the analysis of McCurdy, Horner and Rescigno [86] for electron-impact ionization, and the analysis of Baertschy et al [90], it is possible to evaluate the amplitude $f(k_1, k_2)$ by calculating the integral of Eq.(3.34) on a finite volume, given the solution for Ψ^+_{SC}. For that, it is necessary to choose both the effective charges to be equal to the nuclear charge:

$$Z_1 = Z_2 = 2 \tag{3.40}$$

so, taking into account the properties of the Coulomb functions, the contributions from the discrete single-ionization channels are eliminated [89, 86]. This allows for using an exterior scaling radius of few tenths of Bohr radii for this problem.

3.2.1 Representation of Ψ_{SC}

In a calculation using either DVR or B-Splines within the ECS approach, Ψ^+_{SC} is represented by a use of configuration interaction:

$$\Psi^+_{SC} = \sum_{n,m,l_1<l_2} C_{nl_1,ml_2} \Phi_{n,l_1,m,l_2} \tag{3.41}$$

where the C_{nl_1,ml_2} are the configuration interaction coefficients. The configurations are defined by the total angular momentum L with upper sings corresponding to singlet and lower signs corresponding to triplet spin coupling:

$$\begin{aligned}\Phi_{n,l_1,m,l_2} = \frac{1}{\sqrt{2}} \frac{1}{r_1 r_2} [\varphi_{n,l_1}(r_1)\varphi_{m,l_2}(r_2)\mathcal{Y}^{L,M}_{l_1,l_2}(\Omega_1, \Omega_2) \\ \pm \varphi_{m,l_2}(r_1)\varphi_{n,l_1}(r_2)\mathcal{Y}^{L,M}_{l_2,l_1}](\Omega_1, \Omega_2) \frac{\alpha(1)\beta(2) \mp \beta(1)\alpha(2)}{\sqrt{2}}\end{aligned} \tag{3.42}$$

where $r^{-1}\varphi_{n,l}(r)$ denotes a normalized radial "orbital" associated with the indices n, l.

For the spherically symmetric ^1S initial state and linear polarization of the light it is possible to choose the z-axis to coincide with the polarization vector ϵ. Therefore the final state must have the symmetry $^1P_0$, with $M = 0$ with respect to the z-axis, because the dipole operator, for example, in the length representation, $\epsilon \cdot \mathbf{r}$, is proportional to $Y_{1,0}(\hat{\mathbf{r}})$. Thus, for the case of double ionization of the helium ground state, $L = 1$ and $M = 0$ in Eq.(3.42).

The scattering wave function can be written splitting the direct and exchange contribution coming from the direct part of the CI configurations in 3.42

$$\Psi^+_{SC} = \sum_{l_1<l_2} [\psi^{dir}_{l_1,l_2}(r_1,r_2)\mathcal{Y}^{L,M}_{l_1,l_2}(\Omega_1,\Omega_2) \pm \psi^{exch}_{l_1,l_2}(r_1,r_2)\mathcal{Y}^{L,M}_{l_2,l_1}(\Omega_1,\Omega_2)] \quad (3.43)$$

The coupled generalized spherical harmonics are defined as before for the electron-atom scattering, in equations (3.20) and (3.21). This splitting will prove useful in the partial wave analysis that will be performed in the next section.

3.2.2 Partial-wave analysis

The decomposition in partial waves of the amplitude corresponding to the one photon double ionization can be carried out exactly the same way as for the electron impact ionization.

As mentioned previously, in the ECS scheme, it is more efficient to compute breakup amplitudes as surface integrals over a volume just inside the exterior scaling radius R_0.

For this it is necessary to evaluate explicitly the integral expression for the double-ionization amplitude:

$$f(\mathbf{k}_1,\mathbf{k}_2) = \langle \Phi^{(-)}(\mathbf{k}_1,\mathbf{r}_1)\Phi^{(-)}(\mathbf{k}_2,\mathbf{r}_2)|E - T - V_1|\Phi^+_{SC}\rangle \quad (3.44)$$

where $\Phi^{(-)}(\mathbf{k},\mathbf{r})$ denotes a Coulomb function with momentum normalization and nuclear charge $Z = 2$ as before. This function is related to the outgoing boundary conditions by $\Phi^{(-)}(\mathbf{k},\mathbf{r}) = [\Phi^{(+)}(-\mathbf{k},\mathbf{r})]^*$, and its partial wave expansion is given by [85]:

$$\Phi^{(-)}(\mathbf{k},\mathbf{r}) = \left(\frac{2}{\pi}\right)^{1/2} \sum_{l,m} \frac{i^l e^{-i\eta_l}}{kr} \phi^{(c)}_{kl}(r) Y_{lm}(\hat{\mathbf{r}}) Y^*_{lm}(\hat{\mathbf{k}}) \quad (3.45)$$

there the radial Coulomb function, $\varphi^{(c)}_\ell(k,r)$ has the asymptotic behavior

$$\phi^{(c)}_{kl}(r) \to \sin\left(kr + \frac{Z}{k}\log 2kr - \frac{\pi l}{2} + \eta_l(k)\right) \quad (3.46)$$

with

$$\eta_l(k) = \arg\Gamma(l+1-i/k) \tag{3.47}$$

Applying Eqs.(3.45) and (3.41) and Eq.(3.42), to Eq.(3.44) leads to the working equation for the ionization amplitude $f(k_1,k_2)$ in terms of the direct and exchange partial-wave amplitudes:

$$f(\mathbf{k}_1,\mathbf{k}_2) = \sum_{l_1<l_2} i^{-(l_1+l_2)}[e^{i\eta_{l_1}(k_1)+i\eta_{l_2}(k_2)}\mathcal{F}^{dir}_{l_1l_2k_1k_2}\mathcal{Y}^{L,M}_{l_1,l_2}(\mathbf{k}_1,\mathbf{k}_2) \pm e^{i\eta_{l_1}(k_2)+i\eta_{l_2}(k_1)}\mathcal{F}^{exch}_{l_1l_2k_1k_2}\mathcal{Y}^{L,M}_{l_2,l_1}(\hat{\mathbf{k}}_1,\hat{\mathbf{k}}_2)] \tag{3.48}$$

The double-ionization amplitude has two contributions, one from the direct part and the other from the exchange part of each of the configurations in equation (3.42). The l_i indices are reversed in the coupled generalized spherical harmonics in the exchange contribution and the k's and l's appear differently in the direct and the exchange contributions. The vector coupling coefficients are then used to recombine the resulting terms to give coupled generalized spherical harmonics that are functions of the angles of ejection corresponding to the two momenta $\mathbf{k}_1$ and $\mathbf{k}_2$.

Focusing on the two-potential form of V_1 in Eq.(3.35), the one-electron radial Hamiltonian can be written as:

$$h_i = -\frac{1}{2}\frac{d^2}{dr_i^2} + \frac{l(l+1)}{2r_i^2} - \frac{2}{r_i} \tag{3.49}$$

The partial-wave amplitudes in Eq.(3.48) are given by:

$$\begin{aligned}\mathcal{F}^{dir}_{l_1l_2k_1k_2} &= \frac{2}{\pi}\frac{1}{k_1k_2}\frac{1}{\sqrt{2}}\sum_{n,m} C_{nl_1ml_2}\langle\phi^{(c)}_{k_1l_1}\phi^{(c)}_{k_2l_2}|E-h_1-h_2|\varphi_{nl_1}\varphi_{ml_2}\rangle \\ &= \frac{2}{\pi}\frac{1}{k_1k_2}\frac{1}{\sqrt{2}}\times \\ &\sum_{n,m} C_{nl_1ml_2}\int dr_1dr_2\phi^c_{k_1l_1}(r_1)\phi^c_{k_2l_2}(r_2)(E-h_1-h_2)\varphi_{nl_1}(r_1)\varphi_{ml_2}(r_2)\end{aligned} \tag{3.50}$$

and

$$\begin{aligned}\mathcal{F}^{exch}_{l_1l_2k_1k_2} &= \frac{2}{\pi}\frac{1}{k_1k_2}\frac{1}{\sqrt{2}}\sum_{n,m} C_{nl_1ml_2}\langle\phi^{(c)}_{k_1l_2}\phi^{(c)}_{k_2l_1}|E-h_1-h_2|\varphi_{ml_2}\varphi_{nl_1}\rangle \\ &= \frac{2}{\pi}\frac{1}{k_1k_2}\frac{1}{\sqrt{2}}\times \\ &\sum_{n,m} C_{nl_1ml_2}\int dr_1dr_2\phi^c_{k_1l_2}(r_1)\phi^c_{k_2l_1}(r_2)(E-h_1-h_2)\varphi_{ml_2}(r_1)\varphi_{nl_1}(r_2)\end{aligned} \tag{3.51}$$

The two-potential formulas of equations (3.50) and (3.51) have also an equivalent surface integral representation, which appears upon the application of the Green's theorem. By using the hyperspherical coordinates defined in Eq.(3.32), they can be written as integrals over a surface with hyperradius $\rho = \rho_0$, which defines the volume in $\mathbf{r}_1$ and $\mathbf{r}_2$ for the integration:

$$\begin{aligned}
&\langle \phi^{(c)}_{k_1 l_1} \phi^{(c)}_{k_2 l_2} | E - h_1 - h_2 | \varphi_{n l_1} \varphi_{m l_2} \rangle \\
&= \frac{\rho_0}{2} \int_0^{\pi/2} \Bigg[\phi^{(c)}_{k_1 l_1}(r_1) \phi^{(c)}_{k_2 l_2}(r_2) \frac{\partial}{\partial \rho} \varphi_{n l_1}(r_1) \varphi_{m l_2}(r_2) - \\
&\varphi_{n l_1}(r_1) \varphi_{m l_2}(r_2) \frac{\partial}{\partial \rho} \phi^{(c)}_{k_1 l_1}(r_1) \phi^{(c)}_{k_2 l_2}(r_2) \Bigg] \Bigg|_{\rho=\rho_0} d\alpha
\end{aligned} \tag{3.52}$$

and

$$\begin{aligned}
&\langle \phi^{(c)}_{k_1 l_2} \phi^{(c)}_{k_2 l_1} | E - h_1 - h_2 | \varphi_{m l_2} \varphi_{n l_1} \rangle \\
&= \frac{\rho_0}{2} \int_0^{\pi/2} \Bigg[\phi^{(c)}_{k_1 l_2}(r_1) \phi^{(c)}_{k_2 l_1}(r_2) \frac{\partial}{\partial \rho} \varphi_{m l_2}(r_1) \varphi_{n l_1}(r_2) - \\
&\varphi_{m l_2}(r_1) \varphi_{n l_1}(r_2) \frac{\partial}{\partial \rho} \phi^{(c)}_{k_1 l_2}(r_1) \phi^{(c)}_{k_2 l_1}(r_2) \Bigg] \Bigg|_{\rho=\rho_0} d\alpha
\end{aligned} \tag{3.53}$$

In a practical calculation ρ_0 is chosen to be just inside R_0; typically a few tenths of a Bohr radius smaller than R_0. Equations (3.52) and (3.53) are the working equations with which the double-ionization amplitudes are calculated.

3.3 Amplitudes for two photon double photoionization of an atom: He

The scheme to study the ionization for more than one photon within the perturbation theory ECS formulation, is to solve as many driven equations like (3.30) as photons are being treated. Starting from an initial state, and then reinjecting the solution of each driven equation as the initial state for the next photon interaction. The two-photon double ionization results in the two coupled equations:

$$(E_0 + \hbar\omega - H)\Psi_1^{SC}(\mathbf{r}_1, \mathbf{r}_2) = \mu \Phi_0 \tag{3.54}$$

$$(E_0 + 2\hbar\omega - H)\Psi_2^{SC}(\mathbf{r}_1, \mathbf{r}_2) = \mu \Psi_1^{SC} \tag{3.55}$$

where Φ_0 and E_0 represent both the initial state wavefunction and energy, ω is the photon energy, and Ψ_1^{SC} and Ψ_2^{SC} are the first photon and second photon wavefunction respectively. The dipole operator, μ, is defined in terms of the momentum operators $\mathbf{p}_i$ for the two electrons, $\mu = \mu_1 + \mu_2 = \boldsymbol{\epsilon}\cdot\mathbf{p}_1 + \boldsymbol{\epsilon}\cdot\mathbf{p}_2$. As it can be seen, the first photon wavefunction, results from the first driven equation and is then reused as the initial state for the second photon interaction.

Once these coupled driven equations have been solved, the same strategy for obtaining the one-photon amplitude must be used, i.e. using momentum normalized one-electron Coulomb functions with a nuclear charge $Z = 2$ for the case of helium.

But there is a problem that is not present for the one-photon double ionization of helium. It arises from the fact that, for photon energies higher than the first ionization potential of the atom, the first photon scattered wavefunction, $\Psi_1^{SC}(\mathbf{r}_1, \mathbf{r}_2)$ solution of Eq.3.54, will have single ionization terms, that, at large real values of the electron coordinates, behave like the symmetrized product of a bound state of He^+ times an undamped outgoing wave in the other electron coordinate. This condition appears when the first photon already ionizes the atom and, in consequence, the second photon absorption has a initial state from a already ionized system. This is called above threshold ionization (ATI).

This implies that $\mu\Psi_1^{SC}$, which is the driving term for the second photon equation Eq.(3.55), will not vanish as $\mathbf{r}_1, \mathbf{r}_2 \to \infty$. Since the dipole operator μ is a one-body operator, the second photon equation will be ill-conditioned, irrespective of the gauge being used, and the ionization amplitudes extracted from Ψ_2^{SC} will not converge with increasing volume, rendering this method inappropriate. However, there is a simple way to circumvent this problem by adding a small, positive imaginary part to ω only in the first photon equation Eq.(3.54) which will produce a solution Ψ_1^{SC} with an exponential fall-off for large r-values. This new Ψ_1^{SC} can then be used as a valid driving term to solve the second photon equation, leading to convergent amplitudes that can be numerically extrapolated to real photon energies. Thus, equations (3.54) and (3.55) must be solved for different complex values of ω in the first equation, and then, numerically extrapolate to a pure real photon energy all the different amplitudes resulting from solving the second photon equation with different Ψ_1^{SC}, which come from solving the first photon equation with different values of the complex part of ω.

This 'complex' photon energy calculations can be summarized in the following scheme:

- Solve equation (3.54) for different 'complex' values of ω, i.e. for values like: $\omega' = (\omega, [0.025 : 0.5])$.
- Using each individual Ψ_1^{SC} wavefunction to solve equation (3.55).
- Extract the amplitudes for each imaginary part of the ω dependent Ψ_2^{SC}.
- Extrapolate to $\Im[\omega] = 0$ using all the resulting amplitudes of the last step.

A convenient extrapolating method is to plot the amplitudes as a function of the imaginary part of ω, and using a numerical analysis in order to find an appropriate fitting function. For example, in all the ECS two-photon double ionization calculations of He shown in this thesis, a third order polynomial was used.

The choice of the lowest value of $\Im[\omega]$ to include in the fitting depends on R_0. There is always a small interval in the vicinity of $\Im[\omega] = 0$ where the calculated amplitudes are incorrect. In this interval the amplitudes deviate rapidly from their smooth behavior in the rest of the complex ω-plane. These deviating amplitudes are the ones that should be removed from the fit. For larger values of R_0, the interval for ω around $\omega = 0$ in which the amplitudes are unphysical becomes smaller (the physical limit of $\Im[\omega] = 0$ is reached when $R_0 = \infty$). So a practical way to eliminate those contributions is to choose a large enough value of R_0, while, using different values of R_0 it is easy to spot which amplitudes should not be included in the fit.

3.4 Amplitudes for one photon double photoionization of a molecule: H_2

The amplitude for the one photon double ionization is associated with the purely outgoing wavefunction Ψ_{SC}^{+} solution of the driven Schrödinger equation (3.29), with the proper Hamiltonian.

A expression similar to Eq.(3.34) must be used for the molecular case. As the ionization process is much faster than the nuclear movement, the Born-Oppenheimer approximation will be used, in which the nuclear movement is not taken into account. The expression for a fixed internuclear distance then becomes [65]:

$$f(\mathbf{k}_1, \mathbf{k}_2) = \langle \Phi^{(-)}(\mathbf{k}_1, \mathbf{r}_1)\Phi^{(-)}(\mathbf{k}_2, \mathbf{r}_2)|[E - T - v(r_1) - v(r_2)]|\Psi_{SC}^{+}(\mathbf{r}_1, \mathbf{r}_2)\rangle, \tag{3.56}$$

where E is the excess energy above the double ionization threshold, T is the two-electron kinetic operator, and $v(r)$ is the nuclear attraction potential

seen by one electron in the field of the bare nuclei. The functions $\Phi^{(-)}(\mathbf{k},\mathbf{r})$ are the H_2^+ continuum eigenfunctions with incoming momentum $\mathbf{k}$. There are other choices of testing functions that are equivalent, although this choice is optimal for eliminating the contributions of the single ionization channel, because of the orthogonality of the H_2^+ continuum eigenfunctions to the bound states of H_2^+. This works in the same way as the $Z = 2$ Coulomb functions in the case of the helium atom (Eq.3.45). As in the case of an atom it is worth to emphasize again that the product of 'testing functions' is not the physical final-state wave function, although it is the exact way of removing the single ionization components from the scattered wave function.

3.4.1 H_2^+ continuum functions

The evaluation of the H_2^+ continuum wave functions, used as 'testing functions', already poses a computational challenge, since the electron leaves behind two protons, positioned at $\pm A$. The one-electron functions $\Phi^{(-)}(\mathbf{k},\mathbf{r})$ are the solutions of:

$$\left[\frac{k^2}{2} + \frac{\nabla^2}{2} + \frac{1}{|\mathbf{r}-\mathbf{A}|} + \frac{1}{|\mathbf{r}+\mathbf{A}|}\right]\Phi^{(-)}(\mathbf{k},\mathbf{r}) = 0 \tag{3.57}$$

and satisfy the usual relationship, $\Phi^{(-)}(\mathbf{k},\mathbf{r}) = [\Phi^{(+)}(-\mathbf{k},\mathbf{r})]^*$. The goal is to define a procedure to evaluate (3.57) to arbitrary accuracy, and producing a nearly exact value of the fixed-nuclei double photoionization amplitude within the Born-Oppenheimer approximation.

As the incoming wave part in the solution of Eq.(3.57) is only determined by the long range behavior of the potential, it is identical to the previously considered problem for the Helium atom with $Z = 2$. Hence, it is possible to convert Eq.(3.57) into a driven equation for the scattered wave part of $\Phi^{(+)}$, where the H_2^+ wavefunction can be rewritten as:

$$\Phi^{(+)}(\mathbf{k},\mathbf{r}) = \chi(\mathbf{k},\mathbf{r}) + \Phi_c^{(+)}(\mathbf{k},\mathbf{r}) \tag{3.58}$$

with the unperturbed portion $\Phi^{(+)}(\mathbf{k},\mathbf{r})$ being the standard $Z = 2$ Coulomb function, $\Phi_c^{(+)}(k,r)$, and incoming momentum vector $\mathbf{k}$. The scattered wave portion $\chi(k,r)$ of the exact H_2^+ continuum function then satisfies the driven Schrödinger equation:

$$\left(\frac{k^2}{2} - h\right)\chi(\mathbf{k},\mathbf{r}) = \left(h - \frac{k^2}{2}\right)\Phi_c^{(+)}(\mathbf{k},\mathbf{r}) = \left(\frac{2}{r} - \frac{1}{|\mathbf{r}-\mathbf{A}|} - \frac{1}{|\mathbf{r}+\mathbf{A}|}\right)\Phi_c^{(+)}(\mathbf{k},\mathbf{r}) \tag{3.59}$$

with h being the one-electron Hamiltonian in Eq.(3.57). As χ is an outgoing wave, the correct boundary conditions can be imposed using the ECS

transformations described earlier.

The solution of Eq.(3.59) is required for any direction of the momentum vector $\mathbf{k}$ in $\Phi_c^{(+)}(\mathbf{k},\mathbf{r})$. In the fixed-body frame, the solution can be written as a single-center expansion of the form:

$$\Phi^{+}(\mathbf{k},\mathbf{r}) = \sum_{l,m,l'} \varphi_{ll'm}(r,k) Y^{*}_{lm}(\hat{\mathbf{k}}) Y_{l'm}(\hat{\mathbf{r}}) \tag{3.60}$$

where the magnetic quantum number m is a constant of the system (good quantum number). To construct the radial functions $\varphi_{ll'm}(r,k)$, the appropriate single-center expansion of the quantities in Eq.(3.58) are required. First, applying the expansion of the momentum normalized Coulomb function:

$$\Phi_c^{(+)}(\mathbf{k},\mathbf{r}) = \left(\frac{2}{\pi}\right)^{1/2} \sum_{l,m} \frac{i^l e^{i\eta_l(k)}}{kr} \phi^{(c)}_{l,k}(r) Y_{l,m}(\hat{\mathbf{r}}) Y^{*}_{lm}(\hat{\mathbf{k}}), \tag{3.61}$$

where $\phi^{(c)}_{l,k}(r)$ is the radial Coulomb function with the asymptotic form

$$\sin[kr + (Z/k)\log 2kr - l\pi/2 + \eta_l(k)] \tag{3.62}$$

and the Coulomb phase:

$$\eta_l(k) = \arg\Gamma(l + q - iZ/k) \tag{3.63}$$

Then a set of solutions of the driven Schrödinger equation with the right-hand sides being proportional to an incident Coulomb function with a single $Y_{l_0,m_0}(r)$ can be defined:

$$(E-h)\chi^{l_0,m_0}(\mathbf{r}) = (h-E)\frac{\varphi^{(c)}_{l_0,k}(r)}{kr} Y_{l_0,m_0}(\hat{\mathbf{r}}) \tag{3.64}$$

The single-center expansion of the function $\chi^{l_0,m_0}(\mathbf{r})$ and choosing the z-axis to coincide with the direction of $\hat{A}$, and using the fact that m being a good quantum number, gives:

$$\chi^{l_0,m_0}(\mathbf{r}) = \sum_{l} \frac{R^{l_0,m_0}_{l}(r)}{r} Y_{lm_0}(\hat{\mathbf{r}}) \tag{3.65}$$

This expansion results in a set of coupled equations for the outgoing radial functions $R^{l_0,m_0}_{l}(r)$ corresponding to an incident Coulomb wave with angular momentum quantum numbers l_0 and m_0, that must be solved for every l_0 and m_0

$$\sum_{l} \left\{ \delta_{l',l} \left[E - \left(-\frac{1}{2}\frac{d^2}{dr^2} + \frac{l(l+1)}{2r^2} \right) \right] - v^{m_0}_{l',l}(r) \right\} R^{l_0 m_0}_{l}(r) = \\ = \left[v^{m_0}_{l',l_0}(r) + \frac{2}{r}\delta_{l',l_0} \right] \frac{1}{k} \phi^{(c)}_{l_0,k}(r), \tag{3.66}$$

where

$$v_{l',l}^{m_0}(r) = \int d\hat{r} Y_{l',m_0}^*(\hat{r}) \left(-\frac{1}{|r-A|} - \frac{1}{|r+A|} \right) Y_{l,m_0}(\hat{r}). \tag{3.67}$$

As parity is conserved, the sum $\sum_l$ is limited to even values of l if l_0 is even and to odd values if l_0 is odd.

The complete solution of Eq.(3.59) can be constructed for any direction of $\mathbf{k}$ as a linear combination of the solutions of Eq.(3.66),

$$\begin{aligned} \chi(\mathbf{k},\mathbf{r}) &= \sum_{l_0,m_0} i^{l_0} e^{i\eta_{l_0}(k)} Y_{l_0,m_0}^*(\hat{\mathbf{k}}) \chi^{l_0,m_0}(\mathbf{r}) = \\ &= \sum_{l_0,m_0} i^{l_0} e^{i\eta_{l_0}(k)} Y_{l_0,m_0}^*(\hat{\mathbf{k}}) \frac{R_l^{l_0,m_0}(r)}{r} Y_{l,m_0}(\hat{\mathbf{r}}) \end{aligned} \tag{3.68}$$

The resulting single-center expansion of the H_2^+ scattering eigenstates in the body-fixed frame is then:

$$\begin{aligned} \Phi^{(+)}(\mathbf{k},\mathbf{r}) &= \left(\frac{2}{\pi}\right) \sum_{l,m} i^l e^{i\eta_l(k)} Y_{lm}^*(\hat{\mathbf{k}}) \\ &\times \sum_{l'} \Delta_{l,l'} \left(\frac{\Phi_{l,k}^{(c)}(r)}{kr} \delta_{l,l'} + \frac{R_{l'}^{lm}}{r} \right) Y_{l',m}(\hat{\mathbf{r}}) \end{aligned} \tag{3.69}$$

and has the same single-center expansion as in Eq.(3.60). The radial functions $R_{l'}^{lm}(r)$ can be expanded in a basis of discrete functions (within this thesis work, in either B-Splines or FEM-DVR). Substituting the representation of the radial functions in Eq.(3.66) the result is a system of linear equations for their coefficients.

3.4.2 Partial-wave double ionization amplitudes

Similar to the atomic case, it is possible to write the scattered two-electron continuum wave function, Ψ_{SC}^+, for a fixed value of the total magnetic projection M along the molecular axis, for singlet spin coupling. It can be written as a sum of products of two-dimensional radial wave functions and spherical harmonics:

$$\begin{aligned} \Psi_{SC}^+(\mathbf{r}_1,\mathbf{r}_2) = \sum_{\mu_1\mu_2, j_1 \geq j_2} \Bigg(& \frac{\psi_{j_1\mu_1,j_2\mu_2}^{dir}(r_1,r_2)}{r_1 r_2} Y_{j_1\mu_1}(\hat{\mathbf{r}}_1) Y_{j_2\mu_2}(\hat{\mathbf{r}}_2) \\ & + \frac{\psi_{j_1\mu_1,j_2\mu_2}^{exch}(r_1,r_2)}{r_1 r_2} Y_{j_2\mu_2}(\hat{\mathbf{r}}_1) Y_{j_1\mu_1}(\hat{\mathbf{r}}_2) \Bigg) \end{aligned} \tag{3.70}$$

The expansion in direct and exchange contributions in Eq.(3.70) can be represented by employing an explicitly symmetrized wave function ψ^{dir} and ψ^{exch}, although it would also be possible to use an unsymmetrized representation with unrestricted sums over j_1 and j_2, except those forbidden by parity. For the one-photon double ionization of H_2, initially in the ${}^1\Sigma_g^+$ ground state, the outgoing wave function can only ungerade symmetries:

$$ {}^1\Sigma_g^+ \rightarrow \begin{cases} {}^1\Sigma_u^+ & for \quad \Delta M = 0 \\ {}^1\Pi_u & for \quad \Delta M \pm 1 \end{cases} \tag{3.71} $$

For example, to obtain the ungerade scattering wave function, Ψ_{SC}^+, j_1 has to be even and j_2 must be odd and viceversa. Similarly, to get the gerade symmetry, j_1 and j_2 must be either even or odd. This reduces significantly the size of the computations. The radial wavefunctions $\psi^{dir}_{j_1\mu_1 j_2\mu_2}(r_1, r_2)$ and $\psi^{exch}_{j_1\mu_1 j_2\mu_2}(r_1, r_2)$ are expanded either in products of B-Splines or FEM-DVR elements, so the Hamiltonian matrix elements corresponding to the left hand side of (3.29) are the same as those in the complete configuration interaction calculation in that basis.

The amplitude for double ionization is expressed as a six-dimensional volume integral Eq.(3.56) and can be transformed into a five-dimensional surface integral on a sphere of hyperradius ρ (using Gauss' theorem):

$$ \begin{aligned} & f(\mathbf{k}_1, \mathbf{k}_2) = \\ & \int\int\int d\Omega_1 d\Omega_2 d\rho \int_0^{\pi/2} d\alpha \frac{\rho^5 \sin^2\alpha \cos^2\alpha}{2} \Phi^{(-)}(\mathbf{k}_1, \mathbf{r}_1)^* \Phi^{(-)}(\mathbf{k}_2, \mathbf{r}_2)^* \\ & \times \left[\frac{\overleftarrow{\partial}}{\partial\rho} \delta(\rho - \rho_0) - \delta(\rho - \rho_0) \frac{\overrightarrow{\partial}}{\partial\rho} \right] \Psi_{SC}^+(\mathbf{r}_1, \mathbf{r}_2). \end{aligned} \tag{3.72} $$

The notation of the partial derivatives with respect to the hyper-radius operate to the left or to the right as indicated by the arrows, and the delta functions constrain the integration to the surface of the hypersphere. In addition to the normal spherical polar angles, denoted as Ω_1 and Ω_2, the hyperspherical coordinates are:

$$ \begin{aligned} \rho &= \sqrt{r_1^2 + r_2^2} \\ \tan(\alpha) &= \frac{r_2}{r_1} \end{aligned} \tag{3.73} $$

This surface integral is written to allow for the direct use of the radial functions from calculations performed in ordinary spherical coordinates, instead of the more familiar hyperradial functions of ρ in this coordinate system.

Now it is possible to substitute the partial-wave expansions of the one-electron functions $\Phi^{(-)}(\mathbf{k}_1, \mathbf{r}_1)$ and $\Phi^{(-)}(\mathbf{k}_2, \mathbf{r}_2)$ (given by $\Phi^{(+)}(-\mathbf{k}, \mathbf{r})^*$) in

Eq.(3.61) and the two-electron wave function of Eq.(3.70) into the surface integral expression for the amplitude in Eq.(3.72). Integrating over $d\Omega_1$ and $d\Omega_2$ yields an expression for the double ionization amplitude for a particular value of ΔM. Because of the orthogonality of the spherical harmonics, the integration over the angles Ω_1 and Ω_2 connects outgoing waves of the two-electron wave function of a particular $Y_{j_1\mu_1}(\hat{r_1})Y_{j_2\mu_2}(\hat{r_2})$ to the corresponding components of the two one-electron functions. The resulting amplitude becomes:

$$f^{(M)}(\mathbf{k}_1,\mathbf{k}_2) = \sum_{l_1,\mu_1}\sum_{l_2,\mu_2}\left(\frac{2}{\pi}\right) i^{-l_1-l_2} e^{i\eta_{l_1}(k_1)+i\eta_{l_2}(k_2)}$$
$$\times\Bigg[Y_{l_1\mu_1}(\hat{\mathbf{k}}_1)Y_{l_2\mu_2}(\hat{\mathbf{k}}_2)\sum_{j_1\geq j_2} F^{dir}_{l_1l_2j_1\mu_1j_2\mu_2}(k_1,k_2)\delta_{j_1l_1}\delta_{j_2l_2} +$$
$$Y_{l_1\mu_2}(\hat{\mathbf{k}}_1)Y_{l_2\mu_2}(\hat{\mathbf{k}}_2)\sum_{j_1\geq j_2} F^{exch}_{l_1l_2j_1\mu_1j_2\mu_2}(k_1,k_2)\delta_{j_2l_1}\delta_{j_1l_2}\Bigg], \qquad (3.74)$$

where $M=\mu_1+\mu_2$, and the factor $\Delta_{j,l}$ is unity if $j+l$ is even and zero otherwise. The direct radial amplitude in this expression is the surface integral for particular angular components,

$$F^{dir}_{l_1,l_2,j_1,\mu_1,j_2,\mu_2}(k_1,k_2) = \frac{\rho_0}{2}\int_0^{\pi/2} d\alpha \left(\frac{\phi^{(c)}_{l_1,k_1}(r_1)}{k_1}\delta_{l_1,j_1} + R^{l_1\mu_1}_{j_1}(r_1)\right)$$
$$\times\left(\frac{\phi^{(c)}_{l_2,k_2}(r_2)}{k_2}\delta_{l_2,j_2} + R^{l_2\mu_2}_{j_2}(r_2)\right)\left[\frac{\overleftarrow{\partial}}{\partial\rho} - \frac{\overrightarrow{\partial}}{\partial\rho}\right]_{\rho=\rho_0} \psi^{dir}_{j_1,\mu_1,j_2,\mu_2}(r_1,r_2) \qquad (3.75)$$

and the corresponding exchange amplitude is obtained by interchanging j_1,μ_1 and j_2,μ_2 on the right hand side:

$$F^{exch}_{l_1,l_2,j_1,\mu_1,j_2,\mu_2}(k_1,k_2) = \frac{\rho_0}{2}\int_0^{\pi/2} d\alpha \left(\frac{\phi^{(c)}_{l_1,k_1}(r_1)}{k_1}\delta_{l_1,j_2} + R^{l_1\mu_2}_{j_2}(r_1)\right)$$
$$\times\left(\frac{\phi^{(c)}_{l_2,k_2}(r_2)}{k_2}\delta_{l_2,j_1} + R^{l_2\mu_1}_{j_1}(r_2)\right)\left[\frac{\overleftarrow{\partial}}{\partial\rho} - \frac{\overrightarrow{\partial}}{\partial\rho}\right]_{\rho=\rho_0} \psi^{exch}_{j_1,\mu_1,j_2,\mu_2}(r_1,r_2). \qquad (3.76)$$

A number of radial one-electron test functions with values l_1 and l_2 for their incident Coulomb waves can have outgoing waves with angular momenta $j_1\mu_2$ and $j_2\mu_2$, so, each two-electron radial function corresponding to a particular angular component $Y_{j_1\mu_1}(\hat{r_1})Y_{j_2\mu_2}(\hat{r_2})$ results in a set of these direct or exchange amplitudes.

The expression in equation (3.74) can be simplified by summing over the angular momenta j_1 and j_2 associated with the single-center expansion of $\Psi_{SC}^{+(M)}$ and thereby define "reduced amplitudes" $\mathcal{F}_{l_1,l_2,\mu_1,\mu_2}^{dir,exch(M)}(k_1,k_2)$:

$$\begin{aligned} f^{(M)}(\mathbf{k}_1,\mathbf{k}_2) = & \sum_{l_1,\mu_1}\sum_{l_2,\mu_2}\left(\frac{2}{\pi}\right) i^{-l_1-l_2} e^{i\eta_{l_1}(k_1)+i\eta_{l_2}(k_2)} \\ \times & \left[\mathcal{F}_{l_1,l_2,\mu_1,\mu_2}^{dir(M)}(k_1,k_2) Y_{l_1\mu_1}(\hat{\mathbf{k}}_1) Y_{l_2\mu_2}(\hat{\mathbf{k}}_2)\right. \\ & \left. + \mathcal{F}_{l_1,l_2,\mu_1,\mu_2}^{exch(M)}(k_1,k_2) Y_{l_1\mu_2}(\hat{k_1}) Y_{l_2\mu_1}(\hat{k_2})\right] \end{aligned} \tag{3.77}$$

With this notation only one of the reduced amplitudes ($\mathcal{F}_{l_1,l_2,\mu_1,\mu_2}^{dir,exch(M)}(k_1,k_2)$) is nonzero in each term of these sums.

With the three expressions for each fixed value of M, it is necessary to obtain an expression to calculate the amplitude for arbitrary orientations of the polarization vector relative to the the molecular axis in the fixed-body frame. The solution for an arbitrary direction $\hat{\epsilon}$, the formal solution of Eq.(3.30) with all three M contributions to the scattered wave:

$$\langle \mathbf{\Phi^{(M)}} | E_0 + \omega - H | \mathbf{\Phi^{(M)}} \rangle \cdot \mathbf{\Psi_{sc}^{+(M)}} = \hat{\epsilon} \cdot \langle \mathbf{\Phi^{(M)}} | (\mathbf{r_1} + \mathbf{r_2}) | \Psi_0 \rangle \tag{3.78}$$

The right hand sides for the above set of equations can be simplified differently. It will be shown for the $< -iy >$ matrix elements to be sufficient to express the amplitude for a given orientation of the polarization axis with respect to the molecular axis. Substituting for the possible values of M in 3.78:

$$\begin{aligned} \langle \Phi^{(0)} | E_0 + \omega - H | \Phi^{(0)} \rangle \cdot \Psi_{sc}^{+(0)} &= \hat{\epsilon}_z \cdot \langle \Phi^{(M)} | z_1 + z_2 | \Psi_0 \rangle \\ \langle \Phi^{(+1)} | E_0 + \omega - H | \Phi^{(+1)} \rangle \cdot \Psi_{sc}^{+(+1)} &= \hat{\epsilon}_x \cdot \langle \Phi^{+1)} | x_1 + x_2 | \Psi_0 \rangle \\ &+ i\hat{\epsilon}_y \cdot \langle \Phi^{(+1)} | - iy_1 - iy_2 | \Psi_0 \rangle \\ \langle \Phi^{(-1)} | E_0 + \omega - H | \Phi^{(-1)} \rangle \cdot \Psi^{+(-1)_{sc}} &= \hat{\epsilon}_x \cdot \langle \Phi^{(-1)} | x_1 + x_2 | \Psi_0 \rangle \\ &+ i\hat{\epsilon}_y \cdot \langle \Phi^{(-1)} | - iy_1 - iy_2 | \Psi_0 \rangle \end{aligned} \tag{3.79}$$

The following identities for matrix elements involving spherical harmonics with $m = -1, 0, +1$ and configurations with $M = -1, 0, +1$ will be useful:

$$\begin{aligned} \langle Y_{l',-1} | x | Y_{l,0} \rangle &= -a \\ \langle Y_{l',+1} | x | Y_{l,0} \rangle &= a \\ \langle Y_{l',-1} | - iy | Y_{l,0} \rangle &= a \\ \langle Y_{l',+1} | - iy | Y_{l,0} \rangle &= a, \end{aligned} \tag{3.80}$$

where a is a real number. All of these integrals are *real valued* and related, thus it is possible to use one only matrix elements such as $< -iy >$ to evaluate equation 3.78. The case of z polarization is the Σ_u case, and the amplitudes associated with $\Psi_{sc}^{+(0)}$ can be calculated directly.

Then the right hand sides of the second two equalities in Eq.(3.79) can be written in a simpler form in terms of just the matrix elements of the $(-iy)$ operator:

$$\begin{aligned}\langle\Phi^{(+1)}|E_0+\omega-H|\Phi^{(+1)}\rangle\cdot\Psi_{sc}^{+(+1)} &= (\hat{\epsilon}_x+i\hat{\epsilon}_y) \quad\cdot\quad \langle\Phi^{(+1)}|-iy_1-iy_2|\Psi_0\rangle \\ \langle\Phi^{(-1)}|E_0+\omega-H|\Phi^{(-1)}\rangle\cdot\Psi_{sc}^{+(-1)} &= (-\hat{\epsilon}_x+i\hat{\epsilon}_y) \quad\cdot\quad \langle\Phi^{(-1)}|-iy_1-iy_2|\Psi_0\rangle\end{aligned} \tag{3.81}$$

The relationship between the $M=\pm1$ elements can be seen from the "$-iy$" polarization of the contribution:

$$\begin{aligned}\langle\Phi^{(+1)}|E_0+\omega-H|\Phi^{(+1)}\rangle\cdot\Psi_{sc}^{+(+1,-iy)} &= \langle\Phi^{(+1)}|-iy_1-iy_2|\Psi_0\rangle \\ \langle\Phi^{(-1)}|E_0+\omega-H|\Phi^{(-1)}\rangle\cdot\Psi_{sc}^{+(-1,-iy)} &= \langle\Phi^{(-1)}|-iy_1-iy_2|\Psi_0\rangle\end{aligned}$$

Then the solutions of (3.79) or (3.81) can be written in terms of the solution of (3.82):

$$\begin{aligned}\Psi_{SC}^{+(+1)} &= (\hat{\epsilon}_x+i\hat{\epsilon}_y)\Psi_{SC}^{+(+1,-iy)} \\ \Psi_{SC}^{+(-1)} &= (-\hat{\epsilon}_x+i\hat{\epsilon}_y)\Psi_{SC}^{+(-1,-iy)}\end{aligned} \tag{3.82}$$

The final working expression for the amplitude for a given direction of the polarization vector $\hat{\epsilon}=(\hat{\epsilon}_x,\hat{\epsilon}_y,\hat{\epsilon}_z)$ is then:

$$\begin{aligned}f(\mathbf{k_1},\mathbf{k_2}) = \quad & \hat{\epsilon}_z f^{(0)}(\mathbf{k_1},\mathbf{k_2}) + \\ & \frac{(\hat{\epsilon}_x+i\hat{\epsilon}_y)}{\sqrt{2}} f^{(+1,[-iy])}(\mathbf{k_1},\mathbf{k_2}) + \\ & \frac{(-\hat{\epsilon}_x+i\hat{\epsilon}_y)}{\sqrt{2}} f^{(-1,[-iy])}(\mathbf{k_1},\mathbf{k_2})\end{aligned} \tag{3.83}$$

where the $f^{(M,\mathbf{r})}(\mathbf{k_1},\mathbf{k_2})$ are the amplitudes calculated for a given value of M, and $\mathbf{r}$ indicates the matrix element used.

3.5 Amplitudes for two photon double photoionization of a molecule: H_2

The two-photon ionization process exhibits of the same divergence related to the above threshold ionization (ATI) as for the two-photon double-ionization

of He. Therefore same approach of using imaginary values for ω is be used in order to obtain converged amplitudes (see section 3.3).

In addition the molecular axis can now be oriented randomly with respect to the polarization vector.

Therefore a similar expression to Eq.(3.83) is needed, but for a two-photon calculation. Unfortunately, for the second photon, the driven term is not an eigenfunction of L_z, except for the case of $M = 0$. Instead of using $\Psi_{SC}^{+(\pm1,0)}$ as initial state, $\Psi_{SC}^{+(\pm1,-iy)}$ for $\Delta M = \pm1$ and $\Psi_{SC}^{+(0,z)}$ for $\Delta M = 0$ are used.

3.5.1 Two $\Delta M = 0$ transitions

Consider the case of $\Sigma_g \rightarrow \Sigma_u \rightarrow \Sigma_g$ transitions, the equation describing absorption of the second photon is given by:

$$\langle\Phi^{(0)}|E_0 + 2\omega - H|\Phi^{(0)}\rangle \cdot \Psi_{sc}^{+(0)} = \hat{\epsilon}_z \cdot \langle\Phi^{(0)}|z_1 + z_2|\Psi_{SC}^{+(0)}\rangle \tag{3.84}$$

Since for both photons the driven terms with $M = 0$ are eigenfunctions of L_z, the relationship between the calculated wave function and the physical scattering wave function is trivial:

$$\Psi_{SC}^{+(0)} = \hat{\epsilon}_z^2 \Psi_{SC}^{+(0,z)}. \tag{3.85}$$

3.5.2 A $\Delta M = +1$ transition followed by a $\Delta M = \pm1$

After absorption of the first photon $\Psi_{SC}^{+(+1)}$ needs to be calculated. For the second photon, the equivalent expressions to those in Eq.(3.78) and Eq.(3.79) are:

$$\langle\Phi^{(M)}|E_0 + 2\omega - H|\Phi^{(M)}\rangle \cdot \Psi_{sc}^{+(\mathbf{M})} = \hat{\epsilon} \cdot \langle\Phi^{(M)}|(\mathbf{r_1} + \mathbf{r_2})|\Psi_{SC}^{+(+1)}\rangle,$$

and

$$\begin{aligned}
\langle\Phi^{(+2)}|E_0 + 2\omega - H|\Phi^{(+2)}\rangle \cdot \Psi_{sc}^{+(+2)} &= \hat{\epsilon}_x \cdot \langle\Phi^{(+2)}|x_1 + x_2|\Psi_{SC}^{+(+1)}\rangle \\
&+ i\hat{\epsilon}_y \cdot \langle\Phi^{(+2)}| - iy_1 - iy_2|\Psi_{SC}^{+(+1)}\rangle \\
\langle\Phi^{(0)}|E_0 + 2\omega - H|\Phi^{(0)}\rangle \cdot \Psi_{sc}^{+(0)} &= \hat{\epsilon}_x \cdot \langle\Phi^{(0)}|x_1 + x_2|\Psi_{SC}^{+(+1)}\rangle \\
&+ i\hat{\epsilon}_y \cdot \langle\Phi^{(0)}| - iy_1 - iy_2|\Psi_{SC}^{+(+1)}\rangle
\end{aligned} \tag{3.86}$$

As for the one-photon case, the relationship between the matrix elements of spherical harmonics and the x and $-iy$ operators are needed in order to find the relationship for the amplitudes.

$$\begin{aligned}
&\langle Y_{l',+2}|x|Y_{l,+1}\rangle = -a \\
&\langle Y_{l',0}|x|Y_{l,+1}\rangle = \frac{1}{\sqrt{6}}a \\
&\langle Y_{l',+2}|-iy|Y_{l,+1}\rangle = -a \\
&\langle Y_{l',0}|-iy|Y_{l,+1}\rangle = -\frac{1}{\sqrt{6}}a,
\end{aligned} \tag{3.87}$$

where a is a real number. Consequently the wave functions can be calculated in the same way as for the one photon ionization of H_2. After extracting the amplitude, for example, for the $< -iy >$ element, Eq.(3.86) can be rewritten in terms of the $< -iy >$ operator for any orientation of the polarization vector with respect to the molecular axis:

$$\begin{aligned}
&\langle\Phi^{(+2)}|E_0+2\omega-H|\Phi^{(+2)}\rangle\cdot\Psi_{sc}^{+(+2)} = \\
&(-\hat{\epsilon}_x - i\hat{\epsilon}_y)\cdot\langle\Phi^{(+2)}|-iy_1-iy_2|\Psi_{SC}^{+(+1)}\rangle \\
&\langle\Phi^{(0)}|E_0+2\omega-H|\Phi^{(0)}\rangle\cdot\Psi_{sc}^{(0)} = \\
&(\hat{\epsilon}_x - i\hat{\epsilon}_y)\cdot\langle\Phi^{(0)}|-iy_1-iy_2|\Psi_{SC}^{+(+1)}\rangle
\end{aligned} \tag{3.88}$$

But the equations with the $< -iy >$ matrix elements are:

$$\begin{aligned}
&\langle\Phi^{(+2)}|E_0+2\omega-H|\Phi^{(+2)}\rangle\cdot\Psi_{sc}^{+(+2,-iy)} = \langle\Phi^{(+2)}|-iy_1-iy_2|\Psi_{sc}^{+(+1,-iy)}\rangle \\
&\langle\Phi^{(0)}|E_0+2\omega-H|\Phi^{(0)}\rangle\cdot\Psi_{sc}^{(0,-iy)} = \langle\Phi^{(0)}|-iy_1-iy_2|\Psi_{sc}^{+(+1,-iy)}\rangle
\end{aligned} \tag{3.89}$$

Here it is not possible to find a relationship between the solutions for different polarizations similar as in Eq.(3.82), because, because the initial state Ψ_0 on the right hand side differs between the set of equations. However, using the definition of $\Psi_{SC}^{+(+1)}$ in Eq.(3.82), and substituting into Eq.(3.88):

$$\begin{aligned}
&\langle\Phi^{(+2)}|E_0+2\omega-H|\Phi^{(+2)}\rangle\cdot\Psi_{sc}^{+(+2)} = \\
&\frac{(-\hat{\epsilon}_x - i\hat{\epsilon}_y)}{\sqrt{2}}\cdot\langle\Phi^{(+2)}|-iy_1-iy_2|\frac{(\hat{\epsilon}_x + i\hat{\epsilon}_y)}{\sqrt{2}}\Psi_{SC}^{+(+1,-iy)}\rangle \\
&\langle\Phi^{(0)}|E_0+2\omega-H|\Phi^{(0)}\rangle\cdot\Psi_{sc}^{(0)} = \\
&\frac{(\hat{\epsilon}_x - i\hat{\epsilon}_y)}{\sqrt{2}}\cdot\langle\Phi^{(0)}|-iy_1-iy_2|\frac{(\hat{\epsilon}_x + i\hat{\epsilon}_y)}{\sqrt{2}}\Psi_{SC}^{+(+1,-iy)}\rangle
\end{aligned} \tag{3.90}$$

and then:

$$\begin{aligned}
&\langle\Phi^{(+2)}|E_0+2\omega-H|\Phi^{(+2)}\rangle\cdot\Psi_{sc}^{+(+2)}=\\
&\frac{(-\hat{\epsilon}_x^2-2i\hat{\epsilon}_x\hat{\epsilon}_y+\hat{\epsilon}_y^2)}{\sqrt{4}}\cdot\langle\Phi^{(+2)}|-iy_1-iy_2|\Psi_{SC}^{+(+1,-iy)}\rangle\\
&\langle\Phi^{(0)}|E_0+2\omega-H|\Phi^{(0)}\rangle\cdot\Psi_{sc}^{(0)}=\\
&\frac{(\hat{\epsilon}_x^2+\hat{\epsilon}_y^2)}{\sqrt{4}}\cdot\langle\Phi^{(0)}|-iy_1-iy_2|\Psi_{SC}^{+(+1,-iy)}\rangle
\end{aligned}\tag{3.91}$$

Hence, the solutions with the correct ΔM can be related to the calculated solutions of Eq.(3.91) with the simple formulas:

$$\begin{aligned}
\Psi_{SC}^{+(+2)}&=\frac{(-\hat{\epsilon}_x^2-2i\hat{\epsilon}_x\hat{\epsilon}_y+\hat{\epsilon}_y^2)}{\sqrt{4}}\Psi_{SC}^{+(+2,-iy)}\\
\Psi_{SC}^{+(0)}&=\frac{(\hat{\epsilon}_x^2+\hat{\epsilon}_y^2)}{\sqrt{4}}\Psi_{SC}^{+(0,-iy)}
\end{aligned}\tag{3.92}$$

3.5.3 A $\Delta M=-1$ transition followed by a $\Delta M=\pm1$

Considering the case where $\Psi_{SC}^{+(-1)}$ is the initial state for absorption of the second photon, the equivalent integrals of Eq.(3.87) for $\Delta M=-1$ are:

$$\begin{aligned}
&\langle Y_{l',-2}|x|Y_{l,-1}\rangle=a\\
&\langle Y_{l',0}|x|Y_{l,-1}\rangle=-\frac{1}{\sqrt{6}}a\\
&\langle Y_{l',-2}|-iy|Y_{l,-1}\rangle=-a\\
&\langle Y_{l',0}|-iy|Y_{l,-1}\rangle=-\frac{1}{\sqrt{6}}a
\end{aligned}\tag{3.93}$$

As these integrals reveal a similar relationship between the terms with x and $-iy$, as before, substituting the definition of $\Psi_{SC}^{+(-1)}$ similar to Eq.(3.82), in Eq.(3.88) gives:

$$\begin{aligned}
&\langle\Phi^{(-2)}|E_0+2\omega-H|\Phi^{(-2)}\rangle\cdot\Psi_{sc}^{+(-2)}=\\
&\frac{(\hat{\epsilon}_x-i\hat{\epsilon}_y)}{\sqrt{2}}\cdot\langle\Phi^{(-2)}|-iy_1-iy_2|\frac{(-\hat{\epsilon}_x+i\hat{\epsilon}_y)}{\sqrt{2}}\Psi_{SC}^{+(-1,-iy)}\rangle\\
&\langle\Phi^{(0)}|E_0+2\omega-H|\Phi^{(0)}\rangle\cdot\Psi_{sc}^{(0)}=\\
&\frac{(-\hat{\epsilon}_x-i\hat{\epsilon}_y)}{\sqrt{2}}\cdot\langle\Phi^{(0)}|-iy_1-iy_2|\frac{(-\hat{\epsilon}_x+i\hat{\epsilon}_y)}{\sqrt{2}}\Psi_{SC}^{+(-1,-iy)}\rangle
\end{aligned}\tag{3.94}$$

and then:

$$\begin{aligned}
&\langle\Phi^{(-2)}|E_0+2\omega-H|\Phi^{(-2)}\rangle\cdot\Psi_{sc}^{+(-2)}= \\
&\frac{(-\hat{\epsilon}_x^2+2i\hat{\epsilon}_x\hat{\epsilon}_y+\hat{\epsilon}_y^2)}{\sqrt{4}}\cdot\langle\Phi^{(-2)}|-iy_1-iy_2|\Psi_{SC}^{+(-1,-iy)}\rangle \\
&\langle\Phi^{(0)}|E_0+2\omega-H|\Phi^{(0)}\rangle\cdot\Psi_{sc}^{(0)}= \\
&\frac{(\hat{\epsilon}_x^2+\hat{\epsilon}_y^2)}{\sqrt{4}}\cdot\langle\Phi^{(0)}|-iy_1-iy_2|\Psi_{SC}^{+(-1,-iy)}\rangle
\end{aligned} \tag{3.95}$$

The corresponding relationship between the scattered wave function and the calculated $\Psi_{SC}^{+(-2|0,[-iy])}$ becomes:

$$\begin{aligned}
\Psi_{SC}^{+(-2)}&=\frac{(-\hat{\epsilon}_x^2+2i\hat{\epsilon}_x\hat{\epsilon}_y+\hat{\epsilon}_y^2)}{\sqrt{4}}\Psi_{SC}^{+(-2,-iy)} \\
\Psi_{SC}^{+(0)}&=\frac{(\hat{\epsilon}_x^2+\hat{\epsilon}_y^2)}{\sqrt{4}}\Psi_{SC}^{+(0,-iy)}
\end{aligned} \tag{3.96}$$

3.5.4 $\Delta M = 0$ (1st photon) and $\Delta M = \pm 1$ (2nd photon)

The intermediate state after the first photon absorption is $\Psi_{sc}^{+(0)}$. The equivalent expressions of Eq.(3.78) and Eq.(3.79) are:

$$\langle\Phi^{(\pm1)}|E_0+2\omega-H|\Phi^{(\pm1)}\rangle\cdot\Psi_{sc}^{+(\pm1)}=\hat{\epsilon}\cdot\langle\Phi^{(M)}|(\mathbf{r_1}+\mathbf{r_2})|\Psi_{SC}^{+(0)}\rangle \tag{3.97}$$

and:

$$\begin{aligned}
\langle\Phi^{(\pm1)}|E_0+2\omega-H|\Phi^{(\pm1)}\rangle\cdot\Psi_{sc}^{+(\pm1)} &= \hat{\epsilon}_x\cdot\langle\Phi^{(\pm1)}|x_1+x_2|\Psi_{SC}^{+(0)}\rangle \\
&+ i\hat{\epsilon}_y\cdot\langle\Phi^{(\pm1)}|-iy_1-iy_2|\Psi_{SC}^{+(0)}\rangle.
\end{aligned} \tag{3.98}$$

The integral equivalence in this case is:

$$\begin{aligned}
&\langle Y_{l',+1}|x|Y_{l,0}\rangle=a \\
&\langle Y_{l',-1}|x|Y_{l,0}\rangle=-a \\
&\langle Y_{l',+1}|-iy|Y_{l,0}\rangle=a \\
&\langle Y_{l',-1}|-iy|Y_{l,0}\rangle=a.
\end{aligned} \tag{3.99}$$

Therefore the relation to the solution for the $< -iy >$ matrix elements becomes: So relating everything to $-iy$ as before:

$$\begin{aligned}
&\langle\Phi^{(+1)}|E_0+2\omega-H|\Phi^{(+1)}\rangle\cdot\Psi_{sc}^{+(+1)}=\\
&\frac{(\hat{\epsilon}_x+i\hat{\epsilon}_y)}{\sqrt{2}}\cdot\langle\Phi^{(+1)}|-iy_1-iy_2|\Psi_{SC}^{+(0)}\rangle\\
&\langle\Phi^{(-1)}|E_0+2\omega-H|\Phi^{(-1)}\rangle\cdot\Psi_{sc}^{+(-1)}=\\
&\frac{(-\hat{\epsilon}_x+i\hat{\epsilon}_y)}{\sqrt{2}}\cdot\langle\Phi^{(-1)}|-iy_1-iy_2|\Psi_{SC}^{+(0)}\rangle
\end{aligned} \tag{3.100}$$

The equivalent equation to (3.92) and (3.96) for the scattered wave function $\Psi_{SC}^{(\pm1)}$ is then given by:

$$\begin{aligned}
\Psi_{SC}^{+(+1)}&=\frac{\hat{\epsilon}_z(\hat{\epsilon}_x+i\hat{\epsilon}_y)}{\sqrt{2}}\Psi_{SC}^{+(+1,-iy)}\\
\Psi_{SC}^{+(-1)}&=\frac{\hat{\epsilon}_z(-\hat{\epsilon}_x+i\hat{\epsilon}_y)}{\sqrt{2}}\Psi_{SC}^{+(-1,-iy)}
\end{aligned} \tag{3.101}$$

3.5.5 $\Delta M = \pm 1$ (1st photon) and $\Delta M = 0$ (2nd photon)

Here the initial state is the $\Pi_u^{\pm}$ state going to the corresponding $\Pi_g^{\pm}$ final state. The second photon transition only involves $\hat{\epsilon}_z$, so:

$$\begin{aligned}
\langle\Phi^{(+1)}|E_0+2\omega-H|\Phi^{(+1)}\rangle\cdot\Psi_{sc}^{+(\mathbf{+1})}&=\hat{\epsilon}_z\cdot\langle\Phi^{(+1)}|(\mathbf{r_1}+\mathbf{r_2})|\Psi_{SC}^{+(1)}\rangle\\
\langle\Phi^{(-1)}|E_0+2\omega-H|\Phi^{(-1)}\rangle\cdot\Psi_{sc}^{+(\mathbf{-1})}&=\hat{\epsilon}_z\cdot\langle\Phi^{(-1)}|(\mathbf{r_1}+\mathbf{r_2})|\Psi_{SC}^{-(1)}\rangle
\end{aligned} \tag{3.102}$$

Following the same steps as for the single ionization in section 3.2, the equivalence of Eq. (3.82) becomes:

$$\begin{aligned}
\Psi_{SC}^{+(+1)}&=\frac{\hat{\epsilon}_z(\hat{\epsilon}_x+i\hat{\epsilon}_y)}{\sqrt{2}}\Psi_{SC}^{+(+1,-iy)}\\
\Psi_{SC}^{+(-1)}&=\frac{\hat{\epsilon}_z(-\hat{\epsilon}_x+i\hat{\epsilon}_y)}{\sqrt{2}}\Psi_{SC}^{+(-1,-iy)}
\end{aligned} \tag{3.103}$$

3.5.6 Wave function equivalences

The equivalence relationships for the scattered wave functions $\Psi^{+(\Delta M)}$ and the calculated functions involving the $< -iy >$ operator are:

$$
\begin{aligned}
\Sigma_g \to \Sigma_u \to \Sigma_g &: \Psi_{SC}^{+(0)} = \hat{\epsilon}_z^2 \Psi_{SC}^{+(0,z)} \\
\Sigma_g \to \Pi_u^+ \to \Delta_g^+ &: \Psi_{SC}^{+(+2)} = \frac{(-\hat{\epsilon}_x^2 - 2i\hat{\epsilon}_x\hat{\epsilon}_y + \hat{\epsilon}_y^2)}{\sqrt{4}} \Psi_{SC}^{+(+2,-iy)} \\
\Sigma_g \to \Pi_u^- \to \Delta_g^- &: \Psi_{SC}^{+(-2)} = \frac{(-\hat{\epsilon}_x^2 + 2i\hat{\epsilon}_x\hat{\epsilon}_y + \hat{\epsilon}_y^2)}{\sqrt{4}} \Psi_{SC}^{+(-2,-iy)} \\
\Sigma_g \to \Pi_u^+ \to \Sigma_g &: \Psi_{SC}^{+(0)} = \frac{(\hat{\epsilon}_x^2 + \hat{\epsilon}_y^2)}{\sqrt{4}} \Psi_{SC}^{+(0,-iy)} \\
\Sigma_g \to \Pi_u^- \to \Sigma_g &: \Psi_{SC}^{+(0)} = \frac{(\hat{\epsilon}_x^2 + \hat{\epsilon}_y^2)}{\sqrt{4}} \Psi_{SC}^{+(0,-iy)} \\
\Sigma_g \to \Sigma_u \to \Pi_g^+ &: \Psi_{SC}^{+(+1)} = \frac{\hat{\epsilon}_z(\hat{\epsilon}_x + i\hat{\epsilon}_y)}{\sqrt{2}} \Psi_{SC}^{+(+1,-iy)} \\
\Sigma_g \to \Sigma_u \to \Pi_g^- &: \Psi_{SC}^{+(-1)} = \frac{\hat{\epsilon}_z(-\hat{\epsilon}_x + i\hat{\epsilon}_y)}{\sqrt{2}} \Psi_{SC}^{+(-1,-iy)} \\
\Sigma_g \to \Pi_u^+ \to \Pi_g^+ &: \Psi_{SC}^{+(+1)} = \frac{\hat{\epsilon}_z(\hat{\epsilon}_x + i\hat{\epsilon}_y)}{\sqrt{2}} \Psi_{SC}^{+(+1,-iy)} \\
\Sigma_g \to \Pi_u^- \to \Pi_g^- &: \Psi_{SC}^{+(-1)} = \frac{\hat{\epsilon}_z(-\hat{\epsilon}_x + i\hat{\epsilon}_y)}{\sqrt{2}} \Psi_{SC}^{+(-1,-iy)}
\end{aligned}
\tag{3.104}
$$

3.5.7 Final amplitude expression

As the final solution for the scattering amplitude involving all the possible two-photon transitions and for an arbitrary polarization vector, $\hat{\epsilon} = (\hat{\epsilon}_x, \hat{\epsilon}_y, \hat{\epsilon}_z)$, with respect to the internuclear axis we obtain:

$$\begin{aligned} f(\mathbf{k_1}, \mathbf{k_2}) = \quad & \hat{\epsilon}_z^2 f^{(0)}_{\Sigma_g \to \Sigma_u \to \Sigma_g}(\mathbf{k_1}, \mathbf{k_2}) + \\ & \frac{(-\hat{\epsilon}_x^2 - 2i\hat{\epsilon}_x\hat{\epsilon}_y + \hat{\epsilon}_y^2)}{\sqrt{4}} f^{(+2,[-iy])}_{\Sigma_g \to \Pi_u^+ \to \Delta_g^+}(\mathbf{k_1}, \mathbf{k_2}) + \\ & \frac{(-\hat{\epsilon}_x^2 + 2i\hat{\epsilon}_x\hat{\epsilon}_y + \hat{\epsilon}_y^2)}{\sqrt{4}} f^{(-2,[-iy])}_{\Sigma_g \to \Pi_u^- \to \Delta_g^-}(\mathbf{k_1}, \mathbf{k_2}) + \\ & \frac{(\hat{\epsilon}_x^2 + \hat{\epsilon}_y^2)}{\sqrt{4}} f^{(0,[-iy])}_{\Sigma_g \to \Pi_u^+ \to \Sigma_g}(\mathbf{k_1}, \mathbf{k_2}) + \\ & \frac{(\hat{\epsilon}_x^2 + \hat{\epsilon}_y^2)}{\sqrt{4}} f^{(0,[-iy])}_{\Sigma_g \to \Pi_u^- \to \Sigma_g}(\mathbf{k_1}, \mathbf{k_2}) + \\ & \frac{\hat{\epsilon}_z(\hat{\epsilon}_x + i\hat{\epsilon}_y)}{\sqrt{2}} f^{(+1,[-iy])}_{\Sigma_g \to \Sigma_u \to \Pi_g^+}(\mathbf{k_1}, \mathbf{k_2}) + \\ & \frac{\hat{\epsilon}_z(-\hat{\epsilon}_x + i\hat{\epsilon}_y)}{\sqrt{2}} f^{(-1,[-iy])}_{\Sigma_g \to \Sigma_u \to \Pi_g^-}(\mathbf{k_1}, \mathbf{k_2}) + \\ & \frac{\hat{\epsilon}_z(\hat{\epsilon}_x + i\hat{\epsilon}_y)}{\sqrt{2}} f^{(+1,[-iy])}_{\Sigma_g \to \Pi_u^+ \to \Pi_g^+}(\mathbf{k_1}, \mathbf{k_2}) + \\ & \frac{\hat{\epsilon}_z(-\hat{\epsilon}_x + i\hat{\epsilon}_y)}{\sqrt{2}} f^{(-1,[-iy])}_{\Sigma_g \to \Pi_u^- \to \Pi_g^-}(\mathbf{k_1}, \mathbf{k_2}) \end{aligned} \tag{3.105}$$

3.5.8 Amplitude test case: Parallel polarization

For parallel polarization ($\epsilon_x = 0, \epsilon_y = 0, \epsilon_z = 1$), the polarization vector only has a z component, and all the components of the two photon amplitude which do not have pure ϵ_z contribution are zero. Thus the amplitude can be written as:

$$f(\mathbf{k_1}, \mathbf{k_2}) = \quad f^{(0)}_{\Sigma_g \to \Sigma_u \to \Sigma_g}(\mathbf{k_1}, \mathbf{k_2}). \tag{3.106}$$

3.5.9 Amplitude test case: Perpendicular polarization I

For perpendicular polarization in $\hat{x}$-direction ($\epsilon_x = 1, \epsilon_y = 0, \epsilon_z = 0$), the only contributing terms in (3.105) are:

$$\begin{aligned} f(\mathbf{k_1}, \mathbf{k_2}) = & \\ & -\frac{1}{2} f^{(+2,[-iy])}_{\Sigma_g \to \Pi_u^+ \to \Delta_g^+}(\mathbf{k_1}, \mathbf{k_2}) \\ & -\frac{1}{2} f^{(-2,[-iy])}_{\Sigma_g \to \Pi_u^- \to \Delta_g^-}(\mathbf{k_1}, \mathbf{k_2}) \\ & +\frac{1}{2} f^{(0,[-iy])}_{\Sigma_g \to \Pi_u^+ \to \Sigma_g}(\mathbf{k_1}, \mathbf{k_2}) \\ & +\frac{1}{2} f^{(0,[-iy])}_{\Sigma_g \to \Pi_u^- \to \Sigma_g}(\mathbf{k_1}, \mathbf{k_2}) \end{aligned} \tag{3.107}$$

3.5.10 Amplitude test case: Perpendicular polarization II

Similarly, for perpendicular polarization in $\hat{y}$-direction ($\epsilon_x = 0, \epsilon_y = 1, \epsilon_z = 0$), the scattering amplitudes becomes:

$$\begin{aligned} f(\mathbf{k_1}, \mathbf{k_2}) = & \\ & +\frac{1}{2} f^{(+2,[-iy])}_{\Sigma_g \to \Pi_u^+ \to \Delta_g^+}(\mathbf{k_1}, \mathbf{k_2}) \\ & +\frac{1}{2} f^{(-2,[-iy])}_{\Sigma_g \to \Pi_u^- \to \Delta_g^-}(\mathbf{k_1}, \mathbf{k_2}) \\ & +\frac{1}{2} f^{(0,[-iy])}_{\Sigma_g \to \Pi_u^+ \to \Sigma_g}(\mathbf{k_1}, \mathbf{k_2}) \\ & +\frac{1}{2} f^{(0,[-iy])}_{\Sigma_g \to \Pi_u^- \to \Sigma_g}(\mathbf{k_1}, \mathbf{k_2}) \end{aligned} \tag{3.108}$$

CHAPTER 4

Numerical representations of the wave functions

In a numerical calculation, the implementation of *sharp exterior scaling* requires of a grid based representation of both the wave functions and the Hamiltonian operator. Different representations have been used together with ECS for doing scattering and breakup calculations. Examples are finite differences [91], traditional finite elements [92, 93], pseudospectral methods [94, 95], **B-Splines** [96], and **finite-element methods with discrete variable representation (FEM-DVR)** [97, 86, 63].

B-Splines and FEM-DVR are the one chosen to do the presented calculations, and so, they will be described here.

4.1 B-Splines

In the field of numerical analysis, a spline function is a function defined piecewise by the use of polynomials. This kind of functions is mainly used in interpolating problems, as it yields similar results to polynomial results, while avoiding the called Runge phenomenon for higher degrees. It is also a really used tool in the field of computer-aided design and computer graphics, as the construction of this functions is really simple, they can be used to fit any kind of curve shape accurately.

B-splines are splines functions that have minimal support (set of points where the function is not zero) with respect to a given degree, smoothness and domain partition. Any given spline function of a certain degree, smoothness and domain partition can be represented as a linear combination of B-splines of the same degree and smoothness over that partition.

Although the development of B-Splines has been quite recent, its use in the frame of atomic and molecular physics has become more and more popular in the last decades. The first appearance of the term B-Splines was in 1946, in a paper by Isaac Jacob Schoenberg in 1946 [98]. But it was

almost thirty years later when B-Splines were first used for atomic physics in a series of papers by Shore ([99]) where he studied the discrete spectrum of the hydrogen atom and other model systems, showing that B-Splines based methods were as accurate as other methods such as standard finite-difference or Numerov methods. But the real push forward in physics is due to the publication in 1978 of *A Practical Guide to Splines* by Carl de Boor ([100]). This book described in detail the most important mathematical properties of splines, B-Splines basis set, and included a handful of Fortran-77 codes showing the use of such functions. But, another decade had to pass in order to find the first application of B-Splines beyond the hydrogen-atom case ([101, 102]).

This functions have many properties that make them more suitable for the description of continuum states. One of that advantages is the quasi-banded structure of the matrices that one has to diagonalize in single particle problems. This allows the use of bigger basis sets without problems related to linear dependence.

This section is organized as follows. We will first present the basic mathematical definition and properties of B-Spline basis sets. Then, some examples and simple applications will be shown.

4.1.1 Definition and properties of B-Spline functions

Before the description of the building process, some definitions are required to understand this procedure:

- k order polynomials (maximum order $k-1$) are defined as:

$$p(x) = a_0 + a_1 x + a_2 x^2 + ... + a_{k-1} x^{k-1} \tag{4.1}$$

- If a function is continuous, and its derivatives are continuous up to a order n, in a given domain, that function is said to be of C^n class in that domain. So, for example, if a function belongs to the C^2 class, it means that it is twice-differentiable and its second derivative is continuous.

- Considering an interval $I = [a, b]$ divided in l sub-intervals $I_j = [\xi_j, \xi_j + 1]$ by an ascending order sequence of $l+1$ points ξ_j in such a way that:

$$a = \xi_1 < \xi_2 < .. < \xi_{l+1} = b \tag{4.2}$$

  The ξ_j points are called **breakpoints**.

- A second positive integer number sequence is associated with this *breakpoints*, called v_j with $j = 2, ..., l, v_j \geq 0$, that defines the continuity condition $C^{v_j - 1}$ in the associated *breakpoint* ξ_j. To the *breakpoints* in the first and the last point a 0 continuity is associated, it means $v_1 = v_{l+1} = 0$

- There is a last sequence of points, called *knots* (t_i) in non-strict ascending order:

$$\{t_i\}_{(i=1,..,m)}, t_1 \leq t_2 \leq ... \leq t_m \tag{4.3}$$

  These knots (t_i) are associated to each *breakpoint* (ξ_j) in the following way:

$$\begin{aligned}
&t_1 = t_2 = ... = t_{\mu_1} = \xi_1; \quad \mu_1 = k \\
&t_{\mu_1+1} = t_{\mu_1+2} = ... = t_{\mu_1+\mu_2} = \xi_2; \quad \mu_1 = k \\
&... \\
&t_{p+1} = t_{p+2} = ... = t_{p+\mu_1} = \xi_i; \quad p = \mu_1 + \mu_2 + ... + \mu_{i-1} \\
&... \\
&t_{n+1} = t_{n+2} = ... = t_{n+k} = \xi_{l+1}; \;\; mu_{l+1} = k; \;\; n = \mu_1 + ... + \mu_l
\end{aligned} \tag{4.4}$$

  where μ_j is the multiplicity of the *knots* t_i in ξ_j, which is $\mu_j = k - v_j$. Multiplicity in the first and the last point of the interval should be fixed to the maximum $(k = \mu_i = \mu_{l+1})$. The most common value for the inner points is to choose unitary multiplicity, that achieves the maximum continuity (C^{k-2}).

- With this definitions the number of B-Splines involved in the basis set is:

$$n = l + k - 1 \tag{4.5}$$

- The continuity in a *breakpoint* can be reduced by increasing its associated multiplicity

Given this definitions, a B-Spline $B(x)$ is determined by the order $k > 0$, and a set of $k + 1$ *knots* $(t_i, ..., t_{i+k})$ in a way that $t_i < t_{i+k}$. The most important properties of the B-Splines as basis set are:

- $B(x)$ is a piecewise polynomial function of order k over $[t_i, t_{i+k}]$
- $B(x)$ is defined positive for every $x \in]t_i, t_{i+k}[$
- $B(x)) = 0$ for every $x \notin [t_i, t_{i+k}]$
- For $x = \xi_j$, $B(x) \in C^{k-q-\mu_j}$, where μ_j is the multiplicity in ξ_j. The maximum multiplicity is k and the minimum is 1, for $B(x) \in C^{k-2}$
- The *knots* do not have to be equidistant and the shape of $B(x)$ changes smoothly with the variation of the *knots*.
- Generally, to completely define a set of B-Spline functions $(B(X), i = 1, ..., n)$ it is necessary to define:

- $k > 0$
- $n > 0$
- *Knot* sequence, $(\{t_i\}_{(i=1,..,m)})$.

As k and n are fixed for a given family of B-Splines, the notation can be changed to $B^k_{t,i}$ instead of $B_i(x)$.

- Each B_i is defined in an interval $[t_i, t_{i+k}]$, that contains $k+1$ consecutive *knots*, and that is indexed by its first *knot*. This way, only one $B_i(x)$ begins on each *knot* $t_i, i = 1..n$ and ends k *knots* later.

- On each interval $]t_i, t_{i+k}[, t_i < t_{i+1}$ there are exactly k B-Splines that are not zero:

$$B_j(x) \neq 0 for j = i-k+1, ..., i \tag{4.6}$$

So, when calculating products of B-Splines:

$$B_i(x) \cdot B_j(x) = 0 for |i-j| \geq k \tag{4.7}$$

- In the expansion of an arbitrary function $f(x)$:

$$f(x) = \sum_{j=1}^{n} c_j B_j(x) = \sum_{j=i-k+1}^{i} c_j B_j(x) \quad for; \quad x \in [t_i, t_{i+1}] \tag{4.8}$$

there are only k terms that are different from zero on each interval, what simplifies the number of operations to make.

- As the B-Splines are only defined positive with minimal support the coefficients of the expansion of an arbitrary function f are close to the values of the function in the *knots*. This way the numerical stability is very high, it avoids oscillations in the coefficients (Runge phenomenon) and cancellation errors are minimum.

- Each interval $I_j = [\xi_j, \xi_{j+1}] = [t_i, t_{i+1}]$ is characterized by a couple of consecutive *knots*, $t_i < t_{i+1}$. t_i is called *left knot* of the interval I_j, and determines the indexes of the B-splines B_i that contribute to that interval I_j, $B_{i-k+1}, ..., B_i$.

- They are normalized, as $\sum_i B_i(x) = 1$ in the whole interval $[t_k, t_n]$.

- For equidistant *knots*, each B_i is just a simple translation of the previous one B_{i-1}, displaced a interval. If the *knots* are non consecutive, there is a slight change in the shape

Any function expressed as a lineal combination of B-Splines will be a piecewise polynomial in the interval $[a, b]$:

$$f = \sum_{i=1}^{n} c_i B_i \tag{4.9}$$

As de Boor shows in [100] f is the most general function made of l polynomial pieces of order k, one peace per interval I_j, joint in the inner *breakpoints* with C^{v_j-1} continuity. Trying to get continuity bigger than C^{k-2} has no sense, because doing so will lead to a one only polynomial over the interval. This kind of discontinuities in the *breakpoints* is normal in the piecewise polynomials. It is generally not necessary a special treatment of the discontinuity. The r-derivative of the function is defined as $D^r f$ as the piecewise polynomial with order $k - r$ that has the same *knot*.

4.1.2 Construction of the B-Spline functions

A set of n B-Splines of order k ($B_i^k(r)$) is constructed from the following B-Spline formula of order 1:

$$B_i^1(x) = \begin{cases} 1 & t_i \leq x \leq t_{i+1} \\ 0 & else \end{cases} \tag{4.10}$$

In order to get the polynomial of higher orders, it is necessary to apply the following recursive formula $k - 1$ times to get the k degree:

$$B_{i,k}(x) = \frac{x - t_i}{t_{i+k-1} - t_i} B_i^{k-1}(x) + \frac{t_{i+k} - x}{t_{i+k} - t_{i+1}} B_{i+1}^{k-1}(x) \tag{4.11}$$

This iterative process is illustrated in the figure 4.1.

The derivative of a k order B-Spline is another piecewise polynomial function of order $k - 1$, that can be expressed as a lineal combination of B-Splines of that order $(k - 1)$:

$$DB_{i,k}(x) = \frac{k-1}{t_{i+k-1} - t_i} B_i^{k-1}(x) + \frac{k-1}{t_{i+k} - t_{i+1}} B_{i+1}^{k-1}(x) \tag{4.12}$$

4.1.3 Practical construction example

To illustrate this procedure, an simple construction process is shown. Figure 4.3 has been constructed using the following characteristics:

- Order is $k = 3$, what implies::
  - Polynomial order is 2.

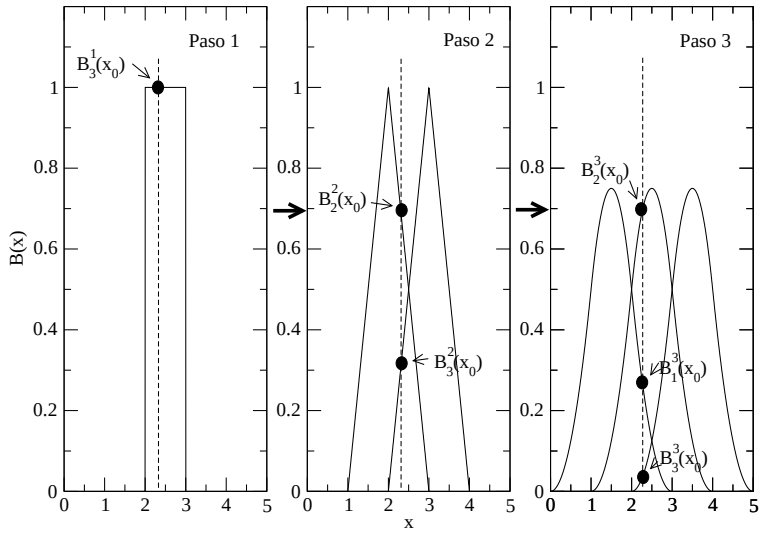

Figure 4.1: Recursive evaluation of the B-Splines up to order $k = 3$, with the *knot* sequence [0,1,2,3,4,5]. Please note that in x_0 (dashed line) there are k non-zero B-Splines

  - Only k B-Splines contribute to the function in a given point.
  - B_3 is of C^1 class, so the function and its derivative are continuum.

- The interval chosen is $I_j = [0, 5]$, divided in 5 sub-intervals ($l = 5$) by the *breakpoints* $\{1, 2, 3, 4, 5\}$ (ξ_j con $j = 1..l + 1$)
- The sequence of *knots* is $\{0, 0, 0, 1, 2, 3, 4, 5, 5, 5\}$. Multiplicity is 3 in the outer points and one for the inner *breakpoints* ($\{\mu_j\}. = \{3, 1, 1, 1, 1, 3\}$).
- Continuity ($\mu_j = k - v_j$) in the *breakpoints* (ξ_j) then is $\{0, 2, 2, 2, 2, 0\}$.
- The number of B-Splines is: $n = l + k - 1 = 5 + 3 - 1 = 7$

For the calculation of the explicit expression is necessary to apply the recursive formula, just as in 4.2.

The explicit representation of $B_3(x)$ is:

$$B_3(x) = \begin{cases} \frac{1}{2}x^2 & 0 \le x \le 1 \\ x^2 + 3x - \frac{3}{2} & 1 \le x \le 2 \\ \frac{1}{2}x^2 - 3x + \frac{9}{2} & 2 \le x \le 3 \\ 0 & e.o.c. \end{cases} \tag{4.13}$$

All figures from this section have been obtained with the programs published by the Boor.

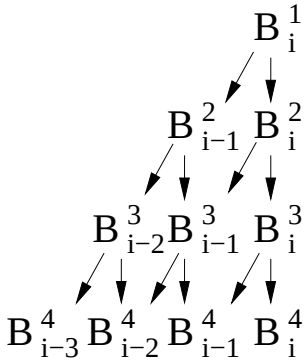

Figure 4.2: B-Spline construction scheme

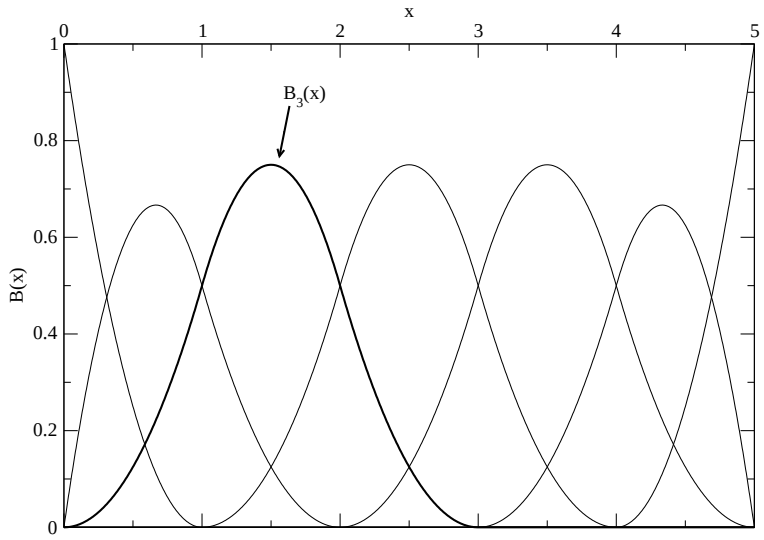

Figure 4.3: Complete set of B-Splines of order *k=3* with the knot sequence $\{0, 0, 0, 1, 2, 3, 4, 5, 5, 5\}$

4.1.4 ECS and B-Splines

Recalling the idea from the last chapter, it is necessary to build a basis set to represent a continuous function with a discontinuity in a specific point R_0. The solution for this is easy. Define the splines as $B_i^k(R(r))$, so put the *breakpoints*, ξ_i and therefore the *knots*, t_j on the complex exterior scaling contour, and place one of the *breakpoints* and its corresponding *knot* at $t_j = R_0$. Then, $B_i^k(R(r))$ has a discontinuous first derivative with respect to

r exactly at $r = R_0$, because the derivative of $R(r)$ is discontinuous at that point (see figure 4.4)

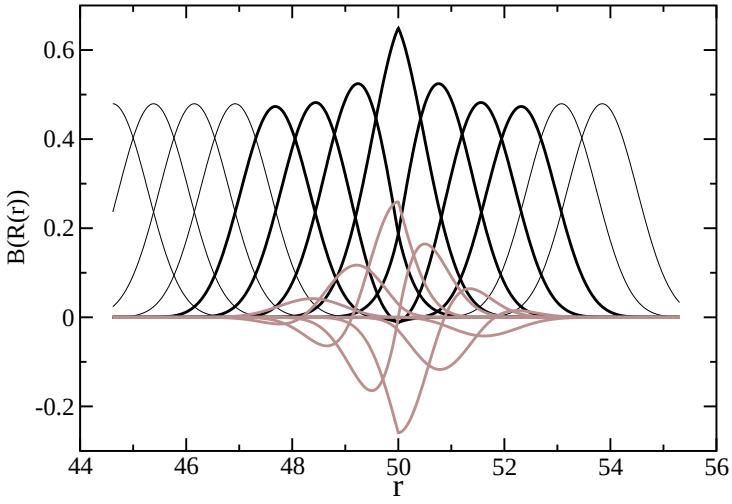

Figure 4.4: Example complex B-Spline set showing the discontinuity at $R_0 = 50$

For example, with this treatment the matrix elements of the operators considered in a one-dimensional model, simply are sums of the corresponding integrals between breakpoints:

$$
\begin{aligned}
V_{mn} &= \sum_l \int_{\xi_l}^{\xi_{l+1}} B_n^k(x) \left(V(x) + \frac{j(j+1)}{2\mu x^2} \right) B_m^k(x) dx \\
S_{mn} &= \sum_l \int_{\xi_l}^{\xi_{l+1}} B_n^k(x) B_m^k(x) dx \\
K_{mn} &= \frac{1}{2\mu} \sum_l \int_{\xi_l}^{\xi_{l+1}} \frac{dB_n^k(x)}{dx} \frac{dB_m^k(x)}{dx} dx
\end{aligned}
\tag{4.14}
$$

where $\xi_l = 0$ and $\xi_N = R(r_{max})$ is the end of the complex contour. In each interval in these sums, the integrals may be performed, for example using simple Gauss-Legrende quadrature, but only the integrals over intervals on which both B-Splines are non zero are required.

4.2 Finite-Element method implemented using a Discrete Variable Representation

The direct numerical solution of the Schrödinger equation for bound and continuum states using grid-based methodologies has gained popularity due to its several advantages. Finite-Element methods (FEM) ([103]), that also employ basis functions with compact support, just as B-Splines, offer quicker convergence and numerical stability. But, although it leads to sparse, structured matrices, easy to compute using iterative methods, FEM require the calculation of potential matrix elements, which can be computationally intensive.
The discrete variable representation (DVR) ([104]) provides a polynomial representation based upon and underlying numerical quadrature grid. With DVR the potential operator elements are diagonal and equal to the potential values at the grid points, and the kinetic energy operator elements, while not diagonal, are easily evaluable to high order. So, the idea is to combine both methods, FEM and DVR, to get the most desirable features of each method, the sparse and structured matrices of FEM, and the diagonal representation of the potential of DVR.

4.2.1 Finite-element Methods and Discrete Variable Representation

Instead of expanding the wave function in terms of global functions, in the FEM, the each independent variable is replaced by a grid of nodes:

$$0 \leq r_1 \leq r_2 \leq ... \leq r_N \tag{4.15}$$

In each interval, a set of linearly independent local functions is used to represent the wavefunction. Elementary finite-element basis functions $f_{i,m}(r)$ are defined to be identically zero outside and interval.

$$f_{i,m}(r) = 0,\ r \notin [r_i, r_{i+1}],\ i = 1, ..., N,\ m = 1, n \tag{4.16}$$

The local basis functions are arranged inside each interval with the index m, and so are the boundary conditions of the basis functions at the nodes. $f_{i,m}(r)$ should satisfy the following conditions:

$$\begin{aligned} f_{i,1}(r_i) &= 1 \\ f_{i,n}(r_{i+1}) &= 1 \\ f_{i,m}(r_i) = f_{i,m}(r_{i+1}) &= 0 \end{aligned} \tag{4.17}$$

In the case of multidimensional problems, products of one-dimensional functions to expand are used.

To ensure continuity of the wave function across each node boundary, this simple condition must be satisfied on the expansion coefficients $c_{i,m}$:

$$c_{i,n} = c_{i+1,1} \tag{4.18}$$

The discrete variable representation uses a discretization procedure that is analogous to employing a basis of grid points, in which local potential operators are represented as diagonal matrices. The way to accomplish this is to start from a polynomial basis that is connected to a Gauss quadrature rule and using that quadrature rule in evaluating all overlap and Hamiltonian matrix elements. To see the connection between DVR and FEM, first begin with the grid defined by the FEM nodes and subdivide each interval with a set of Gauss quadrature points $x_m^i, m = 1, .., n$. In order to impose the correct continuity conditions at the endpoints of each interval, a quadrature that constrains the endpoints of each interval to be included as quadrature points should be used, just as Manalopoulos and Wyatt suggested. If we consider a single interval $[a, b]$, where the numerical grid to use is defined as the Gauss-Lobatto quadrature points on the interval. This quadrature is similar to the Gauss-Legendre quadrature, as both of them numerically approximate integrals as:

$$\int_a^b F(x)dx \approx \sum_{i=1}^{n} F(x_i)\omega_i \tag{4.19}$$

Points and weights ($[x_i, \omega_i]$) are chosen to make equation 4.19 exact when $g(x)$ is a polynomial of degree $\leq 2n + 1$. Equation 4.19 can be generalized to treat definite integrals over an arbitrary interval:

$$\int_{r_i}^{r_{i+q}} g(x)dx \approx \sum_{m=1}^{n} g(x_m^i)w_m^i \tag{4.20}$$

where the points and weights have been scaled by:

$$\begin{aligned} w_m^i &= \frac{(r_{i+1} - r_i)}{2}\omega_m \\ x_m^i &= \frac{1}{2}[(r_{i+1} + r_i)x_m + (r_{i+1} - r_i)] \end{aligned} \tag{4.21}$$

The difference in Gauss-Lobatto quadrature is that, two of the points are constrained to coincide with the endpoints, $(x_1^i = r_i; x_n^i = r_{i+1})$. The rest of weights and points are chosen to make 4.20 exact for polynomials of degree $\leq 2n + 1$:

$$\int_{r_i}^{r_{i+q}} g(x)dx \approx g(r_i)w_1^i + \left[\sum_{m=2}^{n-1} g(x_m^i)w_m^i\right] + g(r_{i+1})w_n^i \tag{4.22}$$

The elementary basis functions chosen to construct the DVR based on Gauss-Lobatto quadrature are Lagrange interpolating polynomials, or also called ([96]), Lobatto shape functions:

$$f_{i,m}(x) = \begin{cases} \prod_{j \neq m} \frac{(x - x_j^i)}{(x_m^i - x_j^i)} & for \quad r \leq x \leq r_{i+1} \\ 0 & for \quad x < r_i, x > r_{i+1} \end{cases} \tag{4.23}$$

This functions, when evaluated at the quadrature points are either zero or one:

$$f_m^i(x_k^j) = \delta_{i,j}\delta_{k,m} \tag{4.24}$$

and so they satisfy the condition of equation 4.17. Using the Gauss quadrature rule of equation 4.22 to approximate all required integrals, then the functions are orthogonal:

$$\int_0^\infty f_{im}(x) f_{i'm'}(x) dx = \delta_{ii'} \int_{r_i}^{r_{i+1}} f_{im}(x) f_{im'}(x) dx \approx$$
$$\delta_{ii'} \sum_{j=1}^{n} f_{im}(x_j^i) f_{im'}(x_j^i) \omega_j^i = \delta_{ii'}\delta_{mm'}\omega_m^i \tag{4.25}$$

Then, any local operator has a diagonal representation:

$$\int_o^\infty f_{im}(x) V(x) f_{i'm'}(x) dx \approx \delta_{ii'}\delta_{mm'} V(x_m^i) w_m^i \tag{4.26}$$

The two Lobatto shape functions $f_{i,n}$ and $f_{i+1,1}$ are combined into a single *bridge* function (noted χ_{i1} to get continuity of the wave function at the interval boundaries. Those two functions are unity at r_{i+1}. The expansion of the wave function is then defined as:

$$\begin{aligned} \chi_{i1}(x) &= f_{i,n}(x) + f_{i+1,1}(x) \\ \chi_{im}(x) &= f_{i,m},\ m = 2, ..., n-1 \end{aligned} \tag{4.27}$$

Without this *bridge* functions there would be no coupling between basis functions in adjacent intervals. To ensure the wave function boundary conditions that it vanishes at $x = 0$ and $x = r_N$ are easily achieved by just simple deleting f_{11} and f_{Nn} from the basis. So, this way, the total number of basis functions is $(n-1)XN - 1$. This basis set, as defined here is orthonormal, but not normalized. To obtain a normalized basis set is necessary to do:

$$\begin{aligned} \chi_{i,m}(x) &= \frac{f_{i,m}(x)}{\sqrt{w_m^i}},\ m = 2, n-1 \\ \chi_{i,1}(x) &= \frac{(f_{i,n}(x) + f_{i+1,1}(x))}{\sqrt{w_n^i + w_1^{i+1}}} \end{aligned} \tag{4.28}$$

Some special care is needed in defining the kinetic-energy matrix, because this expansion of the wave function provides continuity at the element boundaries, but not ensures continuous derivatives. Scrinzi and Elander [105, 106] pointed out that the derivative of the wave function does not have to be continuous to correctly define the kinetic energy. Details of this particular aspect will not be given, but, as a conclusion, the kinetic energy elements in the FEM-DVR should be evaluated as:

$$T^{i,i'}_{m,m'} = \frac{1}{2}(\delta_{i,i'}\delta_{i,i'\pm 1}) \int_0^\infty dx \frac{d}{dx}\chi_{i,m}(x)\frac{d}{dx}\chi_{i',m'}(x) \tag{4.29}$$

Kinetic matrix elements are not diagonal in the DVR representation, but they are given by simple analytic formulas when evaluated using the Gauss quadrature. The required elements are evaluated in terms of the first derivatives of the Lobatto shape functions at the quadrature points, which are given by [107]:

$$f_{i,m}(x) = \begin{cases} \frac{1}{(x^i_m - x^i_{m'})} \prod_{k\neq m,m'} \frac{(x^i_{m'} - x^i_k)}{(x^i_m - x^i_k)}, m \neq m' \\ \frac{1}{2\omega^i_m}(\delta_{m,n} - \delta_{m,1}), m = m' \end{cases} \tag{4.30}$$

As seen, using the Gauss quadrature rules to approximate the integrals makes the matrix elements simple, and the basis orthonormal. This DVR-FEM representation is very flexible in adapting the grid to a specific problem, as there is absolute freedom to place the finite element boundaries, and to use different quadrature orders in each element. Also, as the connection between basis functions of adjacent elements is only made by a single *bridge* function, making the Hamiltonian matrix quite sparse.

4.2.2 ECS and FEM-DVR

The ECS transformation is applied to the finite-element boundaries, $[r_i]$, making sure that the exterior complex scaling radius R_0 coincides with one of the nodes r_I:

$$R_i = \begin{cases} r_i, & i < I \\ r_I + (r_i - r_I)e^{i\phi}, & i \geq I \end{cases} \tag{4.31}$$

This way the points are real until the grid reaches R_0, and then complex outside that radius. The points and weights of elements $i \geq I$ are defined this way:

$$\chi_{i,m} = \frac{f_{i,m}(R(x))}{\sqrt{e^{i\phi}\omega^i_m}}, m = 2, n-1, i \geq I, m \neq 1$$
$$\chi_{i,1} = \frac{[f_{i,n}(R(x)) + f_{i+1,1}(R(x))]}{\sqrt{e^{i\phi}(\omega^i_n + \omega^{I+1}_1)}} \tag{4.32}$$

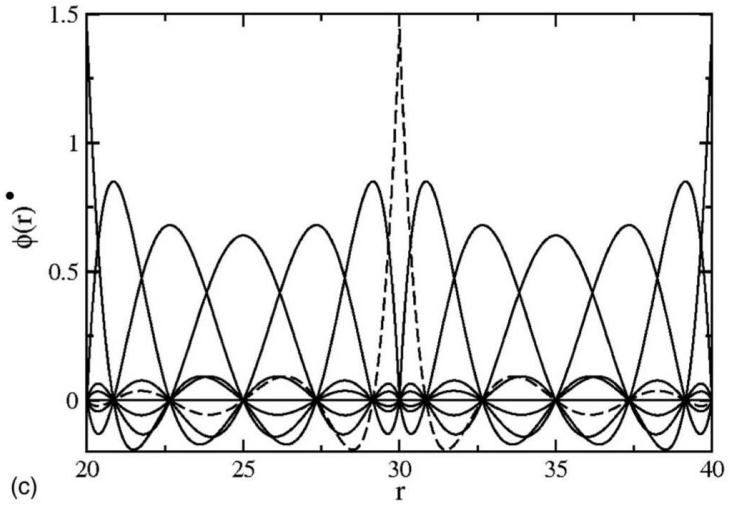

Figure 4.5: Seventh-order FEM/DVR functions plotted over two elements: the dashed curve is the central bridging function which connects the basis functions in the two adjacent elements.

The complex bridge function centered at $R_0 = R_I$ guarantees continuity of the scattered wave at the exterior scaling radius. Figure 4.5 illustrates this complex bridge function for a seventh-order FEM/DVR basis set, with R_0 placed at $r = 30$.

Part II

Results

In the following four chapters of this thesis a detailed view of the results obtained with the method explained in the theory part is presented. Each displays a specific aspect treated with this framework:

- In Chapter 5, recent experiments on single-photon double ionization of H_2 are shown. They revealed patterns suggesting the typical double slit interference, which was also observed for single photon ionization of H_2 both experimentally and theoretically ([31, 32, 33, 30, 34]). The chapter shows the calculations performed to confirm these experimental findings.

- Chapter 6 shows the two-photon ionization for the hydrogen atom. These calculations opened the way for solving increasingly complex system shown in the following two chapters.

- The two photon ionization of Helium is the subject of Chapter 7 and has been intensely discussed over the last few years. Several different theoretical methods have been applied, without providing conclusive results. Meanwhile, the current experiments carried out have not yet clarified this issue. In this Chapter, the results obtained within the ECS approach for the current two photon double ionization of Helium will be presented and compared to existing theoretical predictions.

- As an extension of the two-photon double ionization of Helium, the ECS formalism is being applied for the first time to the two-photon double ionization of the H_2 molecule. In Chapter 8 the results will be presented and compared to the only other presently available theoretical calculations [59]. Experiments on this subject have not yet been performed, but currently under preparation by different experimental groups.

CHAPTER 5

Interference patterns in one-photon double ionization of H_2

Extracted from:
D. A. Horner, S. Miyabe, T. N. Rescigno, C. W. McCurdy, F. Morales, F. Martín. Phys. Rev. Lett. ***101****, 183002 (2008)*

The angular and energy dependence of single ionization of diatomic molecules at high energies exhibit aspects of classical two-slit diffraction that are now well understood, having first been suggested by Cohen and Fano [29] in 1966, and studied by modern theoretical methods [33, 30, 34] and experiments [31, 32]. In two very recent experimental studies, surprisingly similar effects have been observed by Akoury *et al.* [35] and Kreidi *et al.* [36] for one-photon double ionization of H_2 in which two electrons are ejected with kinetic energies corresponding to wavelengths longer than the internuclear distance. These suggestive observations of double ionization were also interpreted in terms of double slit interference models. On the theoretical front, as it has been exposed in this thesis, over the past four years new computational developments have made it possible to solve the Schrödinger equation numerically for double ionization of two-electron molecules to produce effectively exact wave functions and cross sections [63, 28, 65, 47, 108, 109]. The results obtained for the photon energies used in the experiments of refs. [35, 36] show little or no trace of double slit diffraction patterns and that the apparent interference patterns arise from the use of circularly polarized light. However, it is possible to predict that the effects sought in these experiments can in fact be observed for higher photon energies.

In the experiments of Akoury *et al.* [35], the central observation was a four-lobed angular distribution seen for the faster of the two ejected electrons when it carries most of the available kinetic energy and when the other electron is not detected. These experiments use the COLTRIMS method of co-

incident detection of the electrons and the protons released by the Coulomb explosion that follows complete ionization of the H_2 molecule. For that reason the experiment is able to give kinematically complete information about double photoionization of molecules whose orientation is known. Of course, it is the knowledge of that orientation that makes the discussion of angular diffraction effects possible, and this is one of the unique qualities of this powerful momentum imaging technique. The photon energies used were 160 eV and 240 eV, corresponding to maximum available energies (from a vertical transition to the doubly ionized state) to be shared by the two outgoing electrons of 109 eV and 189 eV respectively. The observed angular distributions, shown in Fig. 5.1 were described as a "strong interference pattern" and were reproduced qualitatively by model one-electron calculations, even though the asymptotic wavelengths associated with the kinetic energies of ejection, 2.2 bohr for 160eV photons or 1.7 bohr for 240 eV photons, in the limit that one electron is ejected with all of the available energy, were larger than the equilibrium internuclear distance of the molecule, which is 1.4 a_0.

The calculations performed at these energies using the Exterior Complex Scaling (ECS) method [62] implemented with the Discrete Variable Representation in finite elements for the radial variables of each of the two electrons require considerably denser grids and more partial waves than any calculations on molecular double photoionization previously reported using these methods.

To converge the calculations at the first two energies considered here, 160 eV and 240 eV, radial grids with a maximum value of the electronic coordinate of 90 a_0 and and exterior scaling radius of 50 a_0 were used. The most dense grids contained 209 DVR polynomial basis functions for each electron. The calculations involve a single center expansion of the two-electron wave function around the center of the molecule in terms of products of spherical harmonics, $Y_{\ell_1,m_1}(\Omega_1)Y_{\ell_2,m_2}(\Omega_2)$ as explained in the theory section, and all such products with angular momenta up to and including $\ell = 9$ were included. Varying the parameters of the grid and angular momentum expansion showed these large scale calculations to be converged to graphical accuracy for all the results presented here.

The calculations produce the triple differential cross section (TDCS), $d\sigma/dE_1 d\Omega_1 d\Omega_2$, which when integrated over the angles of one of the electrons produces the doubly differential cross section (DDCS), $d\sigma/dE_1 d\Omega_1$ differential in energy sharing (specified by the energy of one electron, E_1) and the ejection angles of that electron. The results for extreme energy sharing at the two energies of the experiments are shown in Fig. 5.1. The DDCS in all four panels is plotted as a cut of the three-dimensional cross section in the plane containing the molecule and perpendicular to the photon wave

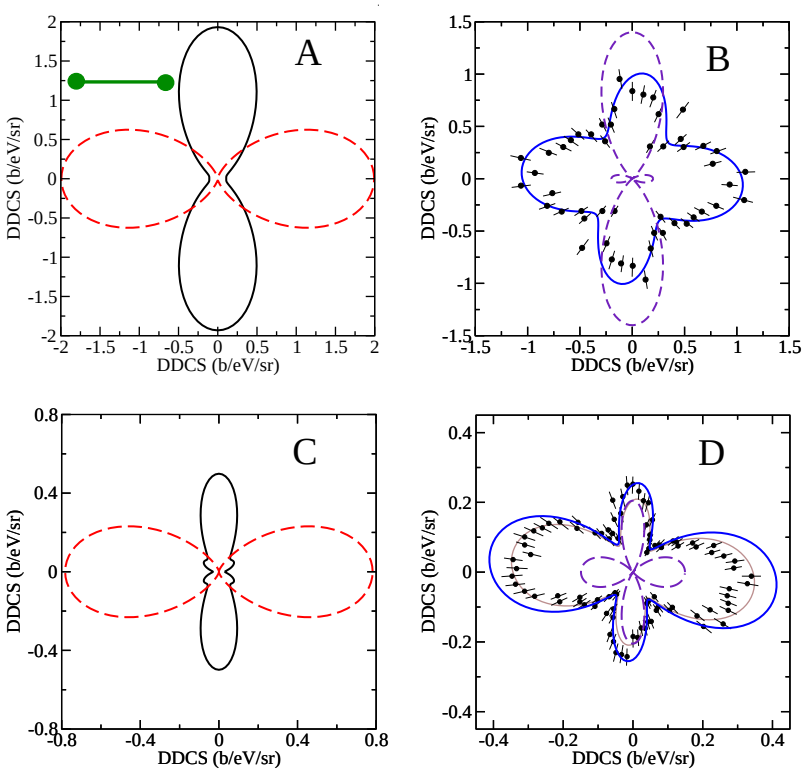

Figure 5.1: DDCS for linearly and circularly polarized radiation. Top row: photon energy of 160 eV, Bottom Row: photon energy of 240 eV. Left Column: parallel polarization (dashed) and perpendicular polarization (solid) for ejected electron energy of 108 eV. Right Column: (top) Experiment compared with calculated DDCS for circularly polarized radiation at 160 eV and ejected electron at 108 eV, and (bottom) at 240 eV with calculated DDCS for ejected electron at 187 eV (light solid) and averaged over 185-190eV (heavy solid line)

vector.

Looking at Fig. 5.1A it is shown that the DDCS for parallel and perpendicular polarization show simple dipole-like patterns with two lobes when the electron whose angular distribution is plotted is ejected with 108eV of kinetic energy, or 99% energy sharing. There is no hint of a diffraction pattern in those cross sections. However, when the amplitudes for parallel and perpendicular polarization are combined to correspond to the dipole operator for circularly polarized radiation, $(x + iz)/\sqrt{2}$, they add to form the four lobes shown in Fig. 5.1B and observed in the experiment. A key point to notice is that while at lower energies the amplitudes for double ionization

by perpendicular or parallel polarization are different by as much as a factor of five [47, 109], they are of roughly equal magnitude at 160 eV. Since one is large at angles where the other is small, the resulting angular distribution is not very sensitive to their relative phases when they are mixed by circular polarization.

At a photon energy of 240 eV a similar effect is seen. In 5.1C a simple dipole-like pattern for parallel polarization is seen, but for perpendicular polarization it can be seen just the hint of the beginning of additional lobes developing as the wavelength of the ejected electron is lowered. It is in perpendicular polarization where one expects the simple effects of diffraction to appear as the energy is raised, as has been demonstrated conclusively in the single photoionization case by accurate calculations [33].

The small lobes for perpendicular polarization in this case are completely obscured, however, in circularly polarized light as shown in Fig. 5.1D, where the origin of the four lobes is again the mixing of Σ and Π contributions corresponding to parallel and perpendicular polarization. The comparison with experiment in Fig.5.1D requires attention to the range of kinetic energies accepted in the measurements. That figure shows that while the DDCS at 99% energy sharing has almost exactly the same shape as the experimental observation, averaging the calculated results over the appropriate range of energy sharings produces a more precise match to the observation, as it should.

Additional insight into the consequences of the use of circularly polarized radiation in double ionization measurements can be seen by examining other energy sharings. In Fig. 5.2 the DDCS for energy sharings of 50, 60 80 and 95% for a photon energy of 160 eV is shown. Keeping in mind that the factor of $1/\sqrt{2}$ in the definition of the dipole operator would make the circular polarized result the average of the two linear polarizations if the relative phases were equal, it can be seen that at some energy sharings there is apparent interference of the two contributions to the circularly polarized result.

The angular behavior of the linearly polarized results at 160 eV photon energy varies rapidly with energy sharing. When the acceptance range of energy sharings in the experiment varies over a sizable range away from extreme energy sharing, the resulting peaks and valleys largely average out of the observation. This is clearly seen in the comparison with results shown in Fig 5.2E. The apparent disappearance of the interference pattern in this experiment was interpreted by Akoury *et al.* as a result of decoherence of the entangled pair of exiting electrons. That interpretation is at odds with the results of Fig 5.2F in which the DDCS for exactly 50% energy sharing is plotted in the same manner. Focusing in on a specific energy sharing, it is

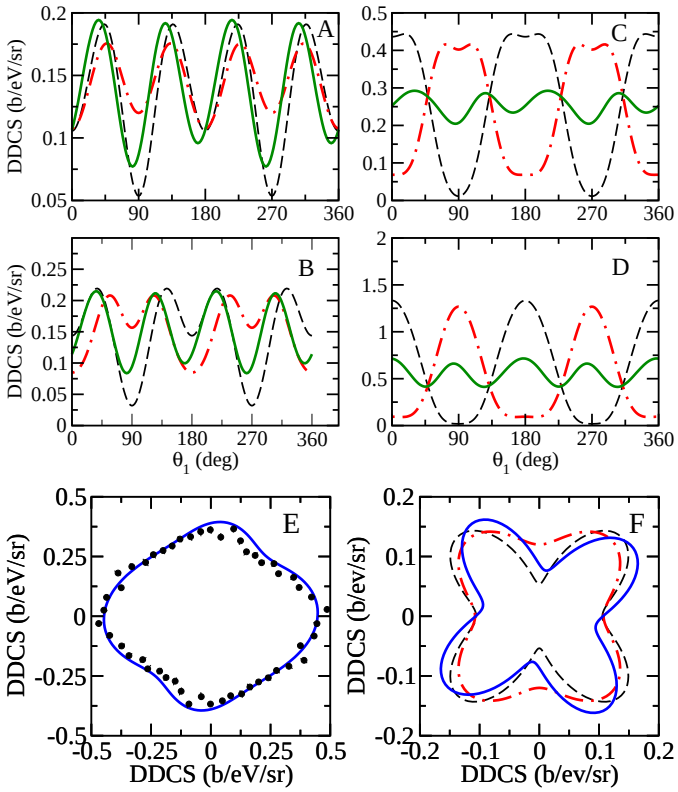

Figure 5.2: DDCS at 160eV for energy sharings of A: 50%, B: 60%, C: 80% and D: 95%, thick chained lines lines: perpendicular polarization, dashed lines: parallel polarization and solid lines: circular polarization. E: DDCS for a photon energy of 160 eV for ejected electron energy of 85-105eV compared with the results of ref. [35]. F: DDCS for a photon energy of 160 eV at 50% energy sharing, long dashed lines: perpendicular polarization, short dashed lines: parallel polarization solid: circular polarization, molecule horizontal.

shown that even at equal energy sharing circularly polarized light produces a four-lobed cross section. In this case a detailed analysis of the underlying TDCS (5.4) shows that the reason is that at this energy sharing a combination of electron repulsion in the final state and the effects of selection rules [110] for particular directions of the outgoing electrons give rise to the four lobes in the DDCS for linear polarizations. This reconstruction is particularly more accurate with higher energies, as it is shown in figure 5.4.

The effects of electron correlation can be seen most directly when the TDCS is plotted as a function of the angle between the directions of the two ejected electrons, as Akoury *et al.* pointed out [35] when displaying their coincidence measurements of the angular distributions. In Fig. 5.3 ex-

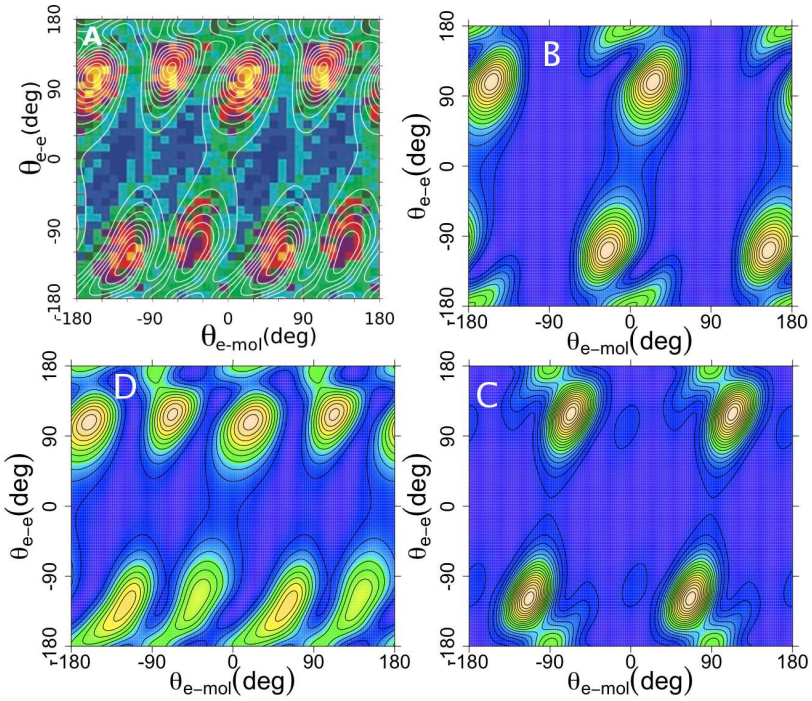

Figure 5.3: TDCS at photon energy of 160 eV plotted as function of angle of faster electron with molecular axis and angle between electrons. A: Experiments with circular polarization of ref [35] with ECS calculations superimposed as contours. Data includes all energy sharings between 78% and 96%. B: ECS calculations for parallel polarization for ejection energy of 108 eV (99% energy sharing). C: Corresponding calculations for perpendicular polarization. D: Calculations for circular polarization.

perimental measurements and the converged calculations of the TDCS are shown. The TDCS is shown in contour plots as a function of the angle between the faster electron and the molecular axis and the angle between the two electrons. Fig 5.3A shows the experimental results - which use circularly polarized light and are integrated over energy sharings between 78% and 96% - plotted with both electrons near the plane perpendicular to the direction of light propagation that contains the molecule. That is the range of energy sharing that produces the nearly featureless DDCS in Fig 5.2E.

Akoury *et al.* argued that the two rows of four maxima in Fig 5.3A arise from two-slit-like interference of one of the entangled pair of electrons which also has a binary collision with the other electron, ejecting it at characteristic values of θ_{12} near 90°. In this interpretation, integrating the data of Fig. 5.3A over all Θ_{e-e} destroys the four-lobed interference pattern, because

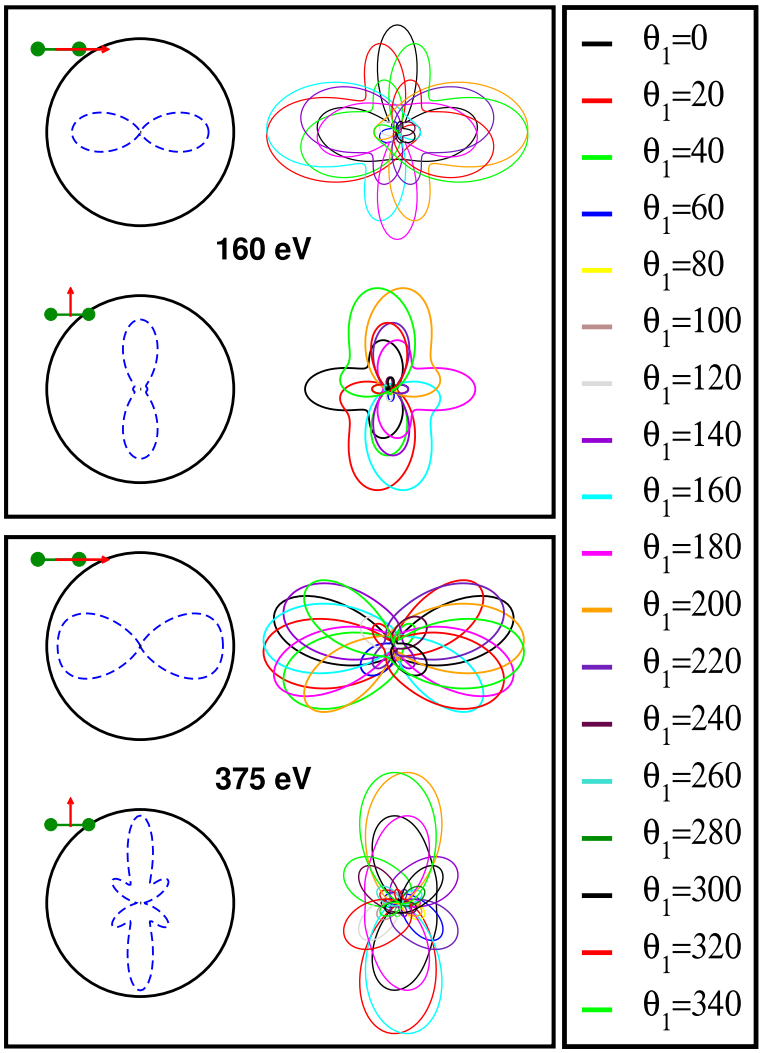

Figure 5.4: DDCS (figures inside a circle) for photon energies of 160 eV and 375 eV and 99% energy sharing, for both parallel and perpendicular cases. Besides each case, TDCS for different orientations of the fixed electron.

doing so obscures the electrons' quantum entanglement. The interference pattern is only recovered when one integrates over particular ranges of Θ_{e-e}.

However, the essentially exact calculations for extreme energy sharing shown in Figs. 5.3B and 5.3C indicate that the perpendicular and parallel polarizations show only a simple dipole pattern in θ_{e-mol} superimposed on the typical "binary peak" that is generally interpreted in atomic double photoionization as arising from a collision of the electrons during the ejec-

tion process. Circular polarization, which is a combination of parallel and perpendicular amplitudes, produces Fig. 5.3D, which is nearly identical to the experiment in Fig. 5.3A. Moreover, by averaging such calculated cross sections over the energy sharing range in the experiment in Fig. 5.3A the calculations reproduce it almost exactly. Those calculations are also shown in Fig 5.3A superimposed as contours on the original data of Akoury *et al.* Thus the conclusions is that the experiments at photon energies of 160 and 240 eV have not in fact demonstrated the expected physical effects of quantum interference and entanglement but rather only the superposition of the contributions of parallel and perpendicular polarization.

So do those fundamental quantum effects sought by the authors of refs. [35] and [36] not exist in molecular double photoionization? To answer that question, converged ECS calculations of the TDCS for a photon energy of 375 eV were also performed. At this energy the minimum asymptotic wavelength of the ejected electrons is 1.3 bohr, and is comparable to the internuclear distance of ground state H_2. Results analogous to those in Fig 5.1 for this case are shown in Fig. 5.5. Here it is possible to see that in perpendicular polarization the DDCS shows a pronounced six-lobed shape that is reproduced qualitatively by the simple two-slit diffraction formula, $(\boldsymbol{\epsilon}\cdot\mathbf{k})^2\cos^2\left[k_e R\cos(\theta_{\text{e-mol}})/2\right]$. The coherent combination of perpendicular and parallel amplitudes that represents circular polarization produces the DDCS shown in Fig. 5.5B that unfortunately nearly obscures four of those six lobes. However, the simple diffraction formula for circular polarization, $\cos^2\left[k_e R\cos(\theta_{\text{e-mol}})/2\right]$ nearly reproduces that result.

As a reinforcement of this argument, two more results will be shown. Attending to the diffraction formula presented before, there are two parameters related with the molecular case than can be changed. This variation should induce changes in the shape of the additional lobes which are related with the two-slit diffraction patterns.

The first calculations are done for a photon energy of 375 eV, and have been performed at different internuclear distances (between 1.0 and 1.8 a.u.) and for 99% energy sharing, as the variation of the internuclear distance will be the equivalent of changing the separation between the two slits in the simple formula shown below. This variation induces a change in the angle and relative size of the lobes of two-slit diffraction patterns. Hence, it should induce similar changes (angle and relative size) in those lobes of the DDCS which are directly related to a two-slit diffraction pattern. Figure 5.6 shows the results for parallel, perpendicular and circularly polarized cases, superimposed with the results of the diffraction model. For the perpendicular case, a clear development of the additional lobes can be seen. Not only these four additional lobes grow in size, but also the angle they form with the lobes

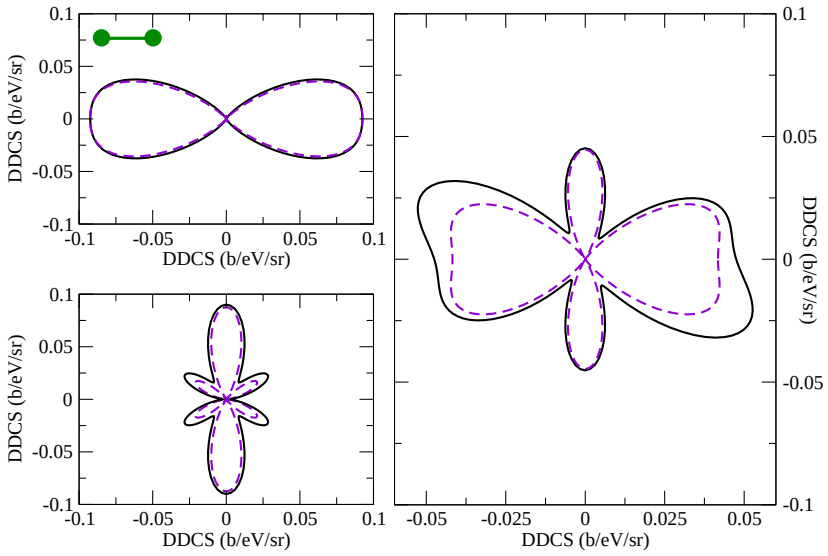

Figure 5.5: DDCS for a photon energy of 375 eV and 99% energy sharing. Left: Parallel (upper panel) and perpendicular (lower panel) polarization. Right: Circular polarization. Dashed curves: Simple diffraction model

fixed at 90 and 270 degrees changes with the internuclear distance. The parallel case also suffers certain changes with the variation of the internuclear distance, but neither of them in relative sizes or in relative angles. Circularly polarized results show no more than the combination of both perpendicular and parallel case, as discussed above.

Another proof of the conclusions exposed here can be obtained by incrementing the photon energy, which will increment k in the simple diffraction model. This would also imply that the size and the angle of the additional lobes will change. Results for a photon energy of 500 eV with an energy sharing of 99% (this means that ejected electron takes $\approx$ 444 eV) are shown in figure 5.7. The additional lobes that appear in the perpendicular case are bigger in relative size with those of 5.5, reinforcing the conclusions exposed in this chapter.

A repetition of such experiments with linear polarization should reveal the correctness of the present interpretation and our predictions for these photon energies. However for photon energies at or above 375 eV we predict

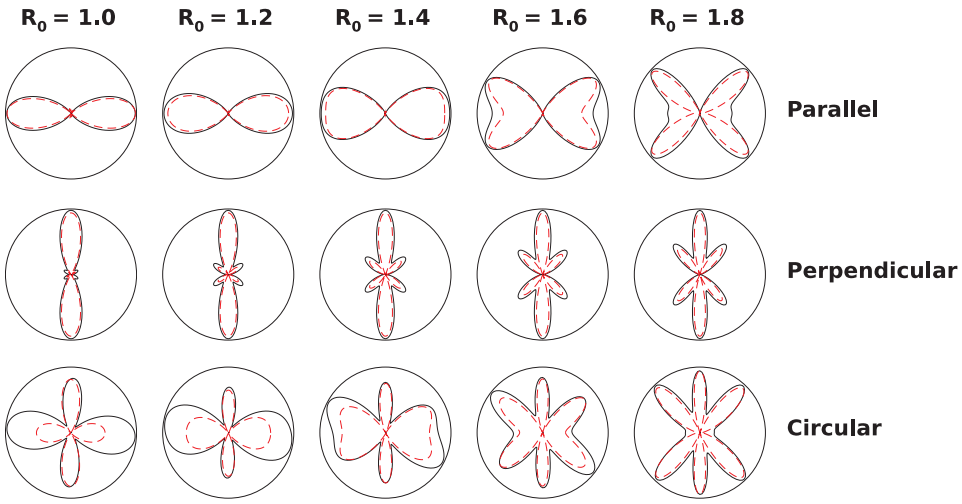

Figure 5.6: Comparison between parallel, perpendicular and circular DDCS obtained for different internuclear distances (in a.u. in the figure), for a photon energy of 375 eV and 99% energy sharing.

that the dramatic demonstration of quantum interference and entanglement in double photoionization will in fact be found.

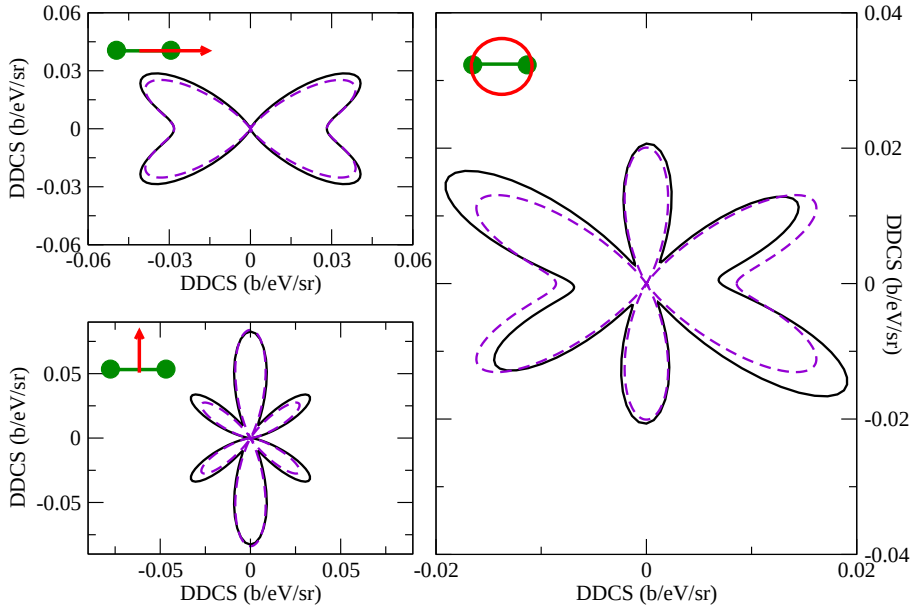

Figure 5.7: DDCS for a photon energy of 500 eV and 99% energy sharing. Left: Parallel (upper panel) and perpendicular (lower panel) polarization. Right: Circular polarization. Dashed curves: Simple diffraction model

5.1 Total cross section, single differential cross section and 3D triply differential cross sections

For all the photon energies calculated in this study, not only DDCS where obtained. As a continuation of work in references [63, 28, 65], total cross section, single differential cross sections, and triply differential cross sections where also obtained.

In the Fig.5.8, total calculated cross section, for the photon energy range of [53.9:75.66] eV [63], and the total cross section for 75 eV [65] are shown together with the total cross section calculated here. It must be noted, that although the methodology used is the same, both the basis set used, and the number of angular momenta of the final states included in the previous calculations [63, 65] are smaller than in the present results. As expected, this leads to a discrepancy in the value of the total cross section. Contributions from $^1\Sigma_u^+$ and $^1\Pi_u$ final states are also shown.

In Fig. 5.9 a comparison of the newly calculated single differential cross sections is shown (SDCS, differential in the energy sharing between the ejected electrons). These results complement those in [63], where the au-

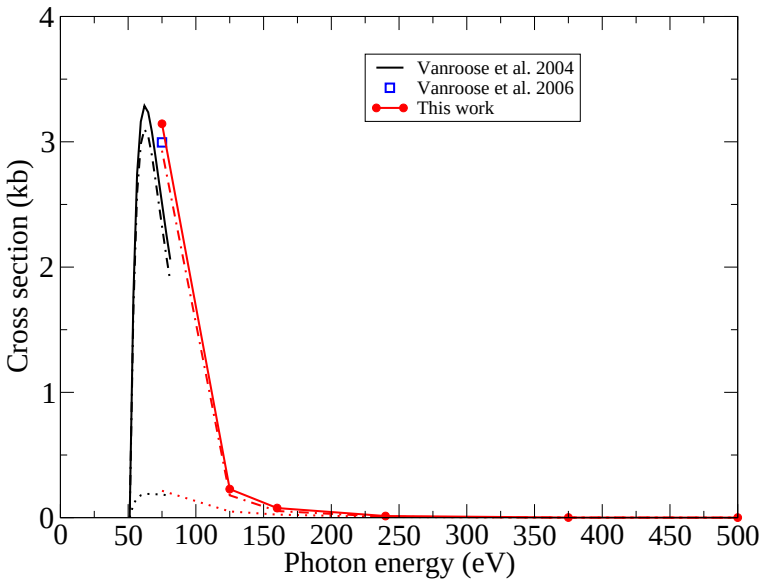

Figure 5.8: Total cross section for the one photon double ionization of H_2. In black are the results from [63], blue squares shows the total cross section from [65], and shown in red current are the results. The continuous line show the total cross sections, while dotted lines mark the $^1\Sigma_u^+$ contribution, and dashed-dotted lines the $^1\Pi_u$ contribution.

thors found that the probability of ejecting one electron which is taking most of the energy is bigger than the probability of both electrons sharing equal energies. The latter was the case for photon energies close to the double ionization threshold. Figure 5.9 shows that this tendency is kept for higher photon energies as well. Results for 500 eV begin to show evidence of a lack of convergence, mainly for two reasons: higher energies require larger numerical box sizes and more angular momenta for the final state, and the cross section becomes smaller when the photon energy is increased.

In Fig. 5.10 the three dimensional triply differential cross sections (TDCS) are shown for all the calculated energies. The molecular orientation with respect to the polarization axis, the fixed direction of the ejected electron, and the electron energy sharing is the same as in reference [28]. Although most often these three dimensional plots are difficult to study and to compare, sometimes they can be helpful to find how features of the TDCS evolve when changing the incident photon energy. In this particular arrangement, it can

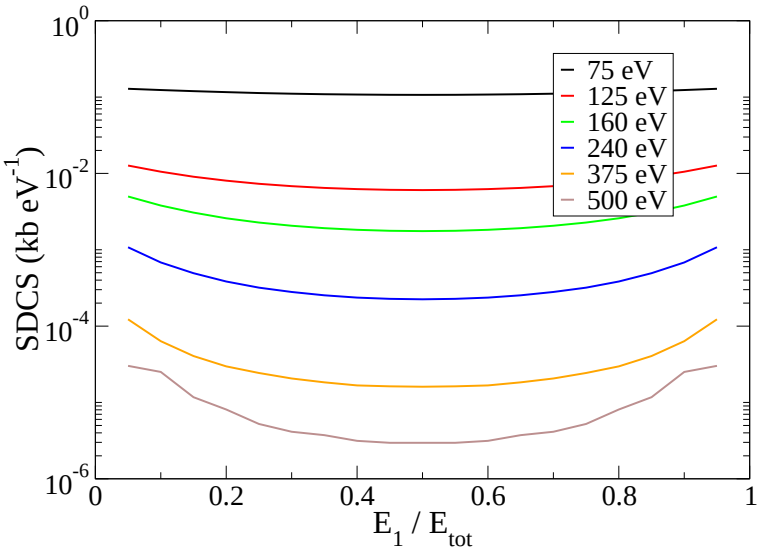

Figure 5.9: Single differential cross sections (SDCS), differential in the electron energy sharing for all the calculated photon energies.

be seen that the lobe most prominently shown at 75 eV, represents back to back emission of the non-fixed electron, which progressively disappears when increasing the photon energy. For higher photon energies the biggest cross section lobes (i.e. probability of ejecting of the non-fixed electron) appear at a 90^o angle with the plane containing both the polarization and the molecular axis.

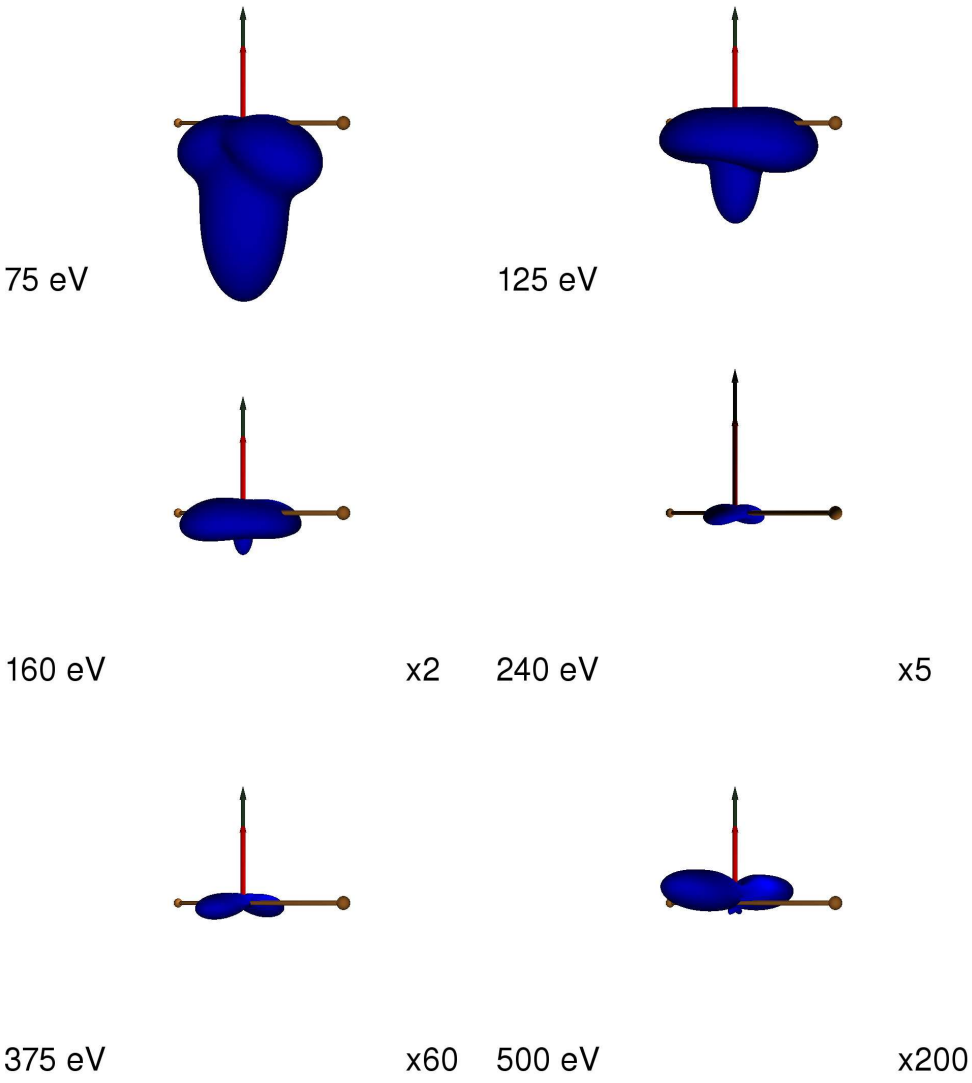

Figure 5.10: Three dimensional TDCS with the direction of the ejected electron fixed as shown by the red arrow taking 90% of the available energy along the polarization axis (green arrow). The molecule is represented in golden.

CHAPTER 6

Two-Photon Ionization of the Hydrogen Atom

As an initial test of the two photon theory explained in the previous Chapters, the most simple atomic case - the hydrogen atom - was verified. In this Chapter the results for the H atom, and the consequent conclusions obtained from this study are presented. Theoretical results for the two photon ionization of H were performed by Karule in 1985 [111], making this system an ideal candidate to test the validity and accuracy of the two photon method from the theoretical part. The expression for the cross section in Karule's paper is different from the cross section expressions seen in the theory part. His calculated two photon ionization is taken from the explicit form of the Coulomb Green's function:

$$\frac{Q^{(2)}}{I} = 2\pi^2 \alpha a_0^2 I_0^{-1} \omega(|f_2(k_1)|^2) \tag{6.1}$$

where $I_0 = 14.038 \times 10^{-16} W/cm^2$, and the final state functions in the definition of the amplitudes are energy normalized.

6.1 Hydrogen atom energy diagram: Below and above threshold ionization

In all the two photon processes studied here, both photons have exactly the same energy. Figure 6.1 shows the energy diagram of the atomic hydrogen for the possible two photon ionization processes, for which process depend on the photon energy. The first process, represented with dark green arrows, describes the below threshold ionization (BTI), which is the simultaneous absorption of two photons of the same energy, in which the energy of a single photon is not sufficient to ionize the atom. Then, the intermediate state in equation (3.54), if any, is a bound (excited) state. The second case,

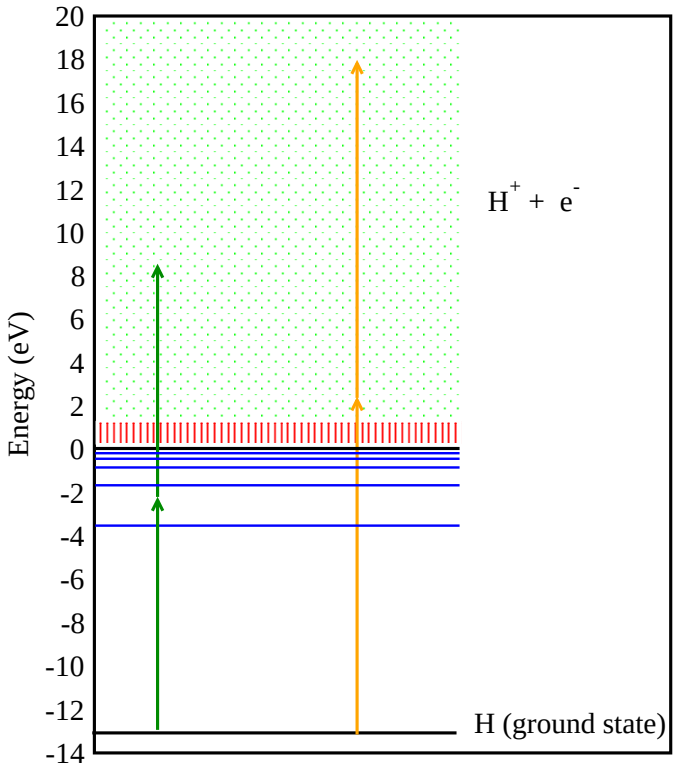

Figure 6.1: Hydrogen energy diagram showing the below and above threshold ionization processes. The dark green arrows correspond to a two-photon ionization within the below threshold ionization region. Orange arrows shows a two-photon ionization with photon energies that correspond to the ATI region.

shown with orange arrows in Fig.6.1, represents the above threshold ionization (ATI). Here, the individual energy of the photons is large enough to ionize, and, therefore, the intermediate state in equation (3.54) is a continuum state. This is the most interesting case, as the theoretical, and, in particular the numerical representation of the intermediate single-ionization continuum state constitutes a significant challenge.

6.1.1 Results for the below threshold ionization

Figure 6.2 shows the results of the total cross section for the two photon ionization of the hydrogen atom for the below threshold ionization. The results agree with those of reference [111], both velocity and length gauge. This is expected, as, the intermediate state is a bound state. With increasing photon energy it can be seen that cross section starts to differ for the length and

the velocity gauge. In addition the cross-sections begin to oscillate wildly, as a consequence of the proximity to the continuum states for the intermediate state. The series of peaks in figure 6.2 corresponds to the Rydberg series of states which lie below the ionization threshold. These Rydberg states are electronically excited states, which, in this case, are reached after a simultaneous two-photon absorption. The closer the photon energy is to the ionization threshold, the higher the principal quantum number is, and the smaller the energy difference between these Rydberg states is. Each of these states is represented by a pole in perturbation theory formulation (i.e. as the difference energy between the addition of the ground state energy plus the photon energy is exactly equal to the excited state energy), and, then, its height should be infinite. The absence of this divergence in the results is due to the fact that the photon energy grid is not dense enough. The finite size of the basis set used is responsible for the poor description of the Rydberg states that lie just below the ionization threshold. These states are infinite in number, and they grow closer and closer with the photon energy, making them impossible to represent with a finite basis set.

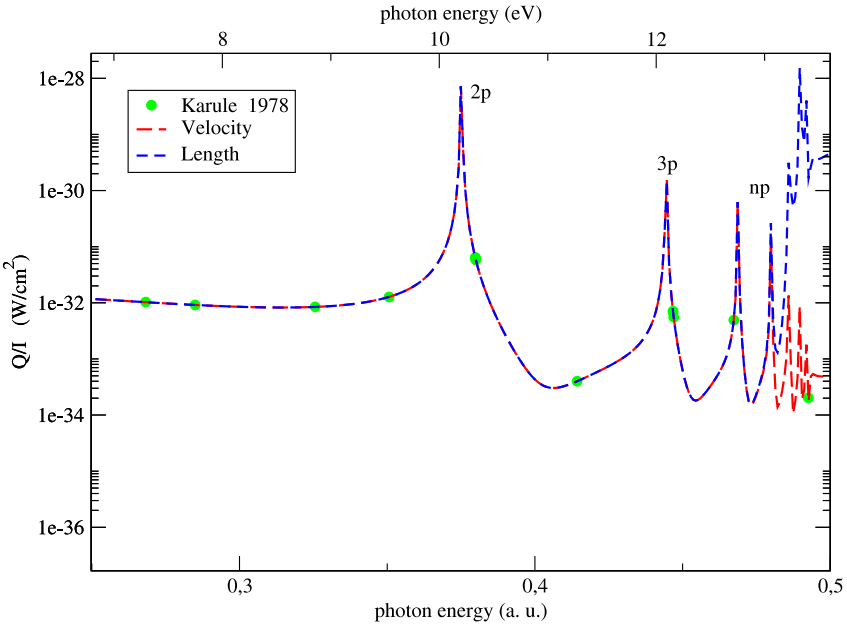

Figure 6.2: Ionization rate for the two-photon double ionization of the hydrogen atom for the BTI region calculated in the length and velocity gauge.

6.1.2 Results for above threshold ionization

In figure 6.3 the combined results for BTI and ATI photon energy ranges are shown. The incorrect oscillatory behavior of the cross sections in the region close to the ionization threshold seen in the previous figure, now gets extended all over the ATI region. This is the effect of having a intermediate state with an electron already in the continuum. It can also be seen that differences between gauges becomes clearer, as velocity gauge, although giving incorrect results, is able to converge faster, and yields results closer to the ones in [111]. Applying the 'complex' photon energy formalism discussed in

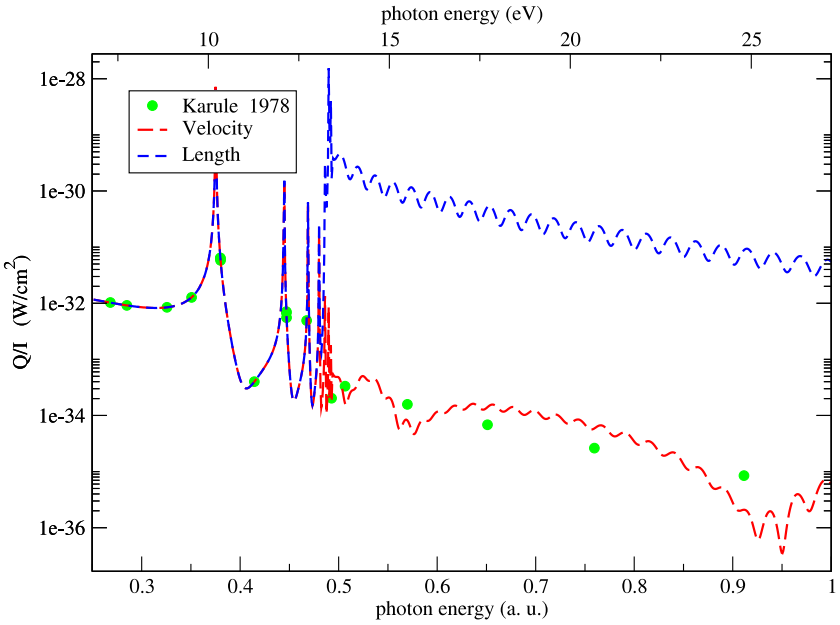

Figure 6.3: Length and velocity gauge calculated ionization rate for two photon ionization of H in the ATI region.

the theory part of this thesis, the results obtained are shown in figure 6.4. As it can be seen, the oscillations observed in the ATI region decreases as the complex part of the photon energy is increased. The oscillatory behavior ends up converging at a certain value of the imaginary part of ω, which, in this case, can be used to obtain the real value of the cross section. The agreement with the results of [111] for the cases with the imaginary part of the first photon energy equals 0.1 and 0.2 eV is now perfect. This complex value of ω avoids the divergence induced by having one electron in the con-

tinuum, as discussed in the theory section. It also has the same effect over the Rydberg series discussed in the BTI case. The higher is the complex part of the photon energy, the smoother the Rydberg states peaks are, as their divergence is also removed with the inclusion of the complex part in the first photon energy. The ATI region does not show any divergence peaks, as the first photon already has enough energy to take the electron into the continuum, and, therefore, it does not excite a state with a given principal quantum number. More details on the practical use of the complex photon energy strategy will be discussed in chapters 7 and 8.

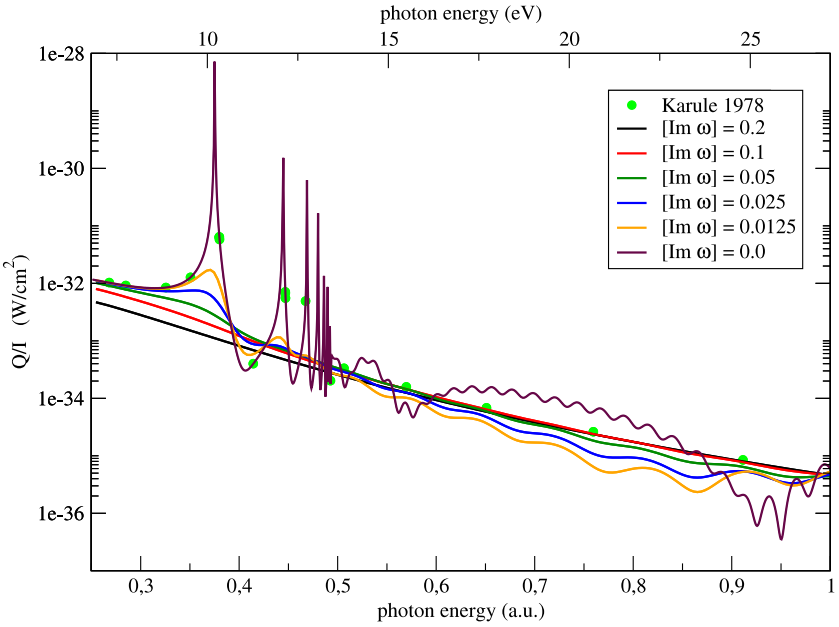

Figure 6.4: Velocity gauge for several values of the imaginary part of the photon energy calculated ionization rate for two photon ionization of H in the ATI region.

CHAPTER 7

Two-Photon Double Ionization of Helium

Extracted from:
D. A. Horner, F. Morales, T. N. Rescigno, F. Martín, C. W. McCurdy. Phys. Rev. A ***76****, 030701 (2007)*

Double ionization of the helium atom by two XUV photons in the range of 40 to 50 eV has recently become the subject of intense theoretical interest [37, 38, 39, 40, 41, 42, 43, 44, 45, 46, 47, 48, 49, 50, 51, 52, 53, 54] as well as the target of new experiments with high harmonic generation sources [55] and experiments underway at the free-electron laser source (FLASH) in Hamburg ([56, 57]). Even in the intensity regime where second order perturbation theory is expected to be valid, recent calculated cross sections vary over more than an order of magnitude. Here, the methodology exposed in the theory part is used to get results of this process both below and above the energetic threshold for sequential ionization. In two-photon double ionization, the relative importance of interaction and correlation varies dramatically as both the total energy and energy sharing between the outgoing electrons is changed, particularly above 54.4 eV where the sequential and non-sequential double ionization processes compete. Multiphoton ionization with new XUV sources offers a new context in which to probe the effects of electron correlation in a Coulomb breakup process.

7.1 Helium energy diagram for two photon ionization

Before discussing the results of the two-photon double ionization in detail, an explanation of the different regions accessible depending on the photon energy ranges will be given. As explained in Chapter 6, the two photon ionization processes (where both photons have exactly the same energy)

critically depends on the photon energy. For the Helium atom, which has two electrons, there are more two-photon interaction pathways than for the case of the hydrogen atom. Figure 7.1 shows a schematic energy diagram of the helium atom, where four different regions can be distinguished:

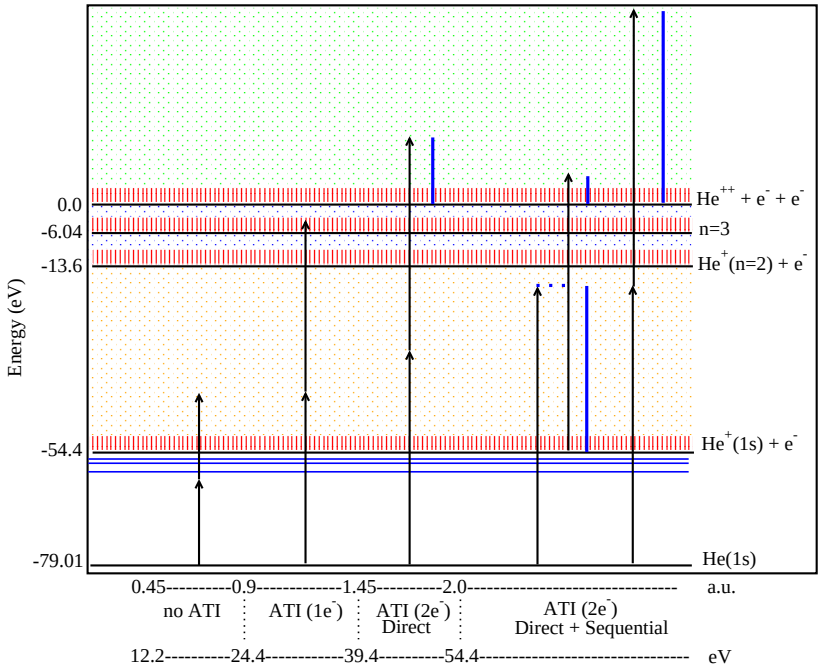

Figure 7.1: He energy diagram showing below and above ionization threshold

- Non above threshold ionization (ATI) region (photon energy between $(12.2 - 24.4)$ eV): The first photon does not ionize the atom, and the intermediate state, if any, is just an excited state. This is equivalent to the below threshold ionization (BTI) in the hydrogen atom.
- First ATI region (photon energy between $24.4 - 39.4$ eV): In this region, the first photon has enough energy to promote one electron over the first ionization threshold into the continuum. However, the second photon does not provide sufficient energy to reach the double ionization threshold. This is the equivalent of ATI in the hydrogen atom.
- Second ATI region (photon energy range between $39.4 - 54.4$ eV): This is the region to be studied in detail in this Chapter. The energy resulting from adding the two photon energies is large enough to reach the double ionization threshold, allowing for ejecting both of the electrons. The only possible way to reach the double ionization threshold is the simultaneous absorption of the two photons, which is called **direct** double ionization.

- Third ATI region (photon energy above $54.4eV$): In this case **direct** ionization is not the only way of reaching the double ionization threshold. It is also possible that after an electron is ejected the first photon absorption, resulting in an He^+ ion in a bound state, which may then absorb the second photon. This is called **sequential** ionization.

The interference of the latter two double ionization processes (direct and sequential) is the subject of this study. As a proof of the validity of the method, results for the first two regions will be shown in the following two subsections.

7.1.1 Results for below threshold two-photon ionization of helium

Figure 7.2 shows the results of applying the methodology described in the theory section to the problem of the two photon single ionization of He in the first photon energy region (i.e. $12.2 - 24.4$ eV). Results are shown independently for the S and D partial waves, which are available in the literature for comparison ([112]). In the figure it can be seen, as in the

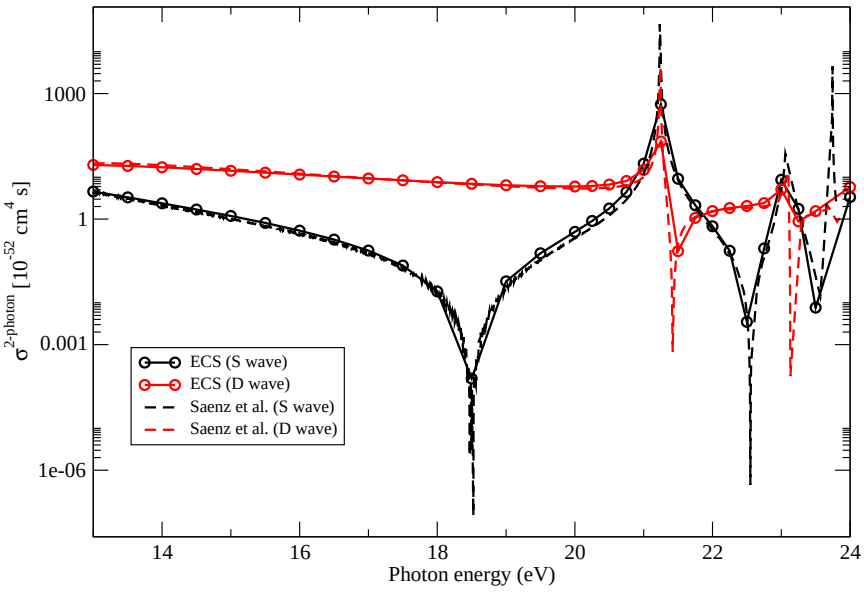

Figure 7.2: Two photon single ionization cross section for S and D partial waves compared with results of [112]

case of the hydrogen atom, the series of states representing the one electron excitations that corresponds to the Rydberg states below the first ionization threshold. As in the previous case, the lack of calculated points, the size of the basis and the number of included angular momenta, leads to a less accurate description of these states closer to the threshold.

7.1.2 Results for above threshold two-photon single ionization of helium

Figure 7.3 displays the results for the second region described in figure 7.1 for photon energies in the range of $(24.4 - 39.4$ eV). Since the first photon already ionizes the system, the results shown here have been obtained from an extrapolation scheme using a complex energy for the first photon, as outlined in Section 3.3. The figure shows a non-definitive test performed in this region, for a small range of imaginary contributions to the photon energy ω for the first photon (specifically for $0.125 - 0.300$). These results, also separated into S and D partial waves, are compared with other results found in the literature [38, 113, 114, 8]. Although there are different levels of agreement with other theoretical calculations, it affects a region outside the primary purpose of this study. Here, the first two doubly excited states

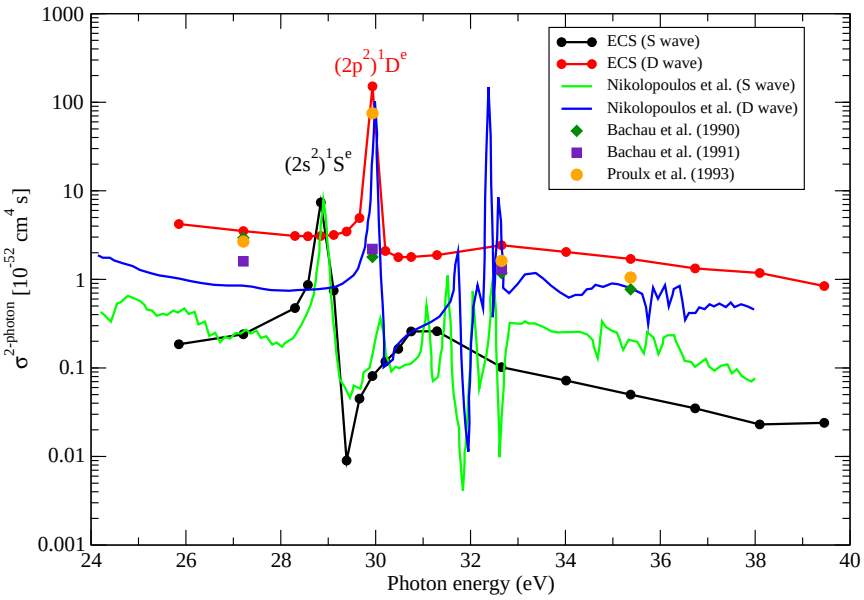

Figure 7.3: Two photon single ionization cross section for He for the photon energy region between $24.4 - 39.4$ eV. Results are compared with those in references [38, 113, 114, 8]

can be identify in the shown results. The doubly excited states are excited bound states where both electrons are excited. These states, after a given time (lifetime), will eject one of the two electrons, leaving the remaining ion in a bound state. This is also an electron correlation effect, and, therefore, another justification for the interacting two electron description. Because of the limited number of points, only one doubly excited state of each symmetry (S and D) can be seen in this calculation. While confirming the numerical

approach used in this thesis, is not the aim of this study, as it has already been treated in the literature [38, 113, 114, 8].

However, the present calculation shows the beginning of continuum-continuum transitions affecting every single theoretical approach for the two photon above threshold ionization. The representation of the wave function of an atom with one electron ejected already poses a significant challenge. As shown for the hydrogen atom, the use of an imaginary part in the first photon energy, can remove the divergences that arise from these f transitions. It mas be taken into account, however, that this procedure also smooths any divergence that appear when exciting a Rydberg state, or a doubly excited state. These states should appear as a peak with infinite height, but, for the reasons given in the previous section, the description of these states is not as accurate as it could be.

After verifying the numerical method with these two initial test cases, the next photon energy region can be studied. In this region allows for both electrons being ejected to the continuum. In addition to the direct ionization, the non-sequential ionization channel becomes accessible and increases the complexity of the underlying calculations.

Once this two cases have been checked, it is time to go into the next energy region, which, not only maintains the difficulties exposed here, but also adds a new one. Now both electrons are removed from the atom, and one new possibility is open, as now, direct ionization is not the only channel, and the effects of sequential ionization should manifest.

7.1.3 Results for above threshold ionization two-photon double ionization of helium

The cross section for two-photon double ionization from lowest order perturbation theory (LOPT) in the velocity gauge, differential in the energy sharing and angular dependence of the ejected photo-electrons, is given by the expression already seen in (1.23):

$$\frac{d\sigma}{dE_1 d\Omega_1 d\Omega_2} = \frac{2\pi}{\hbar}\frac{(2\pi\alpha)^2}{m^2\omega^2} k_1 k_2 |f(\mathbf{k}_1, \mathbf{k}_2, \omega)|^2 \,, \tag{7.1}$$

where $\mathbf{k}_1$ and $\mathbf{k}_2$ are the momenta of the photo-electrons, ω is the photon frequency, m is the electron mass and α is the fine-structure constant. The amplitude $f(\mathbf{k}_1, \mathbf{k}_2, \omega)$ is in turn given by

$$f(\mathbf{k}_1, \mathbf{k}_2, \omega) = \langle \Psi^-_{\mathbf{k}_1,\mathbf{k}_2} | \mu [E_0 + \hbar\omega - H + i\epsilon]^{-1} \mu | \Phi_0 \rangle \,, \tag{7.2}$$

where H is the atomic Hamiltonian, Φ_0 is the initial state of the atom with corresponding energy E_0, $\Psi^-_{\mathbf{k}_1,\mathbf{k}_2}$ is the full momentum-normalized scattering wave function, with incoming boundary conditions corresponding to two free electrons, and the dipole operator, μ, is defined in terms of the momentum operators, $\mathbf{p}_i$, for the two electrons, $\mu = \mu_1 + \mu_2 = \boldsymbol{\epsilon} \cdot \mathbf{p}_1 + \boldsymbol{\epsilon} \cdot \mathbf{p}_2$.

As seen before, there are a number of obstacles associated with an accurate evaluation of the amplitude in Eq. (7.2). One of those is coping with the infinite sum over intermediate states that follows from making a spectral expansion of the resolvent operator $[E_0 + \hbar\omega - H + i\epsilon]^{-1}$. However, the major obstacle is the calculation of the double-continuum state $\Psi^-_{\mathbf{k}_1,\mathbf{k}_2}$ and the difficult boundary conditions associated with three-body Coulomb breakup.

In order to address these, as it already has been seen in the theory part, problems by beginning with the coupled (Dalgarno-Lewis) driven equations that describe two-photon absorption in LOPT,

$$(E_0 + \hbar\omega - H)\Psi_1^{\mathrm{sc}}(\mathbf{r}_1, \mathbf{r}_2) = \mu\Phi_0 \tag{7.3}$$

$$(E_0 + 2\hbar\omega - H)\Psi_2^{\mathrm{sc}}(\mathbf{r}_1, \mathbf{r}_2) = \mu\Psi_1^{\mathrm{sc}} \,, \tag{7.4}$$

both of which must be solved with purely outgoing-wave boundary conditions, and the second of which describes two-photon absorption. Then a large (in the present case six-dimensional), but finite volume beyond which the electron-electron interaction can be safely ignored is chosen and then solve Eqs. (7.3) and (7.4) on that finite volume to arbitrary accuracy. The problem of the boundary conditions for both of these equations is addressed in this approach by making using the method of *exterior complex scaling* (ECS) [96], which scales the electron coordinates by a phase factor, but only

outside the chosen finite volume, thereby inducing an exponential fall-off in the outgoing wave part of the continuum wave function beyond the finite volume. By expanding $\Psi_1^{\rm sc}$ and $\Psi_2^{\rm sc}$ in a truncated product basis of spherical harmonics Eqs. (7.3) and (7.4) can be converted into a set of coupled two-dimensional radial equations that can be solved on parallel computers with sparse matrix methods.

Having solved the coupled equations, the strategy for calculating the amplitude, explained in the theory part, for double ionization is taken, which is formally contained (to within an overall phase) in the asymptotic behavior of the solution for $\Psi_2^{\rm sc}$,

$$\Psi_2^{\rm sc} \underset{\rho\to\infty}{\sim} \sqrt{2\pi i}\left(\frac{K^3}{\rho^5}\right)^{1/2} e^{iK\rho+\zeta\ln 2K\rho} f(k_1\hat{\mathbf{r}}_1, k_2\hat{\mathbf{r}}_2, \omega) \tag{7.5}$$

where $\rho = \sqrt{r_1^2 + r_2^2}$, the energy shared by the outgoing electrons is $K^2/2 = k_1^2/2 + k_2^2/2$, and the angle dependent coefficient of the logarithmic phase is

$$\zeta = Z/k_1 + Z/k_2 - 1/|\mathbf{k}_1 - \mathbf{k}_2|. \tag{7.6}$$

As it has been shown [62], in the contexts of both double photoionization and electron impact ionization, the amplitude can be extracted (to within an irrelevant volume-dependent overall phase) using a surface integral that involves a pair of testing functions $\psi_{\mathbf{k}}^-(\mathbf{r})$ which are momentum-normalized, one-electron Coulomb functions with nuclear charge Z=2, in the case of helium:

$$\begin{aligned} f(\mathbf{k}_1, \mathbf{k}_2, \omega) = \frac{1}{2}\int \Big(&\psi_{\mathbf{k_1}}^{-*}(\mathbf{r_1})\psi_{\mathbf{k_2}}^{-*}(\mathbf{r_2})\,\nabla\,\Psi_2^{\rm sc}(\mathbf{r}_1, \mathbf{r}_2) \\ &-\Psi_2^{\rm sc}(\mathbf{r}_1, \mathbf{r}_2)\,\nabla\,\psi_{\mathbf{k_1}}^{-*}(\mathbf{r_1})\psi_{\mathbf{k_2}}^{-*}(\mathbf{r_2})\Big)\cdot d\mathbf{S} \end{aligned} \tag{7.7}$$

It must emphasized that the functions $\psi_{\mathbf{k_1}}^-(\mathbf{r_1})$ and $\psi_{\mathbf{k_2}}^-(\mathbf{r_2})$ do *not* describe the final state of the system, but are merely the testing functions that extract the necessary amplitude from $\Psi_2^{\rm sc}$. No *ansatz* has been made concerning the final state, and electron correlation is treated completely in the final outgoing wavefunction $\Psi_2^{\rm sc}$ as well as in the initial state Φ_0 in this approach.

But there is another problem that must be addressed before it is possible can proceed. For photon energies greater than the first ionization potential of the atom, $\Psi_1^{\rm sc}$, the solution of Eq. (7.3), will have single ionization terms that behave, at large *real* values of the electron coordinates, as the (symmetrized) product of a bound state of He^+ times an undamped outgoing wave in the other electron coordinate. This fact means that $\mu\Psi_1^{\rm sc}$, which is the driving term for Eq. (7.4), will not vanish as $r_1, r_2 \to \infty$ along the real axis. Since the dipole operator μ is a one-body operator, Eq. (7.4) will be

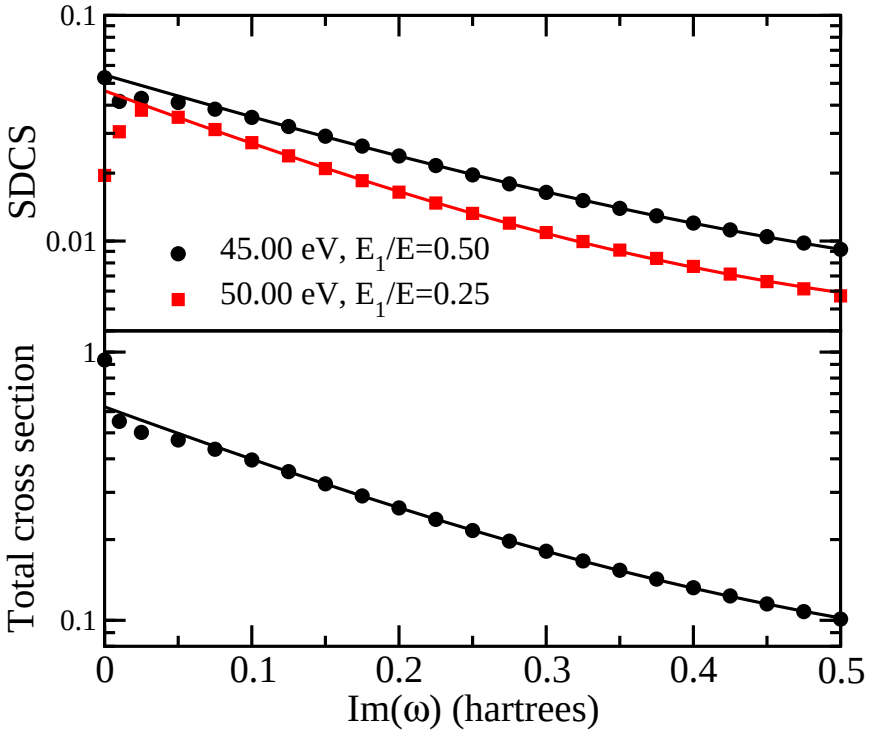

Figure 7.4: Upper: dependence of the SDCS at 45 and 50 eV and 25% and 50% energy sharing, respectively, on the imaginary part of ω used in solving Eq. (7.3). Lower: dependence of the total cross section at 45 eV photon energy on Im(ω). SDCS in units of 10^{-52} cm^4 sec eV^{-1}, total cross section in units of 10^{-52} cm^4 sec .

ill-conditioned, *irrespective of the gauge being used*, and the ionization amplitudes extracted from Ψ_2^{sc} will not converge with increasing volume. This problem can be can circumvented by adding a small, positive imaginary part to ω in Eq. (7.3) only, which will produce a solution Ψ_1^{sc} with an exponential fall-off for real r-values. With this procedure, a valid driving term for the solution of Eq. (7.4) is then calculated, which can then be solved directly under ECS for real ω. As explained in the theory section, and as demonstrated for the atomic hydrogen case, this procedure yields convergent amplitudes that can then be numerically extrapolated to purely real photon energies.

For the present calculations, partial waves up to l=4 to expand the initial state and up to l=5 in the intermediate and final states were used, including all product pairs allowed by symmetry. The coupled Dalgarno-Lewis equations were solved using the finite-element/discrete variable representation (FEM/DVR) method [97] . 15th order Gauss-Lobatto DVR with the first element boundary at 5.0 bohr and subsequent elements boundaries spaced 10.0 bohr apart were used. Calculations were performed with different real grids ranging from 85.0 to 255.0 bohr on a side; the complex portion of the grid was always 30.0 bohr in length. Singly differential cross section (SDCS), which is the quantity defined in Eq. (7.1) integrated over the angles Ω_1 and Ω_2, over a range of complex photon energies in Eq. (7.3) and extrapolated the results to real photon energies, i.e. to Im(ω)=0 were computed.

The SDCS is a relatively flat function of energy sharing for photon energies between 40 and 50 eV. In this energy range, SDCS over energy sharing can be integrated and then extrapolate the results to get the total cross section. The upper panel of Fig. 7.4 shows the dependence of the SDCS on Im(ω) at two different photon energies and energy sharings, while the lower panel shows the corresponding dependence for the total cross section at 45 eV. Above 51 eV, where the SDCS begins to rise at the extremes of energy sharing, i.e. near $E_1/E = 0.0$ and 1.0, a point-wise extrapolation of the SDCS is needed to compute total cross sections. Above 54.4 eV, which is the threshold for SI (sequential double ionization) (see Fig. 7.1), the SDCS has clearly defined peaks at $E_1 = \hbar\omega - 54.4$ eV and $E_1 = \hbar\omega - 24.6$ eV, as seen in Fig. 7.5. Before discussing these results, it is important to understand the origin of the peaks and their consequences for the extrapolations near the sequential ionization threshold.

The origin of the peaks in the SDCS can be understood using a simple model that ignores both correlation and screening in the final and intermediate states, following the logic of Proulx, Pont, and Shakeshaft [37]. Beginning with the exact spectral representation of the Green's function in

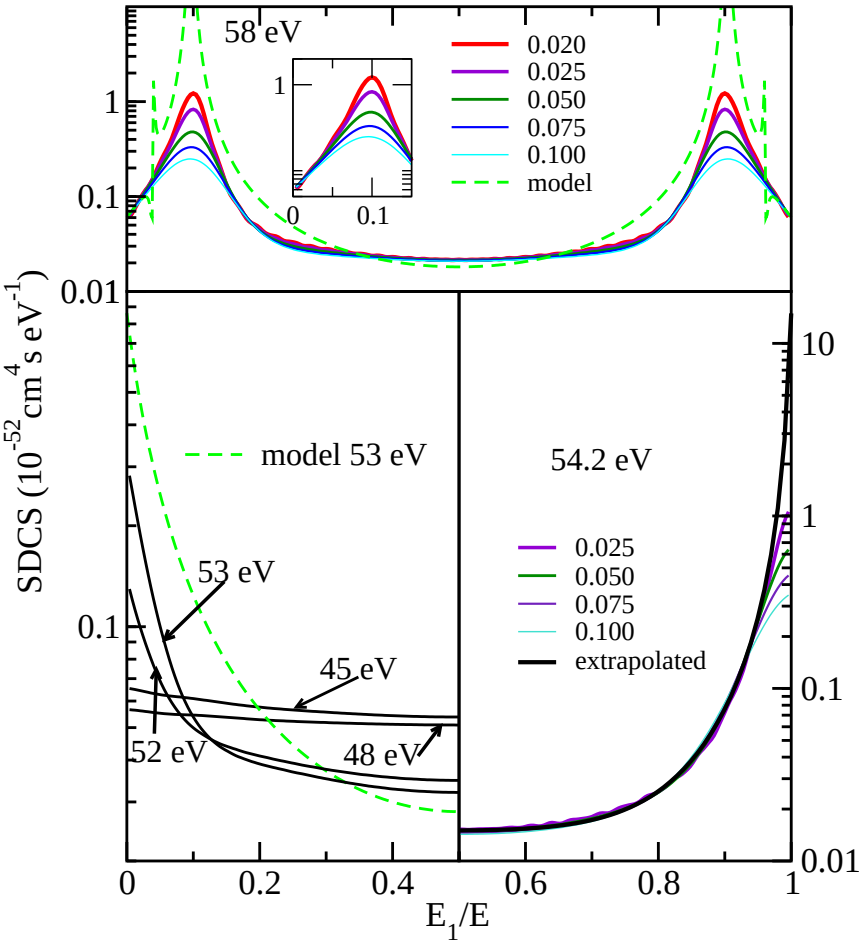

Figure 7.5: Upper: SDCS at 58 eV; solid curves labeled minimum Im(ω) used in extrapolating the data; dashed curve: results of the simplified model. Lower left: Extrapolated SDCS at energies below the SI threshold and the simplified model at 53 eV. Lower right: Extrapolation of SDCS at 54.2 eV with curves labeled by minimum Im(ω) used.

the definition of the amplitude in Eq.(7.2),

$$[E_0 + \hbar\omega - H + i\eta]^{-1} = \sum\!\!\!\!\!\!\int_v \frac{\langle \Psi^-_{\mathbf{k}_1,\mathbf{k}_2}|\mu|v\rangle\langle v|\mu|\Phi_0\rangle}{E_0 + \hbar\omega - E_v}\,. \tag{7.8}$$

Making first the approximation that the sum and integral over intermediate states $|v\rangle$ includes only the integral over the lowest singly ionized continuum $|\psi^-_{\mathbf{k},1s}\rangle$ of the helium atom. To approximate $\langle \Psi^-_{\mathbf{k}_1,\mathbf{k}_2}|\mu|\psi^-_{\mathbf{k},1s}\rangle$ screening and correlation in both the intermediate and properly symmetrized final states by using Coulomb functions with $Z = 2$ for all free electrons are ignored.

With these approximations a pair of momentum conserving delta functions pick out two terms in the integral over intermediate states that correspond to the sequential process. Ignoring the phases of $\langle \psi^-_{\mathbf{k},1s}|\mu|\Phi_0\rangle$ and $\langle \Psi^-_{\mathbf{k}_1,\mathbf{k}_2}|\mu|\psi^-_{\mathbf{k},1s}\rangle$, substituting the result into Eq. (7.1), and integrating over the ejection directions $d\Omega_1$ and $d\Omega_2$ allows us to write an approximate expression for the SDCS in terms of the single ionization cross sections of He and He^+,

$$\frac{d\sigma^{\rm seq}}{dE_1} \approx \frac{\hbar}{4\pi}\left(\frac{\sqrt{\sigma^{\rm He^+}(E_2)\sigma^{\rm He}(E_1)}}{E_0 + \hbar\omega - \epsilon_{1s} - E_1} + \frac{\sqrt{\sigma^{\rm He^+}(E_1)\sigma^{\rm He}(E_2)}}{E_0 + \hbar\omega - \epsilon_{1s} - E_2}\right)^2, \tag{7.9}$$

with $E_1 + E_2 = K^2/2$. In Eq. (7.9) $\sigma^{\rm He}(E)$ is the single ionization cross section of the neutral helium atom, and $\sigma^{\rm He^+}(E)$ is the single photoionization cross section of He^+ . The singularities in Eq. (7.9) corresponding to the SI process are separated in the SDCS by the difference between the ionization potential of He^+ and the first ionization potential of He. These singularities are believed to be a fundamental feature of LOPT and not the consequence of the simplifying approximations made in deriving Eq. (7.9).

The lower left panel of Fig. 7.5 shows the calculated SDCS, extrapolated to real ω, for several energies between 45 and 53 eV. Results from the simple model at 53 eV are also plotted for comparison. One sees that by 52 eV, the SDCS already begins to develop wings near extreme energy sharing, showing the signature of the sequential process whose energy threshold is at 54.4 eV. At 54.2 eV, as shown in the lower right panel of Fig. 7.5, the extrapolation scheme becomes unreliable at extreme energy sharing, where the SDCS shows a residual dependence on the smallest value of $\mathrm{Im}(\omega)$ used in the extrapolation. The final estimate of the SDCS shown in the figure was therefore obtained by extrapolating the calculated SDCS using a functional form that included singularities as in Eq. (7.9).

The upper panel of Fig. 7.5 shows results for calculations at 58 eV, along with the simple model prediction. The calculations show that the extrapo-

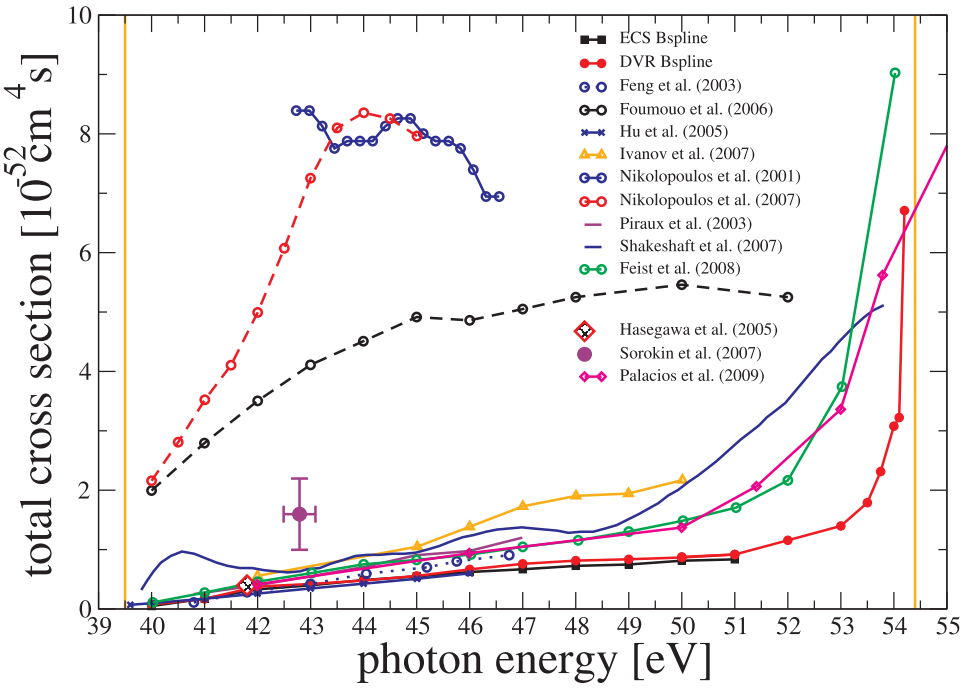

Figure 7.6: Calculated two-photon double ionization total cross sections compared with those of previous calculations. The vertical lines label the DI and SI thresholds.

lated peaks in the SCDS at energies corresponding to sequential ionization increase with decreasing Im(ω). These peaks would become singularities in the limit of an infinite size box. In the model results, there are sharp peaks outside the singularities which arise from the contribution of the first doubly excited (2s2p,^{1}P) state of He* in σ^{He}. It is worth noting that the *ab initio* SDCS data for 58 eV photon energy does show a slight asymmetry about the sequential peaks, with a modest broadening in the regions corresponding to excitation of doubly excited states (see Fig. 7.5 inset). One would expect post-collision interaction to significantly broaden such states, but whether these states are causing the asymmetry in the peaks is difficult to say.

Figure 7.6 shows the ECS calculated total cross sections, along with the results of earlier studies. The cross sections have been obtained : (i) by extrapolating the total cross section, as in Fig. 1b (open circles from 40 to 51 eV) and (ii) by extrapolating the SDCS as shown in the lower right panel of Fig. 3 and then integrating (solid squares from 50 to 54.4 eV), yielding identical results at 50 and 51 eV. At lower energies, where the results can be compared with the results of other calculations, the ECS calculated cross sections compare favorably with the results of several other methods, but are significantly smaller than the most recent studies published by Foumouo *et al.* [44] and by Nikolopoulos and Lambropoulos [48, 38]. The inflection in the total cross section at about 49 eV can be understood from the behavior of the SDCS in Fig. 7.5 as follows. As the non-sequential background portion of the SDCS begins to decrease, the contribution from the wings due to the energetically closed sequential process increases, and the total cross section begins again to increase.

In summary, accurate calculations of two-photon double ionization in lowest order perturbation theory for the helium atom have been carried out. Since these calculations treat electron correlation in the initial, virtual intermediate, and final states essentially exactly, these results show that the large degree by which previous theoretical calculations disagree is not due to the various levels at which correlation was previously treated. Rather it appears that the difficulty of numerically converging either accurate time-independent or time-dependent descriptions of this process is to blame. It has been that, below the threshold for the sequential process, the signature of SI is prominently revealed in the singly differential cross section, even at energies where it is less apparent in the total cross section. Above the threshold for sequential ionization, that process competes with non-sequential double ionization and both processes appear in lowest order perturbation theory. Although the singly differential cross sections is well defined at all energies, its apparently singular behavior at the sequential double ionization peaks means the *total* cross section is not well defined in lowest order perturbation theory above that threshold.

CHAPTER 8

Two-Photon Double ionization of H_2

Extracted from:
F. Morales, D. A. Horner, T. N. Rescigno, C. W. McCurdy and F. Martín. J. Phys. B. ***42*** *134013 (2009)*

As seen in the previous chapter, double ionization of the helium atom by two XUV photons has recently become the subject of intense theoretical interest (see, e.g. [37, 38, 39, 40, 41, 42, 43, 44, 45, 46, 47, 48, 49, 50, 51, 52, 53, 54]). This interest was first spurred by measurements with high harmonic generation sources in Japan [55] and, more recently, by experiments at the free-electron laser source (FLASH) in Hamburg [56, 57]. A general conclusion of these studies is that, in contrast to single-photon double ionization of Helium, the electrons have a preference to escape back to back, which can be easily recognized in the calculated triply differential cross sections [49, 50, 51] and/or in the measured and calculated recoil ion angular distributions [115].

There is, however, a question that has led to intense debate in the last few years [42, 43, 44, 45, 46, 47, 48, 49, 50, 51, 52, 53, 54], as could be checked in the previous chapter: the absolute value of the two-photon double ionization cross section. In spite of the fact that all these experiments have been performed in the intensity regime where second order perturbation theory is expected to be valid and, therefore, theory is easiest to apply, recent calculated cross sections differ by more than an order of magnitude [50]. Experimentally, an accurate determination of the two-photon double ionization cross sections of Helium is very difficult due to the smallness of such cross section. As a result, existing experimental values [55, 56, 116] are affected by error bars that are still too large to give a final answer to this question. Thus, the reasons for the strong disagreement among different theories are still far from being understood.

More recently, experiments under way at FLASH [58] have aimed at

studying two-photon double ionization of homonuclear diatomic molecules, in particular H_2. Although H_2 is more complicated than Helium and, consequently, similar discrepancies in the absolute value of the cross section may be expected, it is nevertheless interesting to investigate the new physical effects that arise from the use of a molecular potential (with cylindrical symmetry) instead of the atomic one (with spherical symmetry). In particular, one can expect to uncover the general trends that govern the two-electron escape by two-photon absorption in a molecular system. The simplest approach to the molecular problem consists in assuming the validity of the fixed-nuclei approximation, in which the positions of the two nuclei are fixed at their equilibrium internuclear distance $R_e = 1.4$ a.u.. This has been shown to be an excellent approximation in one-photon double ionization of H_2 ([65, 28]) because the two electrons are ejected almost instantaneously and, therefore, the nuclei do not have time to move during the ionization process. However, in the two-photon ionization case, some caution is necessary, since double electron escape can also occur through a sequential process in which one electron is first ejected after absorption of one photon and the second electron is later ejected after absorption of the other photon. If the time delay between the first and the second electron ejection is long enough to allow the nuclei to move (which is perfectly possible when, e.g., autoionizing states are active in the process -see e.g. [117, 101, 33]), any realistic description of the double ionization process must account for this nuclear motion. Fortunately, the sequential process is only possible for photon energies larger than 31 eV (this is the energy difference between the H_2^+ ground state and the H_2 double ionization continuum in the Franck-Condon region). Therefore, the fixed-nuclei approximation will be meaningful to study two-photon double ionization from the threshold up to 30 eV.

In a very recent communication, Colgan et al [59] have reported the first theoretical predictions of fully differential cross sections for two-photon double ionization of H_2 at 30 eV by solving the time-dependent Schrödinger equation. In this paper, the first accurate, time-independent calculations of this process using the exterior complex scaling method are presented, a method that has produced benchmark results for one- and two-photon double ionization of He [47, 50, 115] and one-photon double ionization of H_2 [50, 28, 65, 118]. This method provides grid-based, numerical solutions of the Schrödinger equation with no appeal to approximate asymptotic forms nor to ansatz wave functions. In order to compare with the predictions of reference [59], the the same photon energy has been considered, 30 eV, and molecular orientations parallel and perpendicular to the polarization vector. Although these methods have led to almost perfect agreement for the one-photon double ionization of H_2 [108], they disagree in the two-photon case. In particular, it is shown that, when the molecule is ionized parallel to the polarization vector, the electrons are almost exclusively ejected back

to back. This is similar to previous findings in Helium but it is somewhat in contradiction with the triply differential cross sections reported in [59]. A similar behavior is observed when the molecule is perpendicular to the polarization vector, which is in better agreement with the predictions of [59].

Atomic units are used throughout unless otherwise stated.

8.1 Methods

8.1.1 Exterior complex scaling treatment of molecular two-photon double ionization

The cross section for two-photon double ionization using lowest order perturbation theory (LOPT) in the velocity gauge, for a given internuclear distance, and differential in the electron energy sharing, and in the angular dependence of the ejected electrons is given by the expression:

$$\frac{d\sigma}{dE_1 d\Omega_1 d\Omega_2} = \frac{2\pi}{\hbar}\frac{(2\pi\alpha)^2}{m^2\omega^2} k_1 k_2 |f(\mathbf{k_1}, \mathbf{k_2}, \omega)|^2 \tag{8.1}$$

where $f(\mathbf{k_1}, \mathbf{k_2}, \omega)$ is the two-photon double ionization amplitude, $\mathbf{k_1}$ and $\mathbf{k_2}$ are the momenta of the photo-electrons, ω is the photon frequency, m is the electron mass and α is the fine-structure constant. The problem of obtaining the molecular double photo-ionization amplitude for the one-photon absorption case was correctly addressed in Ref.[65]. A straightforward generalization to the two-photon case allows us to write the corresponding amplitude as the following integral for a given internuclear distance:

$$f(\mathbf{k_1}, \mathbf{k_2}) = \langle \Phi^{(-)}(\mathbf{k}_1, \mathbf{r}_1)\Phi^{(-)}(\mathbf{k}_2, \mathbf{r}_2)|[E - T - v(r_1) - v(r_2)]|\Psi_2^{SC}(\mathbf{r_1}, \mathbf{r_2})\rangle \tag{8.2}$$

where E is the excess energy above the double ionization threshold, T is the two-electron kinetic energy operator and $v(\mathbf{r})$ is the nuclear attraction potential seen by one electron in the field of the bare nuclei. The functions $\Phi^{(-)}(\mathbf{k}, \mathbf{r})$ are H_2^+ continuum eigenfunctions with incoming momentum $\mathbf{k}$. The use of those eigenfunctions as testing functions to extract the amplitudes is extensively explained in both [65] and [63]. This choice of testing functions is optimal for these purposes because the orthogonality of the H_2^+ continuum eigenfunctions to the bound states of H_2^+ eliminates the contributions of the single ionization channels to 8.2. It must be emphasized that the product of testing functions is not the physical final-state, which is included in $\Psi_2^{SC}(\mathbf{r_1}, \mathbf{r_2})$. The latter wave function, which has purely outgoing boundary conditions for both electrons, is the solution of the coupled driven Schrödinger equations, in the Dalgarno-Lewis form of second-order perturbation theory that describe the absorption of two photons by a system

initially in a state Φ_0:

$$(E_0 + \hbar\omega - H)|\Psi_1^{SC}(\mathbf{r_1}, \mathbf{r_2})\rangle = \boldsymbol{\epsilon}\cdot(\nabla_\mathbf{1} + \nabla_\mathbf{2})|\Phi_0\rangle \tag{8.3}$$

$$(E_0 + 2\hbar\omega - H)|\Psi_2^{SC}(\mathbf{r_1}, \mathbf{r_2})\rangle = \boldsymbol{\epsilon}\cdot(\nabla_\mathbf{1} + \nabla_\mathbf{2})|\Psi_1^{SC}\rangle \tag{8.4}$$

where ϵ is the polarization unit vector, ∇_1 and ∇_2 are the gradient operators for the electronic coordinates, and $|\Phi_0\rangle$ is the initial bound state of H_2. Notice that the velocity form of the dipole operator has been used. These two driven equations must be solved with the proper outgoing wave scattering boundary conditions. These conditions are imposed rigorously, as described in previous publications on this method [96], by transforming the radial coordinates of both electrons according to the exterior complex scaling (ECS) transformation. This transformation scales those coordinates by a complex factor, $\exp(i\eta)$ beyond some radius R_0:

$$r \to \begin{cases} r & \text{for} \quad r \le R_0 \\ R_0 + (r - R_0)e^{i\eta} & \text{for} \quad r > R_0 \end{cases} \tag{8.5}$$

For photon energies below the first ionization potential of H_2, applying the ECS transformation to the electronic radial coordinates in Eq. (8.3) and (8.4) causes the purely outgoing solutions $\Psi_1^{SC}(\mathbf{r_1}, \mathbf{r_2})$ and $\Psi_2^{SC}(\mathbf{r_1}, \mathbf{r_2})$ to decay exponentially for any $r_i > R_0$, regardless of the number of electrons in the continuum. Thus choosing R_0 large enough, this method allows $\Psi_1^{SC}(\mathbf{r_1}, \mathbf{r_2})$ and $\Psi_2^{SC}(\mathbf{r_1}, \mathbf{r_2})$ to reach its correct outgoing asymptotic form where the $\mathbf{r_1}$ and $\mathbf{r_2}$ coordinates are real valued. In other words, the ECS transformation provides us with the physical wave function in the region where both coordinates are less than R_0. In an exact or converged calculation the solutions of the Schrödinger equation for $r < R_0$ do not depend on η or R_0.

In the present application of the ECS transformation difficulty specific to the application of the ECS approach to two-photon double ionization must be addressed, which, as pointed out in the previous sections and on earlier studies on He [47, 115, 50], does not appear in the case of one-photon double ionization. For photon energies above the first ionization potential of H_2, the solution of 8.3, $\Psi_1^{SC}(\mathbf{r_1}, \mathbf{r_2})$, will have single-ionization terms that behave, at large *real* values of the electron coordinates, as the product of a bound state of H_2^+ times an undamped outgoing wave in the other electron coordinate. This means that $\epsilon\cdot(\nabla_\mathbf{1} + \nabla_\mathbf{2})\Psi_1^{SC}$, which is the initial term for 8.4, will not vanish as $\mathbf{r_1}$ or $\mathbf{r_2} \to \infty$ along the real axis. Because the dipole operator is a one-body operator, the application of outgoing boundary conditions via the ECS transformation in 8.4 will depend on the value of R_0, irrespective of the gauge being used, and the amplitudes extracted from $\Psi_2^{SC}(\mathbf{r_1}, \mathbf{r_2})$ will

not converge with increasing volume of the space on which it is solved. To avoid this problem a small, positive, imaginary part to ω in Eq. 8.3 only is added. This will produce a solution $\Psi_1^{SC}(\mathbf{r_1}, \mathbf{r_2})$ with an exponential falloff for the real r values. In this way, $\Psi_1^{SC}(\mathbf{r_1}, \mathbf{r_2})$ will be a valid driving term for 8.4. However, this procedure yields different amplitudes for different complex values of ω in the first equation. Thus 8.3 and 8.4 must be repeatedly solved for different values of the imaginary part of ω and then numerically extrapolated to a purely real photon energy.

As indicated above, all calculations have been carried out at the equilibrium internuclear distance $R_e = 1.4$ a.u., unless otherwise stated.

8.1.2 Numerical implementation

In these calculations numerical procedures similar to those used for one-photon double ionization of H_2 ([65, 28, 63]) have been used, in which the full scattered wave is decomposed into angular components on a radial grid in order to implement exterior complex scaling. The scattered wave functions $\Psi_1^{SC}(\mathbf{r_1}, \mathbf{r_2})$ and $\Psi_2^{SC}(\mathbf{r_1}, \mathbf{r_2})$ that solve equations 8.3 and 8.4, respectively, for a fixed value of the projection M of the electronic angular momentum along the molecular axis and for singlet spin coupling, are expanded as a sum of products of two-dimensional radial wave functions and spherical harmonics:

$$\Psi^{SC,(M)}(\mathbf{r_1}, \mathbf{r_2}) = \sum_{\mu_1\mu_2, j_1 \geq j_2} \left(\frac{\psi^{dir}_{j_1,\mu_1,j_2,\mu_2}(r_1,r_2)}{r_1 r_2} Y_{j_1\mu_1}(\hat{\mathbf{r}}_\mathbf{1}) Y_{j_2\mu_2}(\hat{\mathbf{r}}_\mathbf{2}) + \frac{\psi^{exch}_{j_1,\mu_1,j_2,\mu_2}(r_1,r_2)}{r_1 r_2} Y_{j_2\mu_2}(\hat{\mathbf{r}}_\mathbf{1}) Y_{j_1\mu_1}(\hat{\mathbf{r}}_\mathbf{2}) \right) \tag{8.6}$$

where the indexes 1 or 2 from Ψ^{SC} have been removed and the value of M has been explicitly written. The radial functions $\psi^{dir}_{j_1,\mu_1,j_2,\mu_2}$ and $\psi^{exch}_{j_1,\mu_1,j_2,\mu_2}$ are expanded in products of discrete variable representation (DVR) basis functions, so that the Hamiltonian matrix elements corresponding to the left hand sides of 8.3 and 8.4 are the same as those in a "complete configuration interaction" calculation in that basis.

In this work, two possible orientations of the molecule will be considered with respect to the polarization vector: parallel and perpendicular. In the first case, $\Delta M = 0$ and the two photon transition is given by the following sequence of molecular symmetries (notice that ${}^1\Sigma_g^+$ is the symmetry of the ground state of H_2):

$${}^1\Sigma_g^+ \rightarrow^1 \Sigma_u^+ \rightarrow^1 \Sigma_g^+ \tag{8.7}$$

The corresponding amplitude can be written as:

$$f^{||}(\mathbf{k_1}, \mathbf{k_2}, \omega) = f_{{}^1\Sigma_g^+ \rightarrow {}^1\Sigma_u^+ \rightarrow {}^1\Sigma_g^+} \tag{8.8}$$

In the perpendicular case, $\Delta M = \pm 1$ and the possible transitions are:

$$\begin{aligned} {}^1\Sigma_g^+ &\rightarrow \Pi_u \rightarrow \Delta_g \\ {}^1\Sigma_g^+ &\rightarrow \Pi_u \rightarrow \Sigma_g^+ \end{aligned} \tag{8.9}$$

The corresponding amplitude is the coherent superposition of these two paths:

$$f^{\perp}(\mathbf{k_1}, \mathbf{k_2}, \omega) = f_{^1\Sigma_g^+ \rightarrow \Pi_u \rightarrow \Delta_g} + f_{^1\Sigma_g^+ \rightarrow \Pi_u \rightarrow \Sigma_g^+}. \tag{8.10}$$

When the molecular axis is not aligned either perpendicular or parallel to the polarization vector, there is a more complicated combination of amplitudes. The analysis of these orientations will be postponed to future work.

8.1.3 Test for two-photon single ionization

To check that this implementation of the ECS method for the two-photon molecular problem is correct, the two-photon single ionization cross section of H_2 oriented parallel to the polarization vector has been evaluated. For this particular orientation there are previous results with which to compare [119, 120]. In this problem, the photon energy is smaller than the H_2 ionization potential and, consequently, there is no need to use a complex photon energy to solve the first driven equation (the second photon absorption connects a truly exponentially decreasing state with the final state). Figure 8.1 shows a comparison between these results and those previously reported in [119, 120]. The agreement is very good, especially with the more recent results of Palacios [120]. The observed peaks are associated with resonance enhanced multiphoton ionization (REMPI) that involves the ${}^1\Sigma_u^+$ bound states of H_2. It is important to emphasize here that these peaks are significantly broadened and enhanced when the vibrational motion is included [121]. This is due to the fact that, in REMPI, the nuclei have enough time to move during the ionization process and, consequently, Chase's approximation is no longer valid. In any case, this does not invalidate the comparison shown in Figure 8.1 since the only purpose is to show that the present implementation of the ECS method is correct.

8.1.4 Test of the $\mathbf{Im}[\omega] \rightarrow 0$ extrapolation

As mentioned above, in two-photon double ionization of H_2, $\Psi_1^{SC,(M)}$ must be evaluated for different values of the imaginary part of ω, $\mathrm{Im}[\omega]$. This leads to transition amplitudes that depend on $\mathrm{Im}[\omega]$ and, therefore, must be extrapolated to $\mathrm{Im}[\omega] = 0$. Different extrapolation methods have been thoroughly tested, including linear, exponential, and polynomial extrapolations, in order to find which one leads to the best fit of the amplitudes and to the most stable extrapolated value. The chosen method is a fourth-order polynomial extrapolation method that includes all calculated amplitudes down

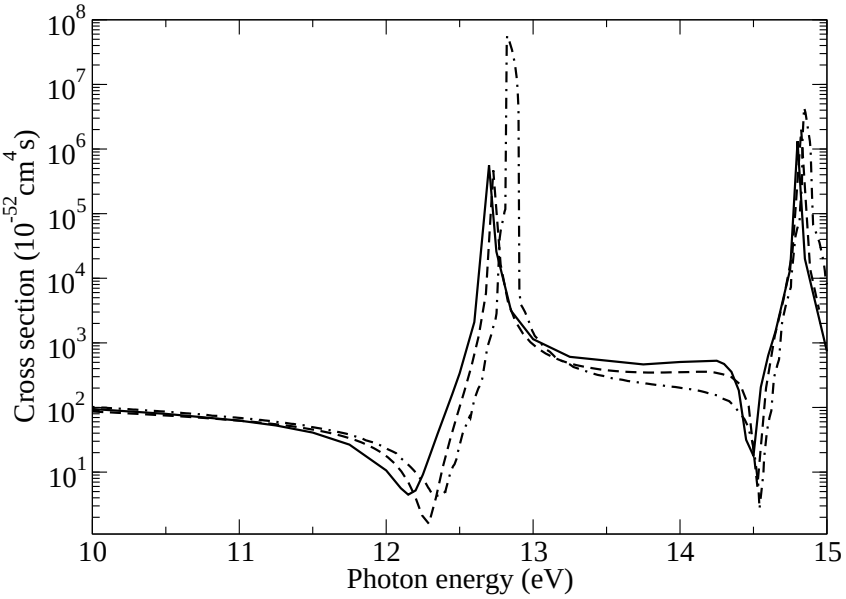

Figure 8.1: Two-photon single ionization cross sections of H_2 oriented parallel to the polarization vector. Full curve: present results obtained with a DVR basis with grid points placed at $\{0, 5, 15, 25, 35, 45, 55, 70\}$ a.u. and angular momentum up to 7 (176 angular configurations). Dashed line: Palacios [120]. Dashed-dotted line: Apalategui et al [119].

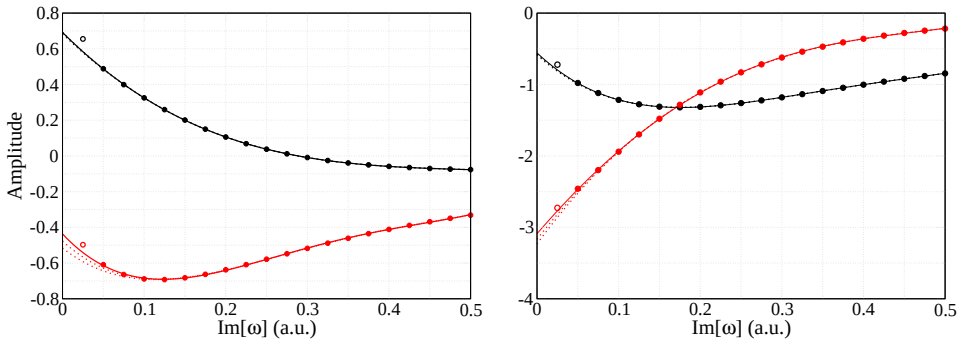

Figure 8.2: Examples of the extrapolation of the amplitudes to $\mathrm{Im}[\omega] = 0$ in atomic units. Solid line: fourth order polynomial fit of the amplitudes, including all points up to $\mathrm{Im}[\omega] = 0.05$, for a photon of 30 eV. Dashed lines, same as solid line, but including points up to $\mathrm{Im}[\omega] = 0.025$, 0.075, and 0.1. Left panel:$(l_1, l_2, j_1, m_1, j_2, m_2)$=$(1, 1, 1, 0, 1, 0)$ Σ_g^+ amplitude; left panel: $(1, 1, 1, -1, 1, -1)$ Δ_g amplitude.

to $\mathrm{Im}[\omega] = 0.05$. The choice of the lowest value of $\mathrm{Im}[\omega]$ that one can include in the fit depends on R_0. Indeed, there is always a small interval Δ in the vicinity of $\mathrm{Im}[\omega] = 0$ where the calculated amplitudes are meaningless. In this interval, the amplitudes deviate rapidly from their smooth behavior in the rest of the complex plane from which one is extrapolating and, therefore, such amplitudes must be excluded from the fit. In general, the larger R_0 the smaller the interval Δ in which the amplitudes are meaningless. Strictly speaking, the physical limit $\mathrm{Im}[\omega] = 0$ is reached for $R_0 = \infty$. Since, in actual calculations, R_0 must remain finite, a practical way of reaching this limit is to choose a large enough value of R_0 and then extrapolate to $\mathrm{Im}[\omega] = 0$ the amplitudes calculated for $\mathrm{Im}[\omega]$ values lying outside Δ. The latter interval can be defined by comparing amplitudes obtained with different values of R_0. More specifically, Δ is given by the region of $\mathrm{Im}[\omega]$ values in which the amplitudes vary significantly with R_0. These amplitudes are not included in the fit. In contrast, amplitudes that remain stable when R_0 is varied lie outside the Δ interval and, therefore, are included in the fit.

Figure 8.2 illustrates the performance of the fourth-order polynomial extrapolation for two characteristic amplitudes: the dominant ones leading to $^1\Sigma_g^+$ and $^1\Delta_g$ final symmetries. It can be seen that the extrapolation value is very stable with respect to the smallest value of $\mathrm{Im}[\omega]$ included in the fit. A similar stability for other amplitudes and for the calculated cross sections has been found(see Figure 8.3). Hence, in practice, the extrapolation is performed automatically by imposing that all amplitudes calculated in the interval $0.05 \leq \mathrm{Im}[\omega] \leq 0.5$ are included in the fit to the fourth-order poly-

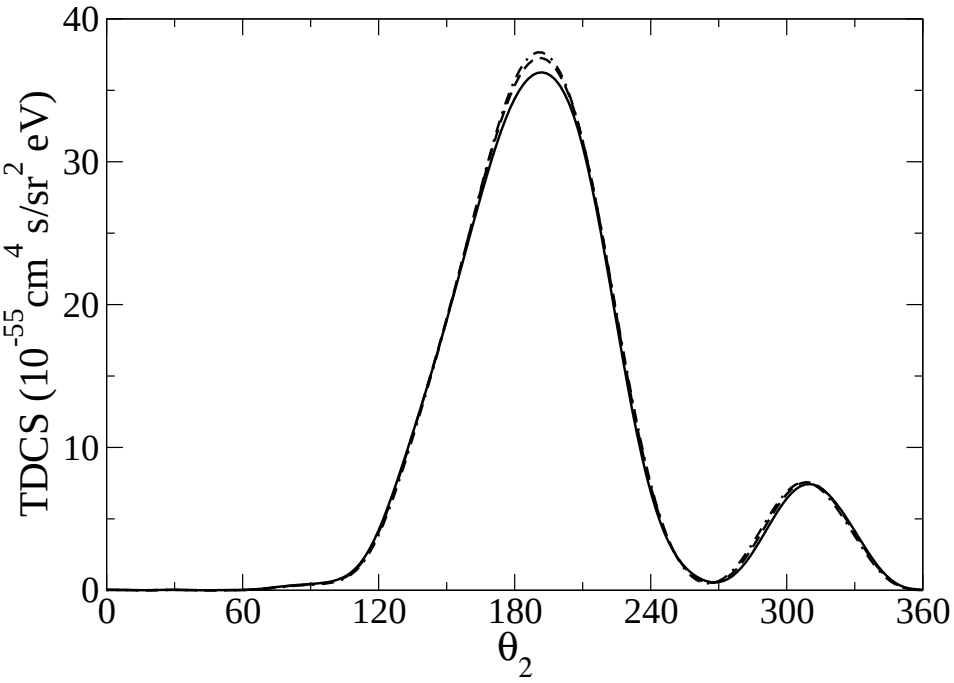

Figure 8.3: TDCS for a photon energy of 30 eV, the molecule oriented perpendicular to the polarization vector, and an angle for the fixed electron of 30 degrees. Grid points set at {0, 5, 10, 20, 30, 40, 50, 60, 70, 80, 90, 100, 110, 120, 130, 140, 150, 170} atomic units. Angular momentum up to 7 (161 angular configurations for Δ_g states, and 176 for the Σ_g^+ states). Solid line: including all points up to Im[ω] = 0.05. Dashed line: including all points up to Im[ω] 0.075. Dashed-dotted line: including all points up to Im[ω] up to 0.1.

nomial. For Im[ω] $\geq$ 0.5, the amplitudes shown in the figure are practically identical to those obtained with a larger value of R_0, which is an additional proof of the validity of the present procedure to obtain the physical limit Im[ω] = 0.

Basis set convergence

Calculations with different box sizes have been performed, different DVR grids and different values of angular momentum. As it can be seen in Figure 8.4, at a photon energy of 30 eV, convergence is reached for l_{max} = 8, a box size of 170 a.u. (R_0 = 140 a.u.), and a DVR grid 0, 5, 10, 20, 30, 40, 50, 60, 70, 80, 90, 100, 110, 120, 130, 140, 150, 170 a.u.. Results obtained with l_{max} = 7 and/or slightly smaller boxes and/or slightly less dense DVR grids are very similar. It also has been checked that results obtained with

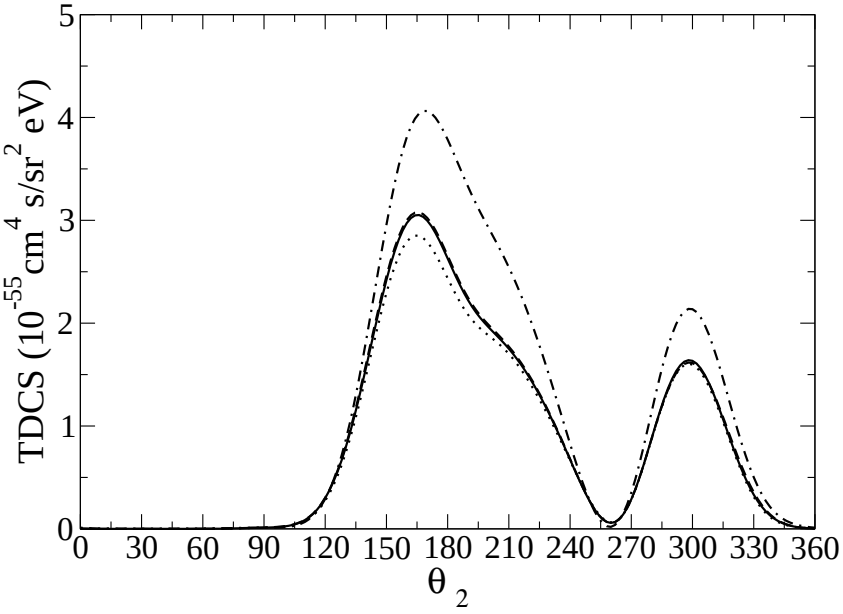

Figure 8.4: TDCS for a photon of 30 eV, Im[ω] = 0.05, and a fixed electron angle of 30 degrees, for H_2 parallel to the polarization vector. Solid: DVR grid in a.u. {0, 5, 10, 20, 30, 40, 50, 60, 70, 80, 90, 100, 110, 120, 130, 140, 150, 170}, $R_0 = 140 a.u.$, $l_{max} = 8$. Dashed: Same grid as before but with $l_{max} = 7$. Dotted: DVR grid in a.u. {0, 5, 10, 20, 30, 40, 50, 60, 70, 80, 90, 100, 110, 120, 130}, $R_0 = 110 a.u.$, $l_{max} = 7$. Dash-dotted: DVR grid in a.u. {0, 5, 10, 20, 31.25, 42.5, 54.75, 66, 77.25, 88.5, 99.75, 110, 120, 130}, $R_0 = 110 a.u.$, $l_{max} = 7$.

different angles of the complex rotation are indistinguishable in the scale of the figure. All results reported below have been obtained by using the largest basis set.

United atom limit

Calculations for two-photon double ionization of H_2 by using a value of the internuclear distance of 0.1 a.u. have been performed. In this case, the fully differential cross sections for parallel and perpendicular orientations must be almost identical and very similar to the corresponding Helium ones for the same excess photon energy. Figure 8.5 shows the calculated cross sections for an excess photon energy of 42 eV for the parallel and perpendicular cases. At 42 eV, only direct (non sequential) ionization is possible in both Helium and the artificially compressed H_2 molecule with $R = 0.1$ a.u.. As can be seen, for all ejection directions of the fixed electron, the results for both orientations are indeed very close to each other. The success of this test proves that coherence between the different amplitudes calculated with the ECS H_2 code is correctly described. The figure also includes the He results previously reported in references [42, 50, 54, 122] for the same excess photon energy and the same angles of the fixed electron. The cross sections calculated with $R = 0.1$ a.u. agree qualitatively with the Helium ones reported in references [50, 54, 122] at $\theta_1 = 0$ and 30°; the agreement deteriorates at $\theta_1 = 60$ and 90° because the corresponding cross sections are substantially smaller. The cross sections reported in [42] are systematically lower than those reported in [50, 54, 122]. In assessing the quality of the present results one must take into account the fact that it these calculations are not using exactly $R = 0$ in the molecular calculations (the reason for not doing it is that it would be a source of numerical errors in the molecular code) and that the differences among the three Helium calculations that better agree in magnitude are of the order of those between the latter and the present calculations. Extrapolating the conclusions of this analysis to the true molecular case ($R = 1.4$ a.u.) suggests that the error of the cross sections presented in the following sections should not be larger than 30%.

8.2 Results and discussion

The calculated triply differential cross sections for two-photon double ionization are given in Figs. 8.6 and 8.7 for molecules oriented, respectively, parallel and perpendicular to the polarization vector. All the results correspond to equal energy sharing between the electrons. The TDCS are plotted in the plane formed by the molecular axis, the polarization vector and the direction of ejection of the fixed electron. In the top left panel of Figure 8.6, the molecular axis, the polarization direction and the direction of the fixed electron coincide at 0°. In the three remaining panels of Fig. 8.6, the direction

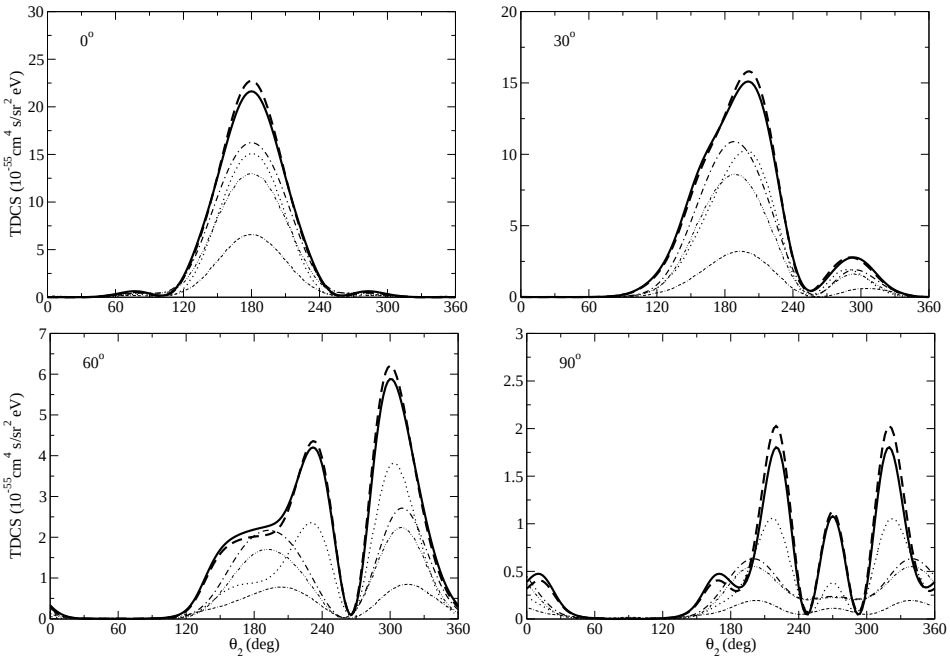

Figure 8.5: TDCS of He and H_2 oriented parallel and perpendicular to the polarization direction for an excess photon energy of 42 eV, equal energy sharing and emission angles of the fixed electron 0, 30, 60 and 90°. The TDCS is shown in the plane that contains the direction of the fixed electron and the polarization vector. The H_2 internuclear distance is $R = 0.1$. Amplitudes where extrapolated using the same procedure as described above. The basis details are the same as those given in figure (8.3). Thick solid line: H_2 parallel. Thick dashed line: H_2 perpendicular. Dotted line: He results from [50]. Dashed-dotted lines: He results from [122]. Dashed-double dotted lines: He results from [54]. Dotted-double dashed lines: He results from [42].

of the fixed electron is rotated $\theta_1 = 30$, 60 and 90°, respectively, with respect to the the polarization vector (and the molecular axis). In the top left panel of Figure 8.7, the polarization vector and the direction of the fixed electron coincide, and the molecular axis is perpendicular to them. In the other three panels, the direction of the fixed electron is rotated by $\theta_1 = 30$, 60 and 90° with respect to the the polarization vector. Notice that, in both figures, the TCDS is largest for $\theta_1 = 0°$ and then decreases with θ_1. The TDCS for $\theta_1 = 90°$ is roughly an order of magnitude smaller than that for $\theta_1 = 0°$ in the parallel case (figure 8.6) and two orders of magnitude smaller than that for $\theta_1 = 0°$ in the perpendicular case (figure 8.7). For $\theta_1 = 0°$, the second electron preferentially escapes at 180°, i.e., in a direction opposite to that of the first electron. This is similar to what has been found in two-photon

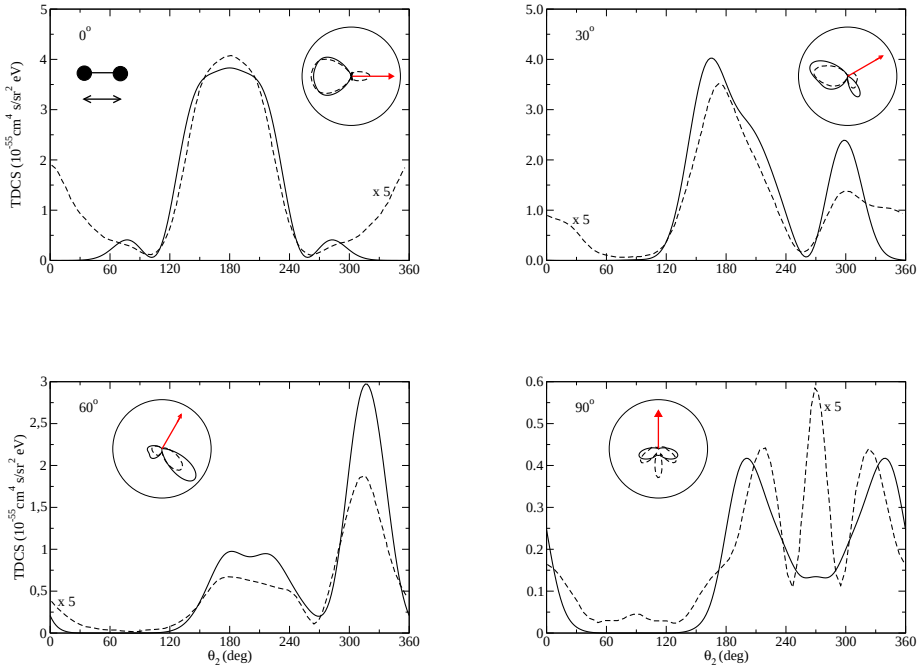

Figure 8.6: TDCS for a photon energy of 30 eV with the molecule oriented parallel to the polarization axis. Each panel displays a different orientation of the fixed electron. Solid: ECS calculations using a DVR grid in a.u. {0, 5, 10, 20, 30, 40, 50, 60, 70, 80, 90, 100, 110, 120, 130, 140, 150, 170}, $R_0 = 140 a.u.$, $l_{max} = 8$. Dashed: Results from [59] multiplied by 5. The insets show polar plots of the corresponding TDCSs. In those insets, the ejection direction of the fixed electron is indicated by an arrow.

double ionization of Helium [49, 50, 51]. In contrast, as θ_1 increases, there is less and less tendency of the electrons to escape in opposite directions. Also, the difference between the parallel and the perpendicular orientations become more apparent. Both effects are the consequence of molecular effects not present in Helium.

The present results are compared with those previously obtained by Colgan et al [59]. In the parallel case, the calculated TDCSs are approximately a factor of five larger than those reported in [59]. In the perpendicular case, the magnitudes are more similar. There are also important differences in the shapes of the TDCSs. For all the TDCSs plotted in Figs. 8.6 and 8.7, there is an effective node in the cross section when $\theta_1 = \theta_2$, i.e., zero probability for the second electron to escape in the same direction as the first electron

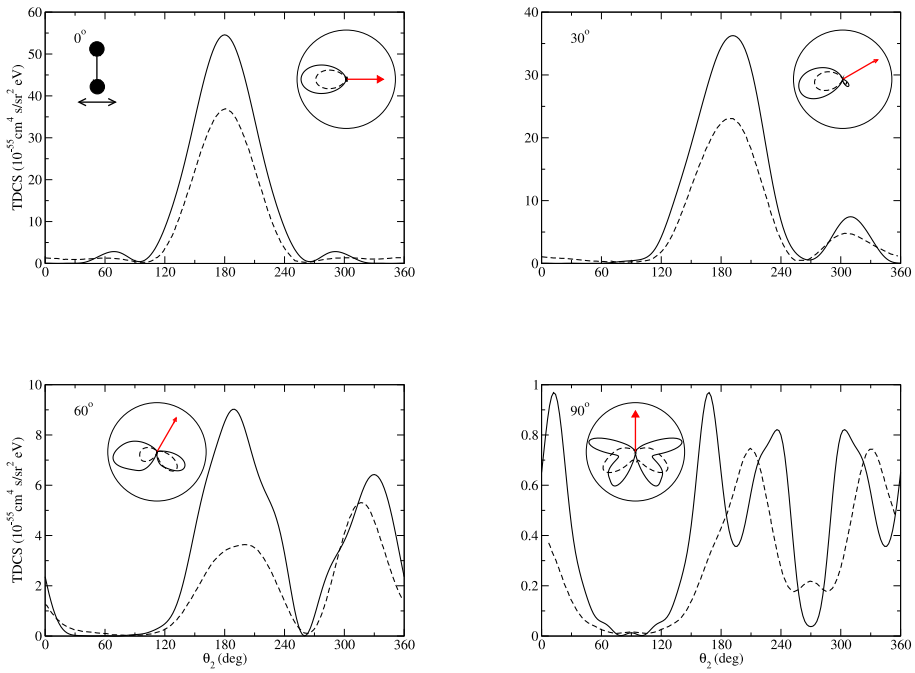

Figure 8.7: TDCS for a photon energy of 30 eV with the molecule oriented perpendicular to the polarization axis. Each panel displays a different orientation of the fixed electron. Solid: ECS calculations using a DVR grid in a.u. $\{0, 5, 10, 20, 30, 40, 50, 60, 70, 80, 90, 100, 110, 120, 130, 140, 150, 170\}$, $R_0 = 140 a.u.$, $l_{max} = 8$. Dashed: Results from [59]. The insets show polar plots of the corresponding TDCSs. In those insets, the ejection direction of the fixed electron is indicated by an arrow.

are predicted. (Bear in mind that these TDCS are for equal energy sharing.) This is not the case in the TDCS reported by Colgan et al [59], especially for the parallel orientation at $\theta_1 = \theta_2 = 0°$, where they predict that the probability for both electrons to escape in the same direction is about 50% of the probability to escape in opposite directions. This result is striking because, in Helium, all existing calculations report an effective node that prevents both electrons from escaping in the same direction when they have the same energy (see figure 8.5 and references [42, 50, 54, 122]). Physical intuition suggests that this should be also the case in two-photon double ionization of H_2 because Coulomb repulsion demands this to be so. In general, the discrepancies are largest for the smallest cross sections, especially for those obtained at 90°. Interestingly, the TDCSs reported by Colgan et al are more helium-like than ours: theirs are more similar to the Helium TDCSs

and they do not differ significantly in the parallel and perpendicular orientations. For instance, for $\theta_1 = 60^\circ$, they find the same relative magnitude of the two main peaks in the parallel and the perpendicular orientations, while opposite relative magnitudes in each orientation are found. While it is very difficult to know the reason why molecular effects are stronger in the present results, all consistency tests reported in the previous section suggest that this cannot be due to a lack of convergence. It is also worth pointing out that Helium results obtained by using the same method as that of Colgan et al (see results from reference [42] in figure 8.5) also differ significantly from those obtained by us and other authors. Whether or not this is due to deficiencies in the treatment of electron correlation in the final state remains an open question.

Conclusions and future work

During the time the thesis work, several conclusions have been reached, as well as some important developments have been achieved. Summarizing, the major conclusions and achievements are:

- The existing photoionization ECS methodology was extended, through a series of ordered steps, for the two photon ionization problems. The first step was to understand completely the formalism, including the physical meaning of the exterior complex scaling, the extraction of the amplitudes as well as understanding the different cross sections that could be calculated for a photo ionization process. An important part of this was also the computational realization, as both the eigenvalue solver and the linear equation solver had to be implemented in parallel, using distributed memory techniques. The knowledge acquired throughout these years, in different areas of physics and computer sciences, has allowed me to develop efficient programs, not only for the methodology here shown, but also for other time dependent problems. This is work in progress, and, for this reason, it has not been described in this manuscript (see list of publications at the end of this thesis).

- While solving for the atomic hydrogen two photon ionization, we gained valuable knowledge about convergence of intermediate continuum state wave functions. The acceleration gauge has also been tested (although it has not been used for the course of publications for this thesis), as a valid gauge to use for this particular problem. However, it becomes useless in the case of the two-photon double ionization, and was therefore discarded.

- Using the methodology presented therein, we were able to obtain converged results for the two-photon double ionization of He. The correct values for the total cross-section are still a challenge for both, theory

and experiments. We hope that the experiments that are being carried out will finally shed some light onto this fundamental problem.

- We obtained one of the first converged results for the two-photon double ionization of H_2. Experiments on this system will be performed soon, however, several theoretical challenges remain to be solved:
  - The calculation of the two-photon double ionization amplitudes for randomly oriented molecules with respect to the polarization axis.
  - The computation of integral cross sections.
  - Investigating the effects of varying the internuclear distance in the fully differential cross-sections.
  - Extension of the methodology to include nuclear motion quantum mechanically.
  - The search for interference effects such as those encountered for the one-photon double ionization.
- Our results for high energy photons in the single-photon double ionization were a real computational test for this method. They helped to better understand the experimental results [35] and to focus on the proper parameters such as laser polarization and photon energy (in the appearance of the observed interference pattern).

Conclusiones y trabajo futuro

Durante el tiempo de la realización de esta tesis, se han llegado a varias conclusiones, además del desarrollo del método llevado a cabo. La lista de conclusiones y logros podría resumirse así

- La metodología ECS existente se ha extendido, siguiendo una serie de pasos ordenados, para tratar problemas de doble ionización mediante dos fotones. El primer paso fue comprender completamente el formalismo, incluyendo el significado físico de lo que supone la escala exterior compleja (ECS), la extracción de las amplitudes, así como entender las diferentes secciones eficaces que podían ser calculadas para un proceso de fotoionización. Esta serie de pasos también llevó asociada una importante carga computacional, puesto que tanto para resolver el sistema de autovalores, como para resolver el sistema de ecuaciones lineales ha hecho falta implementar un código paralelo, usando técnicas de memoria distribuida. Todo este conocimiento, tanto físico como computacional, adquirido durante estos años, me ha permitido desarrollar programas eficientes, ya no sólo para este problema en concreto, sino también para problemas dependientes del tiempo. Esta parte del trabajo, puesto que todavía está en marcha, no ha sido descrita en este manuscrito (ver lista de publicaciones al final de esta tesis).

- Resolviendo el problema de la ionización mediante dos fotones del átomo de hidrógeno, aprendimos mucho sobre cómo converger los estados del continuo usados como estados intermedios para el formalismo ECS. Se probó el uso del gauge de aceleración, que, aunque no está comentado en esta tesis, demostró ser un gauge válido para este problema. Pero, para problemas de doble ionización mediante dos fotones se descartó, puesto que presentaba problemas de convergencia.

- Usando esta metodología, fuimos capaces de obtener resultados convergidos para el problema de la doble ionización mediante dos fotones del helio. El valor actual de la sección eficaz total es todavía un problema para el cual no se conoce la respuesta. Esperamos que los experimentos que actualmente se están llevando a cabo arrojen luz sobre esta cuestión.

- Hemos obtenido uno de los primeros resultados convergidos para el problema de la doble ionización del H_2 mediante dos fotones. Los experimentos para esta cuestión serán llevados a cabo en un futuro próximo, pero, mientras, este problema ofrece muchas cosas sobre las que trabajar desde el punto de vista teórico, como puede ser:

  - Cálculo de las amplitudes de doble ionización mediante dos fotones para cualquier orientación de la molécula respecto al vector de polarización.
  - Calcular secciones eficaces totales.
  - Investigar los efectos puramente moleculares en la sección triplemente diferencial, variando la distancia internuclear.
  - Extender la metodología para incluir el movimiento nuclear.
  - Búsqueda de efectos de interferencia, como los encontrados para la doble ionización mediante un fotón.

- Los resultados para la doble ionización mediante un fotón de alta energía en el H_2 supusieron un verdadero reto computacional, puesto que han requerido el uso de funciones bases de tamaño jamás usado para este tipo de problemas. También ayudó a comprender mejor los resultados del experimento [35], a la vez que aporta la dirección que este tipo de experimentos debe llevar para obtener el tipo de conclusiones que originalmente estaban buscando.

Publications

This thesis work has resulted in the following scientific publications and journal submissions:

- *Validity of the isolated resonance picture for H_2 autoionizing states*, F. Morales, C. W. McCurdy and F. Martín. Phys. Rev. A **73**, 014702 (2006)

- *Two photon double ionization of helium above and below the threshold for sequential ionization*, D. A. Horner, F. Morales, T. N. Rescigno, F. Martín and C. W. McCurdy. Phys. Rev. A. **76**, 030701 (2007)

- *Classical Two Slit Interference Effects in Double Photoionization of Molecular Hydrogen at High Energies*, D. A. Horner, S. Miyabe, T. N. Rescigno, C. W. McCurdy, F. Morales and F. Martín. Phys. Rev. Lett. **101**, 183002 (2008)

- *Two photon double ionization of H_2 at 30eV using Exterior Complex Scaling*, F. Morales, D. A. Horner, T. N. Rescigno, C. W. McCurdy and F. Martín. J. Phys. B. **42** 134013 (2009)

- *Asymmetric electron angular distributions in resonant dissociative photoionization of H_2 with ultrashort XUV pulses*, J. F. Pérez Torres, F. Morales, J. L. Sanz-Vicario and F. Martín. Phys. Rev. A **80**, 011402 (2009)

- *Probing H_2 autoionization quantum dynamics with XUV atto and femtosecond laser pulses*, F. Morales, J. F. Perez Torres, J. L. Sanz-Vicario and F. Martin. Chem. Phys. accepted (2009).

- *Electron Localization following Attosecond Molecular Photoionization*, G. Sansone, F. Kelkensberg, J. F. Pérez Torres, F. Morales, M. F. Kling, W. Siu, O. Ghafur, P. Johnsson, M. Swoboda, E. Benedetti, F.

Ferrari, F. Lépine, J. L. Sanz-Vicario, S. Zherebtsov, I. Znakovskaya, A. L'Huillier, M. Yu. Ivanov, M. Nisoli, F. Martín, M. J. J. Vrakking. Submitted to Nature

- *Probing H_2 autoionizing states with femto and atto second laser pulses*, J. L. Sanz-Vicario, J. F. Pérez Torres, F. Morales, E. Plessiat and F. Martín, Submitted to Journal of Physics: Conference Series: XXVI ICPEAC (2009).

Part III

Appendix

APPENDIX A

Iterative solvers for linear equations

When all the radial degrees of freedom of equations (3.29) and (3.54) and (3.55) for the one and two-photon double ionization of He, and equations (3.78) or any of the two photon equations for H_2 are expanded using the basis functions, these equations become a set of linear equations of the form $Ax = b$. For the box sizes that have been used along this work, the size of the matrix A, which is sparse, complex symmetric and indefinite, can be as large as a 16 millions by 16 millions sparse matrix. The solution of such a set of linear equations requires the use of parallel algorithms and supercomputing facilities. In order to achieve these results in a reasonable amount of time, there are several useful libraries that provide linear equation solvers. The one chosen to implement the linear equation solver is called *PETSc*, (Portable, Extensible Toolkit for Scientific Computation [123]). This library is build upon the MPI standard (Message Passing Interface), which makes it perfect to use in supercomputing centers. It offers efficient parallel implementations of modern techniques for linear equation solving, and also includes solvers for non-linear sets of equations and time step ordinary differential equations, altogether with parallel representation of sparse matrices.

The method chosen to find the solution of the set of linear equations is a Krylov subspace iterative method. In general, the location of the eigenvalues of A in the complex plane determines the convergence of iterative methods. In this scattering problem, the matrix represents the complex-scaled Hamiltonian, with most of its eigenvalues lying in a small region close to the origin, but also with a series of eigenvalues into the fourth quadrant of the complex plane. This eigenvalue arrangement results in very slow convergence for the direct application of an iterative method.

The method itself consists, in brief terms, in solving a preconditioned

matrix problem $M^{-1}Ax = M^{-1}b$ instead of the original matrix problem $Ax = b$. Here, the matrix M is chosen such that $M^{-1}A$ has an eigenvalue spectrum which leads to a faster convergence of the iterative Krylov subspace method. Two different methods of this kind have been used, both with similar speed and numerical accuracy. These methods are the generalized minimal residual method, and the stabilized version of bi-conjugate gradient squared.

The preconditioner matrix M is chosen from deriving a matrix M from A by reducing A to a block diagonal form through the neglect of the coupling elements between the angular parts of the basis functions. For more details on the construction and the properties of M refer to references [65, 124].

APPENDIX B

Eigenvalue solvers for big and sparse matrices

In order to obtain the bound state energies of the system being considered, which is necessary to solve equations (3.29), (3.54) and (3.55) for the one and two photon double ionization of He, and equation (3.78) or any of the two photon equations for H_2, the eigenvalues of a matrix as big in size as the ones considered for the problem of the linear set of equations solver must be found.

There is a software library, built on-top of *PETSc* (i.e. it uses *PETSc*'s matrix data representation, and it is fully integrated) called *SLEPc* (Scalable Library for Eigenvalue Problem Computations [125]) that offers several methods to compute the solution of large eigenvalue problems on parallel computers.

The method chosen to extract the bound state eigenvalues, which requires only to extract the lowest eigenvalue of the system, is a parallel implementation of the Lanczos algorithm. This iterative algorithm is related to the Arnoldi method. No details of the algorithm will be given here, but a very extensive documentation of the *SLEPc* package which includes a very descriptive section about this algorithm can be found in reference [126].

APPENDIX C

Atomic units

Atomics units (a.u.) are used as a system of units, which are especially convenient for atomic physics, through the focus on the properties and typical scales of the electrons. The fundaments of this system of units gets is based on fixing the numerical values of the following six physical constants to unity:

- Electron mass (m_e).
- Electron charge (e).
- Bohr radius (a_0) of the hydrogen atom.
- Absolute value of the electric potential energy of the hydrogen atom in the ground state.
- Planck's constant ($\hbar$)
- Coulomb's constant (k_e)

The values of these constants in the S.I. system are given in the following table, as well as other directly related constants:

Quantity	Atomic Units	S.I. Units.
Mass (electron rest mass)	$m_e = 1$	$9.1093897 \cdot 10^{-31}\ kg$
Length (bohr radius)	$a_0 = 1$	$5.29177249 \cdot 10^{-11}\ m$
Charge (elementary charge)	$e = 1$	$1.60217653 \cdot 10^{-19}\ C$
Reduced Planck's constant	$\hbar = 1$	$1.05457266 \cdot 10^{-34}\ J\ s$
Energy (Hartree energy)	$E_h = m_e c^2 \alpha^2 = 1$	$4.36 \cdot 10^{-18}\ J\ (27.2116\ eV)$
Speed of light (in a vacuum)	$c = 137$	$299,792,458\ m\ s^{-1}$
Hyperfine structure constant	$\alpha = \frac{1}{c} = \frac{1}{137}$	$3.33564 \cdot 10^{-9}\ s\ m^{-1}$
Time	$\frac{\hbar}{E_h} = 1$	$2.418884 \cdot 10^{-17}\ s$

BIBLIOGRAPHY

[1] R. K. Peterkop, Opt. Spectrosc. **13**, 87 (1962).

[2] M. R. H. Rudge and M. J. Seaton, Proc. R. Phys. Soc. **283**, 262 (1965).

[3] F. W. Byron and C. J. Joachain, Phys. Rev. **164**, 1 (1967).

[4] M. R. H. Rudge, Rev. Mod. Phys **40**, 564 (1968).

[5] M. Brauner, J. S. Briggs, and K. H., J. Phys. B **22**, 2265 (1989).

[6] F. Maulbetsch and J. S. Briggs, J. Phys. B **26**, 1679 (1993).

[7] J. Berakdar and J. S. Briggs, Phys. Rev. Lett. **72**, 3799 (1994).

[8] D. Proulx and R. Shakeshaft, J. of Phys. B **26**, L7 (1993).

[9] M. Pont and R. Shakeshaft, Phys. Rev. A. **51**, R2676 (1995).

[10] I. Bray and A. T. Stelbovics, Phys. Rev. A. **46**, 6995 (1992).

[11] I. Bray and D. V. Fursa, Phys. Rev. A. **54**, 2991 (1996).

[12] I. Bray, Phys. Rev. Lett. **78**, 4721 (1997).

[13] P. Selles, L. Malegat, and A. K. Kazansky, Phys. Rev. A **65**, 032711 (2002).

[14] F. Robicheaux, M. S. Pindzola, and D. R. Plante, Phys. Rev. A **55**, 3573 (1997).

[15] J. Colgan, M. S. Pindzola, and F. Robicheaux, J. Phys. B **34**, L457 (2001).

[16] R. Wehlitz *et al.*, Phys. Rev. Lett. **67**, 3764 (1991).

[17] Atomic Physics department at the Goethe-Universität of Frankfurt, COLTRIMS development history, http://hsb.uni-frankfurt.de/web/research/atomic/COLTRIMS/history/.

[18] J. Ullrich *et al.*, Journal of Physics B: Atomic, Molecular and Optical Physics **30**, 2917 (1997).

[19] H. Bräuning *et al.*, Journal of Physics B: Atomic, Molecular and Optical Physics **31**, 5149 (1998).

[20] V. Mergel *et al.*, Phys. Rev. Lett. **80**, 5301 (1998).

[21] J. A. R. Samson *et al.*, Phys. Rev. A **57**, 1906 (1998).

[22] J. P. Wightman, S. Cvejanovic, and T. J. Reddish, Journal of Physics B: Atomic, Molecular and Optical Physics **31**, 1753 (1998).

[23] K. Soejima, A. Danjo, K. Okuno, and A. Yagishita, Phys. Rev. Lett. **83**, 1546 (1999).

[24] A. Huetz and J. Mazeau, Phys. Rev. Lett. **85**, 530 (2000).

[25] T. Weber *et al.*, Nature **431**, 437 (2004).

[26] T. Weber *et al.*, Phys. Rev. Lett. **92**, 163001 (2004).

[27] M. Gisselbrecht *et al.*, Physical Review Letters **96**, 153002 (2006).

[28] W. Vanroose, F. Martín, T. N. Rescigno, and C. W. McCurdy, Science **310**, 1787 (2005).

[29] H. D. Cohen and U. Fano, Phys. Rev. **150**, 30 (1966).

[30] M. Walter and J. S. Briggs, J. Phys. B **32**, 2487 (1999).

[31] Rolles, D. and *et. al*, Nature (London) **437**, 711 (2005).

[32] Liu, X. J. and *et. al*, J. Phys. B **39**, 4801 (2006).

[33] J. Fernandez, O. Fojón, A. Palacios, and F. Martín, Phys. Rev. Lett. **98**, 043005 (2007).

[34] M. Foster *et al.*, Phys. Rev. A **75**, 062707 (2007).

[35] Akoury, D. *et al.*, Science **318**, 949 (2007).

[36] Kreidi, K. *et al.*, Phys. Rev. Lett. **100**, 133005 (2008).

[37] D. Proulx, M. Pont, and R. Shakeshaft, Phys. Rev. A **49**, 1208 (1994).

[38] L. A. A. Nikolopoulos and P. Lambropoulos, J. Phys. B **34**, 545 (2001).

[39] J. Colgan and M. S. Pindzola, Phys. Rev. Lett **88**, 173002 (2002).

[40] L. Feng and H. W. van der Hart, J. Phys. B **36**, L1 (2003).

[41] B. Piraux, J. Bauer, S. Laulan, and H. Bachau, Eur. Phys. J. D **26**, 7 (2003).

[42] S. X. Hu, J. Colgan, and L. A. Collins, J. Phys. B **38**, L35 (2005).

[43] P. Lambropoulos, L. A. A. Nikolopoulos, and M. G. Makris, Phys. Rev. A **72**, 013410 (2005).

[44] E. Foumouo, G. L. Kamta, G. Edah, and B. Piraux, Phys. Rev. A **74**, 063409 (2006).

[45] A. S. Kheifets and I. A. Ivanov, J. Phys. B **39**, 1731 (2006).

[46] R. Shakeshaft, Phys. Rev. A **76**, 063405 (2007).

[47] D. A. Horner *et al.*, Phys. Rev. Lett. **98**, 073001 (2007).

[48] L. A. A. Nikolopoulos and P. Lambropoulos, J. Phys. B **40**, 1347 (2007).

[49] I. A. Ivanov and A. S. Kheifets, Phys. Rev. A **75**, 033411 (2007).

[50] D. A. Horner, C. W. McCurdy, and T. N. Rescigno, Phys. Rev. A **78**, 043416 (2008).

[51] E. Foumouo *et al.*, J. Phys. B **41**, 1 (2008).

[52] E. Foumouo, P. Antoine, H. Bachau, and B. Piraux, New J. Phys. **10**, 025017 (2008).

[53] P. Lambropoulos, L. A. A. Nikolopoulos, M. G. Makris, and A. Mihelič, Phys. Rev. A **78**, 055402 (2008).

[54] J. Feist *et al.*, Phys. Rev. A **77**, 043420 (2008).

[55] H. Hasegawa *et al.*, Phys. Rev. A **71**, 023407 (2005).

[56] A. A. Sorokin *et al.*, Phys. Rev. A **75**, 051402 (2007).

[57] A. Rudenko *et al.*, Phys. Rev. Lett. **101**, 073003 (2008).

[58] Y. H. Jiang *et al.*, Abstracts of the 11th International Conference on Multiphoton Processes Mo03 (2008).

[59] J. Colgan, M. S. Pindzola, and F. Robicheaux, J. Phys. B. **41**, 121002 (2008).

[60] F. Morales *et al.*, J. Phys. B. **42**, 134013 (2009).

[61] B. Simon, Phys. Lett. **71**, 211 (1979).

[62] C. W. McCurdy, M. Baertschy, and T. N. Rescigno, J. Phys. B **37**, R137 (2004).

[63] W. Vanroose, F. Martín, T. N. Rescigno, and C. W. McCurdy, Phys. Rev. A **70**, 050703 (2004).

[64] F. Morales, C. W. McCurdy, and F. Martín, Phys. Rev. A **73**, 014702 (2005).

[65] W. Vanroose *et al.*, Phys. Rev. A **74**, 052702 (2006).

[66] T. Regge, Nuevo Cimento **14**, 951 (1959).

[67] T. Regge, Nuevo Cimento **18**, 947 (1960).

[68] A. Bottino, A. Longoni, and T. Regge, Nuevo Cimento **23**, 954 (1962).

[69] J. Nuttal and H. L. Cohen, Phys. Rev. **188**, 1542 (1969).

[70] E. Baslev and J. M. Combes, Commun. Math. Phys **22**, 280 (1971).

[71] J. Aguilar and J. M. Combes, Commun. Math. Phys **22**, 269 (1971).

[72] B. Simon, Commun. Math. Phys **27**, 1 (1972).

[73] G. D. Doolen, J. Nuttal, and R. W. Stagat, Phys. Rev. A **10**, 1612 (1974).

[74] W. P. Reinhardt, Ann. Rev. Phys. Chem. **33**, 223 (1982).

[75] M. S. Pindzola and D. R. Schultz, Phys. Rev. A **53**, 1525 (1996).

[76] M. S. Pindzola and F. Robicheaux, Phys. Rev. A **54**, 2142 (1996).

[77] C. Bottcher, J. Phys. B **14**, L349 (1981).

[78] L. Malegat, P. Selles, and A. K. Kazansky, J. Phys. B **14**, L349 (1981).

[79] S. Watanabe, Y. Hosoda, and D. Kato, J. Phys. B **26**, L495 (1993).

[80] D. Kato and S. Watanabe, J. Phys. B **29**, L779 (1996).

[81] J. J. Sakurai, *Advanced Quantum Mechanics* (Addison Wesley, 1967).

[82] L. I. Schiff, *Quantum Mechanics* (McGraw-Hill Inc., 1969).

[83] C. A. Nicolaides and D. R. Beck, Phys. Lett. A **65**, 11 (1978).

[84] P. B. Kurasov, A. Scrinzi, and N. Elander, Phys. Rev. A. **49**, 5095 (1994).

[85] R. G. Newton, *Scattering Theory of Waves and Particles* (New York : Springer, 1982).

[86] C. W. McCurdy, D. A. Horner, and T. N. Rescigno, Phys. Rev. A **63**, 022711 (2001).

[87] R. K. Peterkop, *Theory of Ionization of Atoms by Electron Impact* (Associated University Press, Boulder, CO, 1977).

[88] A. R. Edmonds, *Angular Momentum in Quantum Mechanics* (Princeton, NJ: Princeton University Press, 1957), Vol. 118, p. 37.

[89] C. W. McCurdy and T. N. Rescigno, Phys. Rev. A **62**, 032712 (2000).

[90] M. Baertschy, T. N. Rescigno, and C. W. McCurdy, Phys. Rev. A **60**, 022709 (2001).

[91] M. Baertschy, T. N. Rescigno, W. A. Isaacs, and C. W. McCurdy, Phys. Rev. A **60**, R13 (1999).

[92] C. W. McCurdy, T. N. Rescigno, and D. Byrum, Phys. Rev. A **56**, 1958 (1997).

[93] C. W. McCurdy and T. N. Rescigno, Phys. Rev. A **56**, R4369 (1997).

[94] D. A. Telnov and S.-I. Chu, Phys. Rev. A **59**, 2864 (1999).

[95] D. A. Telnov and S.-I. Chu, Phys. Rev. A **66**, 043417 (2002).

[96] C. W. McCurdy and F. Martín, J. Phys. B **37**, 917 (2004).

[97] T. N. Rescigno and C. W. McCurdy, Phys. Rev. A **62**, 032706 (2000).

[98] I. J. Schoenberg, Quart. Appl. Math. **4**, 45 (1946).

[99] B. W. Shore, J. Phys. B **6**, 1923 (1973).

[100] C. de Boor, *A Practical Guide to Splines* (Springer, 1978).

[101] F. Martín, J. Phys. B **32**, R197 (1999).

[102] H. Bachau, E. Cormier, J. E. Hansen, and F. Martín, Rep. Prog. Phys. **64**, 1601 (2001).

[103] D. H. Norrie and G. de Vries, *An Introduction to Finite Element Analysis* (Academic New York, 1978).

[104] J. V. Lill, G. A. Parker, and J. C. Light, Chem. Phys. Lett. **89**, 483 (1982).

[105] A. Scrinzi and N. Elander, J. Chem. Phys. **98**, 3866 (1993).

[106] A. Scrinzi, Comput. Phys. Commun. **86**, 67 (1995).

[107] D. E. Manolopoulos and R. E. Wyatt, Chem. Phys. Lett. **152**, 23 (1988).

[108] J. Colgan, M. S. Pindzola, and F. Robicheaux, Phys. Rev. Lett. **98**, 153001 (2007).

[109] T. J. Reddish *et al.*, Phys. Rev. Lett. **100**, 193001 (2008).

[110] M. Walter and J. S. Briggs, Phys. Rev. Lett. **85**, 1630 (2000).

[111] E. Karule, J. Phys. B. **18**, 2207 (1985).

[112] A. Saenz and P. Lambropoulos, J. Phys. B **32**, 5629 (1999).

[113] H. Bachau, P. Lambropoulos, and X. Tang, Phys. Rev. A **42**, 5801 (1990).

[114] H. Bachau, P. Lambropoulos, and X. Tang, Phys. Rev. A **44**, 4516 (1991).

[115] D. A. Horner, T. N. Rescigno, and C. W. McCurdy, Phys. Rev. A **77**, 030703 (2008).

[116] P. Antoine, E. Foumouo, and B. Piraux, Phys. Rev. A **78**, 023415 (2008).

[117] I. Sánchez and F. Martín, J. Chem. Phys. **106**, 7720 (1997).

[118] D. A. Horner *et al.*, Phys. Rev. Lett. **101**, 183002 (2008).

[119] A. Apalategui and A. Saenz, J. Phys. B. **35**, 1909 (2002).

[120] A. Palacios, Ph.D. thesis, Universidad Autónoma de Madrid, 2006.

[121] A. Palacios, H. Bachau, and F. Martín, Phys. Rev. Lett. **96**, 143001 (2006).

[122] A. Palacios, T. N. Rescigno, and C. W. McCurdy, Phys. Rev, A **79**, 033402 (2009).

[123] PETSc web page, http://www.mcs.anl.gov/petsc/.

[124] Y. Saad, *Iterative Methods for Sparse Linear Systems* (SIAM, Philadelphia, 2003).

[125] SLEPc web page, http://www.grycap.upv.es/slepc.

[126] SLEPc web page, http://www.grycap.upv.es/slepc/documentation/reports/str5.pdf.